

1 **Evolution of cellular diversity in primary motor cortex of human, marmoset monkey, and mouse**

2

3 Trygve E. Bakken, Nikolas L. Jorstad, Qiwen Hu, Blue B. Lake, Wei Tian, Brian E. Kalmbach, Megan  
4 Crow, Rebecca D. Hodge, Fenna M. Krienen, Staci A. Sorensen, Jeroen Eggermont, Zizhen Yao, Brian  
5 D. Aeversmann, Andrew I. Aldridge, Anna Bartlett, Darren Bertagnolli, Tamara Casper, Rosa G.  
6 Castanon, Kirsten Crichton, Tanya L. Daigle, Rachel Dalley, Nick Dee, Nikolai Dembrow, Dinh Diep,  
7 Song-Lin Ding, Weixiu Dong, Rongxin Fang, Stephan Fischer, Melissa Goldman, Jeff Goldy, Lucas T.  
8 Graybuck, Brian R. Herb, Xiaomeng Hou, Jayaram Kancherla, Matthew Kroll, Kanan Lathia, Baldur van  
9 Lew, Yang Eric Li, Christine S. Liu, Hanqing Liu, Anup Mahurkar, Delissa McMillen, Jeremy A. Miller,  
10 Marmar Moussa, Joseph R. Nery, Joshua Orvis, Scott Owen, Carter R. Palmer, Thanh Pham, Nongluk  
11 Plongthongkum, Olivier Poirion, Nora M. Reed, Christine Rimorin, Angeline Rivkin, William J.  
12 Romanow, Adriana E. Sedeño-Cortés, Kimberly Siletti, Saroja Somasundaram, Josef Sulc, Michael  
13 Tieu, Amy Torkelson, Herman Tung, Xinxin Wang, Fangming Xie, Anna Marie Yanny, Renee Zhang,  
14 Seth A. Ament, Hector Corrada Bravo, Jerold Chun, Alexander Dobin, Jesse Gillis, Ronna Hertzano,  
15 Patrick R. Hof, Thomas Höllt, Gregory D. Horwitz, C. Dirk Keene, Peter V. Kharchenko, Andrew L. Ko,  
16 Boudewijn P. Lelieveldt, Chongyuan Luo, Eran A. Mukamel, Sebastian Preissl, Aviv Regev, Bing Ren,  
17 Richard H. Scheuermann, Kimberly Smith, William J. Spain, Owen R. White, Christof Koch, Michael  
18 Hawrylycz, Bosiljka Tasic, Evan Z. Macosko, Steven A. McCarroll, Jonathan T. Ting, Hongkui Zeng,  
19 Kun Zhang, Guoping Feng, Joseph R. Ecker, Sten Linnarsson, Ed S. Lein

20

21 Correspondence: Ed S. Lein ([edl@alleninstitute.org](mailto:edl@alleninstitute.org)), Trygve E. Bakken ([trygveb@alleninstitute.org](mailto:trygveb@alleninstitute.org))

22

23 **Abstract**

24 The primary motor cortex (M1) is essential for voluntary fine motor control and is functionally conserved  
25 across mammals. Using high-throughput transcriptomic and epigenomic profiling of over 450,000 single  
26 nuclei in human, marmoset monkey, and mouse, we demonstrate a broadly conserved cellular makeup  
27 of this region, whose similarity mirrors evolutionary distance and is consistent between the

28 transcriptome and epigenome. The core conserved molecular identity of neuronal and non-neuronal  
29 types allowed the generation of a cross-species consensus cell type classification and inference of  
30 conserved cell type properties across species. Despite overall conservation, many species  
31 specializations were apparent, including differences in cell type proportions, gene expression, DNA  
32 methylation, and chromatin state. Few cell type marker genes were conserved across species,  
33 providing a short list of candidate genes and regulatory mechanisms responsible for conserved features  
34 of homologous cell types, such as the GABAergic chandelier cells. This consensus transcriptomic  
35 classification allowed the Patch-seq identification of layer 5 (L5) corticospinal Betz cells in non-human  
36 primate and human and characterization of their highly specialized physiology and anatomy. These  
37 findings highlight the robust molecular underpinnings of cell type diversity in M1 across mammals and  
38 point to the genes and regulatory pathways responsible for the functional identity of cell types and their  
39 species-specific adaptations.

40

## 41 Introduction

42 Single-cell transcriptomic and epigenomic methods provide a powerful lens on understanding the  
43 cellular makeup of highly complex brain tissues based on distinct patterns of gene expression and  
44 underlying regulatory mechanisms<sup>1-7</sup>. Applied to mouse and human neocortex, single-cell or single-  
45 nucleus transcriptomic analysis has yielded a complex but finite classification of cell types with  
46 approximately 100 discriminable neuronal and non-neuronal types in any given neocortical region<sup>1,2,6,8</sup>.  
47 Similar analyses using epigenomic methods have shown that many cortical cell types can be  
48 distinguished on the basis of regions of open chromatin or DNA methylation<sup>5,9,10</sup>. Furthermore, several  
49 recent studies have shown that transcriptomically-defined cell types can be aligned across species<sup>2,11-</sup>  
50<sup>13</sup>, indicating that these methods provide a path to quantitatively study evolutionary conservation and  
51 divergence at the level of cell types. However, application of these methods has been highly  
52 fragmented to date. Human and mouse comparisons have been performed in different cortical regions,  
53 using single-cell (with biases in cell proportions) versus single-nucleus (with biases in transcript

54 makeup) analysis, and most single-cell transcriptomic and epigenomic studies have been performed  
55 independently.

56

57 The primary motor cortex (MOp in mouse, M1 in human and non-human primates, all referred to as M1  
58 herein) provides an ideal cortical region to address questions about cellular evolution in rodents and  
59 primates by integrating these approaches. Unlike the primary visual cortex (V1), which is highly  
60 specialized in primates, or frontal and temporal association areas, whose homologues in rodents  
61 remain poorly defined, M1 is essential for fine motor control and is functionally conserved across  
62 placental mammals. M1 is an agranular cortex, lacking a defined L4, although neurons with L4-like  
63 properties have been described<sup>14</sup>. L5 of carnivore and primate M1 contains exceptionally large  
64 “giganto-cellular” corticospinal neurons (Betz cells in primates<sup>15,16</sup> that contribute to the pyramidal tract  
65 and are highly specialized for their unusually large size with distinctive “taproot”-style dendrites<sup>17,18</sup>.  
66 Extracellular recordings from macaque corticospinal neurons reveal distinctive action potential  
67 properties supportive of a high conduction velocity and similar, unique properties have been reported  
68 during intracellular recordings from giganto-cellular neurons in cats<sup>19–21</sup>. Additionally, some primate Betz  
69 cells directly synapse onto alpha motor neurons, whereas in cats and rodents these neurons synapse  
70 instead onto spinal interneurons<sup>22,23</sup>. These observations suggest that Betz cells possess specialized  
71 intrinsic mechanisms to support rapid communication, some of which are primate specific.

72

73 Conservation of cellular features across species is strong evidence for evolutionary constraints on  
74 important cellular function. To explore evolutionary conservation and divergence of the M1 cellular  
75 makeup and its underlying molecular and gene regulatory mechanisms, we combined saturation  
76 coverage single-nucleus transcriptome analysis, DNA methylation, and combined open chromatin and  
77 transcriptome analysis of mouse, marmoset, and human M1 and transcriptomic profiling of macaque  
78 M1 L5. We describe a robust classification of neuronal and non-neuronal cell types in each species that  
79 is highly consistent between the transcriptome and epigenome. Cell type alignment accuracy and  
80 similarity varied as a function of evolutionary distance, with human more similar to non-human primate

81 than to mouse. We derived a consensus mammalian classification with globally similar cellular diversity,  
82 varying proportions, and species specializations in gene expression between conserved cell classes.  
83 Few genes had conserved cell type-specific expression across species and likely contribute to other  
84 conserved cellular properties, such as the unique morphology of chandelier GABAergic neurons.  
85 Conversely, these data also allow a targeted search for genes responsible for species specializations  
86 such as the distinctive anatomy, physiology and axonal projections of Betz cells, large corticospinal  
87 neurons in primates that are responsible for voluntary fine motor control. Together these findings  
88 highlight the strength of a comparative approach to understand cortical cellular diversity and identify  
89 conserved and specialized gene and gene regulatory mechanisms underlying cellular identity and  
90 function.

91  
92 We made all primary and analyzed data publicly available. Raw sequence data are available for  
93 download from the Neuroscience Multi-omics Archive ([nemoarchive.org](http://nemoarchive.org)) and the Brain Cell Data  
94 Center ([biccn.org/data](http://biccn.org/data)). Visualization and analysis tools are available at NeMO Analytics  
95 ([nemoanalytics.org](http://nemoanalytics.org)) and Cytosplore Viewer ([viewer.cytosplore.org](http://viewer.cytosplore.org)). These tools allow users to compare  
96 cross-species datasets and consensus clusters via genome and cell browsers and calculate differential  
97 expression within and among species. A semantic representation of the cell types defined through  
98 these studies is available in the provisional Cell Ontology  
99 (<https://bioportal.bioontology.org/ontologies/PCL>; Supplementary Table 1).

100

## 101 Results

### 102 Multi-omic cell type taxonomies

103 To characterize the molecular diversity of M1 neurons and non-neuronal cells, we applied multiple  
104 single-nucleus transcriptomic (plate-based SMART-seq v4, SSv4, and droplet-based Chromium v3,  
105 Cv3, RNA-sequencing) and epigenomic (single-nucleus methylcytosine sequencing 2, snmC-seq2;  
106 single-nucleus chromatin accessibility and mRNA expression sequencing, SNARE-seq2) assays on

107 isolated M1 samples from human (Extended Data Fig. 1a), marmoset, and mouse brain. Cellular  
108 diversity was also profiled selectively in M1 L5 from macaque monkeys using Cv3 (Fig. 1b) to allow  
109 Patch-seq mapping in physiology experiments. M1 was identified in each species based on its  
110 stereotyped location in the caudal portion of frontal cortex and histological features such as the  
111 presence of exceptionally large pyramidal neurons in L5 of M1, classically known as Betz cells in  
112 human, other primates, and carnivores (Fig. 1a; <sup>17</sup>). Single nuclei were dissociated, sorted, and  
113 transcripts were quantified with Cv3 for deep sampling in all four species, and additionally using SSV4  
114 in human and mouse for full-length transcript information. For human and a subset of mouse nuclei,  
115 individual layers of M1 were profiled independently using SSV4. Whole-genome DNA methylation, and  
116 open chromatin combined with transcriptome measurements, were quantified in single nuclei from a  
117 subset of species (Fig. 1b). Mouse datasets are also reported in a companion paper <sup>6</sup>. Median neuronal  
118 gene detection was higher in human using SSV4 (7296 genes) than Cv3 (5657), partially due to 20-fold  
119 greater read depth, and detection was lower in marmoset (4211) and mouse (5046) using Cv3  
120 (Extended Data Fig. 1b-i).

121  
122 For each species, a diverse set of neuronal and non-neuronal cell type clusters were defined based on  
123 unsupervised clustering of snRNA-seq datasets (cluster metadata in Supplementary Table 2). Human  
124 SSV4 and Cv3 data were integrated based on shared co-expression using Seurat <sup>24</sup>, and 127 clusters  
125 were identified that included nuclei from both RNA-seq platforms (Extended Data Fig. j-l). Marmoset  
126 clusters (94) were determined based on independent clustering of Cv3 data using a similar analysis  
127 pipeline. Mouse clusters (116) were defined in a companion paper <sup>6</sup> using seven integrated  
128 transcriptomics datasets. These differences in the number of clusters are likely due to a combination of  
129 statistical methodological differences as well as sampling and data quality differences rather than true  
130 biological differences in cell diversity. For example, more non-neuronal nuclei were sampled in mouse  
131 (58,098) and marmoset (21,189) compared to human (4,005), resulting in greater non-neuronal  
132 resolution in those species. t-SNE visualizations of transcriptomic similarities across nuclei revealed

133 well-separated clusters in all species and mixing among donors, with some donor-specific technical  
134 effects in marmoset (Extended Data Fig. 1m,n).

135

136 Post-clustering, cell types were organized into taxonomies based on transcriptomic similarities and  
137 given a standardized nomenclature (Supplementary Table 3). As described previously for a different  
138 cortical region <sup>2</sup>, taxonomies were broadly conserved across species and reflected different  
139 developmental origins of major non-neuronal and neuronal classes (e.g. GABAergic neurons from  
140 ganglionic eminences (GEs) versus glutamatergic neurons from the cortical plate) and subclasses (e.g.  
141 GABAergic CGE-derived *Lamp5/Sncg* and *Vip* versus MGE-derived *Pvalb* and *Sst*), allowing  
142 identification and naming of these subclasses across species. Consequently, cardinal cell subclass  
143 properties can be inferred, such as intratelencephalic (IT) projection patterns. Greater species variation  
144 was seen at the highest level of resolution (cell types) that are named based on transcription data in  
145 each species including the layer (if available), major class, subclass marker gene, and most specific  
146 marker gene (e.g. L3 Exc *RORB OTOGL* in human; additional markers in Supplementary Tables 4-6).  
147 GABAergic types were uniformly rare (< 4.5% of neurons), whereas more variable frequencies were  
148 found for glutamatergic types (0.01 to 18.4% of neurons) and non-neuronal types (0.15% to 56.2% of  
149 non-neuronal cells).

150

151 Laminar dissections in human M1 further allowed the estimation of laminar distributions of cell types  
152 based on the proportions of nuclei dissected from each layer (Fig. 1c). As expected and previously  
153 reported in middle temporal gyrus (MTG) of human neocortex <sup>2</sup>, glutamatergic neuron types were  
154 specific to layers. A subset of CGE-derived *Lamp5/Sncg* GABAergic neurons were restricted to L1, and  
155 MGE-derived GABAergic types (*Sst* and *Pvalb*) displayed laminar patterning, with transcriptomically  
156 similar types showing proximal laminar distributions, whereas *Vip* GABAergic neuron types displayed  
157 the least laminar specificity. Three astrocyte subtypes had frequencies and layer distributions that  
158 correlated with known morphologically-defined astrocyte types <sup>25</sup>, including a common type in all layers  
159 (protoplasmic), a rare type in L1 (interlaminar) <sup>26</sup>, and a rare type in L6 (fibrous).

160

161 Single-nucleus sampling provides a relatively unbiased survey of cellular diversity<sup>2,27</sup> and enables  
162 comparison of cell subclass proportions across species. For each donor, we estimated the proportion of  
163 GABAergic and glutamatergic cells among all neurons and compared the proportions across species.  
164 Consistent with previously reported differences in GABAergic neuron frequencies in primate versus  
165 rodent somato-motor cortex based on histological measurements (reviewed in<sup>28</sup>), we found twice as  
166 many GABAergic neurons in human (33%) compared to mouse M1 (16%) an intermediate proportion  
167 (23%) in marmoset (Fig. 1f). Despite these differences, the relative proportions of GABAergic neuron  
168 subclasses were similar. Exceptions to this included an increased proportion of *Vip* and *Sncg* cells and  
169 decreased proportion of *Pvalb* cells in marmoset. Among glutamatergic neurons, there were  
170 significantly more L2 and L3 IT neurons in human than marmoset and mouse (Fig. 1f), consistent with  
171 the dramatic expansion of supragranular cortical layers in human (Fig. 1a)<sup>29</sup>. The L5  
172 extratelencephalic-projecting (ET) types (also known as pyramidal tract, PT, or subcerebral types),  
173 including corticospinal neurons and Betz cells in primate M1, comprised a significantly smaller  
174 proportion of glutamatergic neurons in primates than mouse. This species difference was also reported  
175 in MTG<sup>2</sup>, possibly reflecting the spatial dilution of these cells with the expansion of neocortex in  
176 primates. Similarly, the L6 cortico-thalamic (CT) neuron populations were less than half as frequent in  
177 primates compared to mouse, whereas the L6 *Car3* type was rare in all species and relatively more  
178 abundant in marmoset.

179

180 Individual nuclei were isolated from M1 of the same donors for each species and molecular profiles  
181 were derived for DNA methylation (snmC-seq2) and open chromatin combined with mRNA (SNARE-  
182 seq2). Independent unsupervised clustering of epigenomic data also resulted in diverse clusters (see  
183 below, Figs. 4 and 5) that were mapped back to RNA clusters based on shared (directly measured or  
184 inferred) marker gene expression. Cell epigenomes were highly correlated with transcriptomes, and all  
185 epigenomic clusters mapped to one or more transcriptomic clusters. The epigenome data generally had  
186 lower cell type resolution (Fig. 1c-e), although this may be due to sampling fewer cells or sparse

187 genomic coverage. Interestingly, snmC-seq2 and SNARE-seq2 resolved different granularities of cell  
188 types. For example, more GABAergic *Vip* neuron types were identified in human M1 based on DNA-  
189 methylation than open chromatin, despite profiling only 5% as many nuclei with snmC-seq2 (Fig. 1c).

190

### 191 **Consensus cellular M1 taxonomy across species**

192 A consensus cell type classification identifies conserved molecular makeup and allows direct cross-  
193 species comparisons. The snRNA-seq Cv3 datasets were integrated using Seurat<sup>24</sup> that aligns nuclei  
194 across species based on shared co-expression of a subset of orthologous genes with variable  
195 expression. We repeated this analysis for three cell classes: GABAergic neurons (Fig. 2), glutamatergic  
196 neurons (Extended Data Fig. 3) and non-neuronal cells (Extended Data Fig. 4). As represented in a  
197 reduced dimension UMAP space (Fig.2a), GABAergic neuronal nuclei were well-mixed across species.  
198 Eight well-defined populations formed distinct islands populated by cells from all three species,  
199 including CGE-derived (*Lamp5*, *Sncg*, *Vip*) and MGE-derived (*Pvalb*, *Sst*, *Sst Chodl*) subclasses, and  
200 *Lamp5 Lhx6* and chandelier cell (ChC) types. To identify conserved molecular expression for each  
201 subclass across species, we first identified genes that were enriched in each subclass (“markers”)  
202 compared to all GABAergic neurons in each species (ROC test; AUC > 0.7). Then, we looked for  
203 overlap among these genes across species. Each subclass had a core set of conserved markers (Fig.  
204 2b, markers listed in Supplementary Table 7), and many subclass markers were species-specific. The  
205 contrast between a minority of conserved and majority of species-specific marker genes enriched in  
206 subclasses is particularly clear in the heatmap in Figure 2c (Supplementary Table 8). As expected  
207 based on their closer evolutionary distance, human and marmoset shared more subclass markers with  
208 each other than with mouse (Fig. 2b).

209

210 Cell types remained distinct within species and aligned across species in the integrated transcriptomic  
211 space (Fig. 2d). To establish a consensus taxonomy of cross-species clusters, we used unsupervised  
212 clustering to split the integrated space into more than 500 small clusters (‘metacells’) and built a  
213 dendrogram and quantified branch stability by subsampling metacells and reclustered (Extended Data



214 Fig. 2a). Metacells were merged with nearest neighbors until all branches were stable and included  
215 nuclei from the three species (see Methods). We used cluster overlap heatmaps to visualize the  
216 alignment of cell types across species based on membership in merged metacells (Fig. 2e). 24  
217 GABAergic consensus clusters displayed consistent overlap of clusters among the three species and  
218 are highlighted as blue boxes in the heatmaps (Fig. 2e).

219

220 We next constructed a consensus taxonomy by pruning the metacell dendrogram (Extended Data Fig.  
221 2a), and demonstrated that all types were well mixed across species (Fig. 2f, grey branches). The  
222 robustness of consensus types was bolstered by a conserved set of marker genes (Extended Data Fig.  
223 2d) and high classification accuracy of subclasses (Extended Data Fig. 2e, data in Supplementary  
224 Table 9) and types (Extended Data Fig. 2f, data in Supplementary Table 9) compared to nearest  
225 neighbors within and among species using a MetaNeighbor analysis<sup>30</sup>. Distinct consensus types (ChC,  
226 *Sst Chodl*) were the most robust (mean AUROC = 0.99 within-species and 0.88 cross-species), while  
227 *Sncg* and *Sst* types could not be as reliably differentiated from closely related types (mean AUROC =  
228 0.84 within-species and 0.50 cross-species). Most consensus GABAergic types were enriched in the  
229 same layers in human and mouse (Fig. 2f), although there were also notable species differences. For  
230 example, ChCs were enriched in L2/3 in mouse and distributed across all layers in human as was seen  
231 in temporal cortex (MTG) based on RNA ISH<sup>2</sup>. *Sst Chodl* was restricted to L6 in mouse and also found  
232 in L1 and L2 in human, consistent with previous observations of sparse expression of SST in L1 in  
233 human not mouse cortex<sup>31</sup>.

234

235 More consensus clusters could be resolved by pairwise alignment of human and marmoset than  
236 primates and mouse, particularly *Vip* subtypes (Fig. 2g, Extended Data Fig. 2b). Higher resolution  
237 integration of cell types was also apparent in cluster overlap plots between human and marmoset  
238 clusters (Fig. 2e, Extended Data Fig. 2c). We quantified the expression conservation of functionally  
239 annotated sets of genes by testing the ability of gene sets to discriminate GABAergic consensus types.  
240 This analysis was framed as a supervised learning task, both within- and between-species<sup>30</sup>. Within-

241 species, gene sets related to neuronal connectivity and signaling were most informative for cell type  
242 identity (Extended Data Fig. 2g), as reported in human and mouse cortex<sup>2,32</sup>. All gene sets had  
243 remarkably similar consensus type classification performance across species ( $r > 0.95$ ; Fig. 2h),  
244 pointing to strong evolutionary constraints on the cell type specificity of gene expression central to  
245 neuronal function. Gene set classification performance was systematically reduced when training and  
246 testing between primates (44% reduction) and between primates and mouse (65% reduction; Fig. 2h).  
247 Therefore, many cell type marker genes were expressed in different consensus types between species.  
248 Future comparative work can compare reductions in classification performance to evolutionary  
249 distances between species to estimate rates of expression change across phylogenies.  
250  
251 Cross-species consensus types were defined for glutamatergic neurons using an identical approach as  
252 for GABAergic neurons (Extended Data Fig. 3). In general, glutamatergic subclasses aligned well  
253 across species and had a core set of conserved markers as well as many species-specific markers  
254 (Extended Data Fig. 3a-c, genes listed in Supplementary Tables 10-11). 13 consensus types were  
255 defined across species. Glutamatergic types had fewer conserved markers than GABAergic types  
256 (Extended Data Fig. 3d-f,j), although subclasses and types were similarly robust (mean within-species  
257 AUROC = 0.86 for GABAergic types and 0.85 for glutamatergic types) based on classification  
258 performance (Extended Data Fig. 3k,l and Supplementary Table 9). Human and marmoset had  
259 consistently more conserved marker genes than primates and mouse (Extended Data Fig. 3i) and could  
260 be aligned at somewhat higher resolution (Extended Data Fig. 3g,h) for L5/6 NP and L5 IT subclasses.  
261  
262 Integration of non-neuronal cells was performed similarly to neurons (Extended Data Fig. 4a).  
263 Consensus clusters (blue boxes in Extended Data Fig. 4c) that shared many marker genes were  
264 identified across species (Extended Data Fig. 4d), and there was also evidence for the evolutionary  
265 divergence of gene expression in consensus types. For example, the Astro\_1 type had 560 DEGs  
266 (Wilcox test; FDR < 0.01, log-fold change > 2) between human and mouse and only 221 DEGs  
267 between human and marmoset (Extended Data Fig. 4e). The human cortex contains several

268 morphologically distinct astrocyte types<sup>33</sup>: interlaminar (ILA) in L1, protoplasmic in all layers, varicose  
269 projection in deep layers, and fibrous in white matter (WM). We previously reported two transcriptomic  
270 clusters in human MTG that corresponded to protoplasmic astrocytes and ILAs<sup>2</sup>, and we validated  
271 these types in M1 (Extended Data Fig. 4g,h). We identified a third type, Astro L1-6 *FGFR3 AQP1*, that  
272 expresses *APQ4* and *TNC* and corresponds to fibrous astrocytes in WM (Extended Data Fig. 4g, left  
273 ISH). A putative varicose projection astrocyte did not express human astrocyte markers (Extended Data  
274 Fig. 4g, middle and right ISH), and this rare type may not have been sampled or is not  
275 transcriptomically distinct.

276

277 Species comparison of non-neuronal cell types was more challenging than for neurons due to variable  
278 sampling across species and more immature non-neuronal cells in mouse. 5- to 15-fold lower sampling  
279 of non-neuronal cells in human impacted detection of rare types. For example, pericytes, smooth  
280 muscle cells (SMCs), and some subtypes of vascular and leptomeningeal cells (VLMCs) were present  
281 in marmoset and mouse and not human datasets (Extended Data Fig. 4c, right plot, blue arrows),  
282 although these cells are clearly present in human cortex (for example, see<sup>34</sup>). A maturation lineage  
283 between oligodendrocyte precursor cells (OPCs) and oligodendrocytes based on reported marker  
284 genes<sup>35</sup> that was present in mouse and not primates (Extended Data Fig. 4b) likely represents the  
285 younger age of mouse tissues used. Mitotic astrocytes (*Astro\_Top2a*) were also only present in mouse  
286 (Extended Data Fig. 4a,c) and represented 0.1% of non-neuronal cells. Primates had a unique  
287 oligodendrocyte population (*Oligo SLC1A3 LOC103793418* in marmoset and *Oligo L2-6 OPALIN*  
288 *MAP6D1* in human) that was not a distinct cluster in mouse (Extended Data Fig. 4c, left plot, blue  
289 arrow). Surprisingly this oligodendrocyte clustered with glutamatergic types (Fig. 1c,d) and was  
290 associated with neuronal transcripts such as *NPTX1*, *OLFM3*, and *GRIA1* (Extended Data Fig. 4i). This  
291 was not an artifact, as FISH for markers of this type (*SOX10*, *ST18*) co-localized with neuronal markers  
292 in the nuclei of cells that were sparsely distributed across all layers of human and marmoset M1  
293 (Extended Data Fig. 4j). This may represent an oligodendrocyte type that expresses neuronal genes or

294 could represent phagocytosis of parts of neurons and accompanying transcripts that are sequestered in  
295 phagolysosomes adjacent to nuclei.

296

297 To assess differential isoform usage between human and mouse, we used SSv4 data with full transcript  
298 coverage and estimated isoform abundance in cell subclasses. Remarkably, 25% of moderately  
299 expressed (> 10 transcripts per million) isoforms showed a large change (>9-fold) in usage between  
300 species, and isoform switching was 30-60% more common in non-neuronal than neuronal cells  
301 (Extended Data Fig. 2h,i, Supplementary Table 12). For example,  $\beta$ 2-Chimaerin (*CHN2*), a gene shown  
302 to mediate axonal pruning in the hippocampus<sup>36</sup>, was highly expressed in human and mouse L5/6 NP  
303 neurons. In mouse, the short isoform was almost exclusively expressed, while in human, longer  
304 isoforms were also expressed (Extended Data Fig. 2j).

305

### 306 **Open chromatin profiling reveals distinct cell type gene regulation**

307 To directly match accessible chromatin profiles to RNA-defined cell populations, we used SNARE-Seq  
308<sup>37</sup>, now modified for highly multiplexed combinatorial barcoding (SNARE-Seq2)<sup>38</sup>. We generated  
309 84,178 and 9,946 dual-omic single-nucleus RNA and accessible chromatin (AC) datasets from human  
310 (n = 2) and marmoset (n = 2) M1, respectively (Extended Data Fig. 5a-b, Supplementary Table 13). On  
311 average, 2,242 genes (5,764 unique transcripts) were detected per nucleus for human and 3,858 genes  
312 (12,400 unique transcripts) per nucleus for marmoset, due to more than 4-fold greater sequencing  
313 depth for marmoset (average 17,576 reads per nucleus for human and 77,816 reads per nucleus for  
314 marmoset).

315

316 To define consensus clusters, SNARE-seq2 single-nucleus RNA expression data were mapped to  
317 human and marmoset transcriptomic clusters (Fig. 1c,d) based on correlated expression of cell type  
318 marker genes. SNARE-seq2 transcriptomes were also independently clustered, with both approaches  
319 giving consistent results (Extended Data Fig. 5c-f). Consensus clusters were more highly resolved in  
320 transcriptomic compared to AC data (Extended Data Fig. 5g), and so an integrative approach was used

321 to achieve best matched AC-level cluster annotations (Extended Data Fig. 5h-k). AC peak calling at  
322 multiple levels of cellular identity (for RNA consensus clusters, resolved AC clusters, subclasses and  
323 classes) yielded a combined total of 273,103 (human) and 134,769 (marmoset) accessible sites, with  
324 an average of 1527 or 1322 unique accessible peak fragment counts per nucleus, respectively. Gene  
325 activity estimates based on cis-regulatory interactions predicted from co-accessible promoter and distal  
326 peak regions using Cicero<sup>39</sup> were highly correlated with RNA expression values. This highlights the  
327 ability of SNARE-Seq2 to meaningfully characterize AC at RNA-defined cellular resolution that cannot  
328 be achieved using only AC data (Extended Data Fig. 6a-b). The AC-level clusters (Fig. 3a,b) that  
329 showed similar coverage across individual samples (Extended Data Fig. 6c-f) revealed regions of open  
330 chromatin that are extremely cell type specific (Fig. 3c). These regulatory regions were relatively more  
331 abundant in glutamatergic compared to GABAergic neuron subpopulations (Fig. 3c-d, Supplementary  
332 Table 14).

333

334 To better understand the interplay of gene regulation and expression, we compared transcript counts  
335 and open chromatin measured in the same nuclei. For example, the GABAergic neuron marker *GAD2*  
336 and the L2/3 glutamatergic neuron marker *CUX2* showed cell-type specific chromatin profiles for co-  
337 accessible sites that were consistent with their corresponding transcript abundances (Fig. 3e-g).  
338 Transcription factor binding site (TFBS) activities were calculated using chromVAR<sup>40</sup>, permitting  
339 discovery of differentially active TFBSs between cell types. To investigate the regulatory factors that  
340 may contribute to marker gene expression, we evaluated active TFBSs for their enrichment within  
341 marker gene co-accessible sites. This permitted direct cell type mapping of gene expression and  
342 activity levels with the expression and activity of associated regulatory factors (Fig. 3g). Using this  
343 strategy, we identified TFBS activities associated with subclass (Fig. 3h-i) and AC-cluster level  
344 differentially expressed genes (DEGs) in human and marmoset (Supplementary Table 15). DEG  
345 transcript levels and AC-inferred gene activity scores showed high correspondence (Fig. 3h). While  
346 most subclasses also showed distinct TFBS activities, correspondence between human and marmoset  
347 was higher for glutamatergic rather than GABAergic neurons (Fig. 3h,j). For GABAergic neuron

348 subclasses, gene expression profiles were more conserved than TFBS activities, consistent with fewer  
349 differences between GABAergic subpopulations based on AC sites (Fig. 3a,b). This observation is also  
350 consistent with fewer distinct TFBS activities among some inhibitory neuron subclasses (*Lamp5*, *Sncg*)  
351 in human compared to marmoset (Fig. 3h), despite these cell types having a similar number of AC peak  
352 counts (Extended Data Fig. 6d-f). Interestingly, glutamatergic neurons in L5 and L6 showed higher  
353 correspondence between primates based on TFBS activities compared to average expression,  
354 suggesting that gene regulatory processes are more highly conserved in these subclasses than target  
355 gene expression.

356

### 357 **Methylomic profiling reveals conserved gene regulation**

358 We used snmC-seq2<sup>41</sup> to profile the DNA methylome from individual cells in M1. Single-nuclei were  
359 labeled with an anti-NeuN antibody and isolated by fluorescence-activated cell sorting (FACS), and  
360 neurons were enriched (90% NeuN+ nuclei) to increase detection of rare types. Using snmC-seq2, we  
361 generated single-nucleus methylcytosine datasets from M1 of human (n = 2 donors, 6,095 nuclei),  
362 marmoset (n = 2, 6,090), and mouse (9,876) (Liu et al. companion paper) (Supplementary Table 16).  
363 On average,  $5.5 \pm 2.7\%$  (mean  $\pm$  s.d.) of human,  $5.6 \pm 2.9\%$  of marmoset and  $6.2 \pm 2.6\%$  of mouse  
364 genomes were covered by stringently filtered reads per cell, with  $3.4 \times 10^4$  (56%),  $1.8 \times 10^4$  (62%) and  
365  $4.5 \times 10^4$  (81%) genes detected per cell in the three species, respectively. Based on the DNA  
366 methylome profiles in both CpG sites (CG methylation or mCG) and non-CpG sites (CH methylation or  
367 mCH), we clustered nuclei (Methods) to group cell populations into 31 cell types in human, 36 cell types  
368 in marmoset, and 42 cell types in mouse (Fig. 4a and Extended Data Fig. 7a,b). For each species, cell  
369 type clusters could be robustly discriminated using a supervised classification model and had distinct  
370 marker genes based on DNA methylation signatures for neurons (mCH) or non-neuronal cells (mCG)  
371 (Methods). Differentially methylated regions (DMR) were determined for each cell type versus all other  
372 cell types and yielded  $9.8 \times 10^5$  DMRs in human,  $1.0 \times 10^6$  in marmoset, and  $1.8 \times 10^6$  in mouse.

373

374 We determined a consensus molecular classification of cell types in each species by integrating single-  
375 nucleus methylomic data with the Cv3 transcriptomic data described above using measurements of  
376 gene body differential methylation (CH-DMG) to approximate expression levels. Nuclei from the two  
377 data modalities mixed well as visualized in ensemble UMAPs (Fig. 4b,c). Methylation clusters have  
378 one-to-one, one-to-many, or many-to-many mapping relation to transcriptomic clusters (Fig. 1c-e and  
379 Extended Data Fig. 7d-f). DMRs were quantified for each subclass versus all other subclasses (Fig.  
380 4d), and glutamatergic neurons had more hypo-methylated DMRs compared to GABAergic neurons.  
381 Methylome tracks at subclass level can be found at [http://neomorph.salk.edu/aj2/pages/cross-species-](http://neomorph.salk.edu/aj2/pages/cross-species-M1/)  
382 [M1/](http://neomorph.salk.edu/aj2/pages/cross-species-M1/). To identify enriched transcription factor binding sites (TFBS) in each species and subclass, we  
383 performed motif enrichment analysis with hypo-methylated DMRs from one subclass against other  
384 DMRs of the same species, and identified  $102 \pm 57$  (mean  $\pm$  s.d.) TFBS in each subclass (Extended  
385 Data Fig. 8 and Supplementary Table 17). We repeated the enrichment analysis using TFBS motif  
386 clusters<sup>42</sup> and found similarly distinct subclass signatures (Supplementary Table 18). Although  
387 subclasses had unique marker genes (Fig. 2c, genes listed in Supplementary Table 8) and CH-DMG  
388 across species, they had remarkably conserved TFBS motif enrichment (Fig. 4e,f and Extended Data  
389 Fig. 8). For example, *TCF4* is robustly expressed in L5 IT neurons across species and shows  
390 significant TFBS enrichment in hypo-methylated DMRs and AC sites. DMRs and AC sites provide  
391 independent epigenomic information (Extended Data Fig. 7f,g) and can identify different TFBS  
392 enrichment, such as for *ZNF148* in L5 IT neurons. These results are consistent with previous  
393 observations of conserved TF network architectures in neural cell types between human and mouse  
394 (Stergachis et al. 2014). Conserved sets of TFs have the potential to determine conserved and  
395 divergent expression in consensus types based on shared or altered genomic locations of TFBS motifs  
396 across species.

397

#### 398 **Layer 4-like neurons in human M1**

399 M1 lacks a L4 defined by a thin band of densely packed “granular” neurons that is present in other  
400 cortical areas, such as MTG (Fig. 5a), although prior studies have identified neurons with L4-like

401 synaptic properties in mice<sup>14</sup> and expression of *RORB*, a L4 marker, in non-human primate M1<sup>43</sup>. To  
402 address the potential existence of L4-like neurons in human M1 from a transcriptomic perspective, we  
403 integrated snRNA-seq data from M1 and the granular MTG, where we previously described multiple L4  
404 glutamatergic neuron types<sup>2</sup>. This alignment revealed a broadly conserved cellular architecture  
405 between M1 and MTG (Fig. 5b,c, Extended Data Fig. 9) including M1 neuron types Exc L3 *RORB*  
406 *OTOGL* (here, *OTOGL*) and Exc L3-5 *RORB LINC01202* (here, *LINC01202*) that map closely to MTG  
407 neurons in deep L3 to L4 (Fig. 5c, red outlines). Interestingly, four MTG L2/3 IT types (*LTK*, *GLP2R*,  
408 *FREM3*, and *CARM1P1*) whose distinct physiology and morphology are reported in a companion paper  
409<sup>44</sup> had less clear homology in M1 than other types (Extended Data Fig. 9a-c), pointing to more  
410 variability across cortical areas of superficial as compared to deep glutamatergic neurons. To compare  
411 laminar positioning in M1 and MTG, the relative cortical depth from pia for each neuron was estimated  
412 based on the layer dissection and average layer thickness<sup>45</sup>. Transcriptomically similar cell types were  
413 found at similar cortical depths in M1 and MTG, and the *OTOGL* and *LINC01202* types were located in  
414 deep L3 and superficial L5 in M1 (Fig. 5d).

415

416 MTG contains three main transcriptomically-defined L4 glutamatergic neuron types (*FILIP1L*, *TWIST2*  
417 and *ESR1*) and a deep L3 type (*COL22A1*) that is found on the border of L3 and L4 (Fig. 5e-g). The M1  
418 types *OTOGL* and *LINC01202* matched one-to-one with MTG *COL22A1* and *ESR1*, whereas there  
419 were no matches for the other two MTG L4 types (Fig. 5f). Based on snRNA-seq proportions, the L4-  
420 like *OTOGL* type was much sparser in M1 than the *ESR1* type in MTG (Fig. 5e). Multiplex fluorescent in  
421 situ hybridization (mFISH) with probes to cell type marker genes confirmed these findings. The MTG  
422 *ESR1* type was highly enriched in L4,<sup>2</sup> and the homologous M1 *LINC01202* type was sparser and  
423 more widely distributed across L3 and L5 (Fig. 5g). The MTG *COL22A1* type was tightly restricted to  
424 the L3/4 border<sup>2</sup>, and the M1 *OTOGL* type was similarly found at the L3/5 border. Quantification of  
425 labeled cells as a fraction of DAPI+ cells in L3-5 showed similar frequencies of M1 *OTOGL* and MTG  
426 *COL22A1* types and 4-fold sparser M1 *LINC01202* type versus MTG *ESR1* type (Fig. 5h). These data  
427 indicate a conservation of deep L3 glutamatergic types and proportions across human cortical areas,



428 but with reduced diversity and sparsification of L4-like neurons to a single (ESR1) type in M1,  
429 distributed more broadly where L4 would be if tightly aggregated.

430

### 431 **Chandelier cells share a core molecular identity across species**

432 Conserved transcriptomic and epigenomic features of consensus types likely contribute to cell function  
433 and generate hypotheses about the gene regulatory mechanisms underlying cell type identity. Focused  
434 analysis of *Pvalb*-expressing GABAergic neurons illustrates the power of these data to predict such  
435 gene-function relationships. Cortical *Pvalb*-expressing neurons comprise two major types — basket  
436 cells (BCs) and ChCs — that have fast-spiking electrical properties and distinctive cellular  
437 morphologies. BCs selectively synapse onto the perisomatic region of glutamatergic pyramidal  
438 neurons. ChCs, also called axo-axonic cells <sup>46</sup>, selectively innervate the axon initial segment (AIS) of  
439 pyramidal cells and have unique synaptic specializations called axon cartridges. These cartridges run  
440 perpendicular to their post-synaptic target axon, giving a characteristic morphological appearance of  
441 candlesticks on a chandelier. This highly conserved feature is shown with biocytin-filled cells from  
442 mouse, rhesus macaque, and human (Fig. 6a). To reveal evolutionarily conserved transcriptomic  
443 hallmarks of ChCs, we identified DEGs in ChCs versus BCs in each species using an ROC test. 357  
444 DEGs were identified in at least one species, and marmoset ChCs shared more DEGs with human (61  
445 genes) than mouse (29; Fig. 6b, Supplementary Table 19). Remarkably, only 25 DEGs were conserved  
446 across all three species. One conserved gene, *UNC5B* (Fig. 6c), is a netrin receptor involved in axon  
447 guidance and may help target ChC to pyramidal neuron AIS. Three transcription factors (*RORA*,  
448 *TRPS1*, and *NFIB*) were conserved markers and may contribute to gene regulatory networks that  
449 determine the unique attributes of ChCs.

450

451 To determine if ChCs had enriched epigenomic signatures for *RORA* and *NFIB* (*TRPS1* lacked motif  
452 data), we compared DMRs between ChCs and BCs. In all species, *RORA* and *NFIB* had significant  
453 CH-DMGs in ChCs not BCs (Fig. 6d), consistent with differential expression. To discern if these TFs  
454 may preferentially bind to DNA in ChCs, we tested for TF motif enrichment in hypo-methylated (mCG)

455 DMRs and AC sites genome-wide. We found that the RORA motif was significantly enriched in DMRs  
456 in primates (Fig. 6d) and in AC sites of ChCs in all species (Fig. 6e, Supplementary Table 14). The  
457 NFIB binding motif was only significantly enriched in AC sites of mouse ChCs, possibly because  
458 enrichment was transient during development or NFIB specificity is due to expression alone. Three  
459 independent genomic assays converge to implicate *RORA* as a ChC-specific TF among *Pvalb*-  
460 expression neurons. Notably, 60 of 357 DEGs contained a ROR-motif in DMRs and AC regions in at  
461 least one species, further implicating *RORA* in defining ChC identity.

462

### 463 **Primate Betz cell specialization**

464 In mouse cortex, L5 glutamatergic neurons have distinct long-range projection targets (ET versus IT)  
465 and transcriptomes<sup>1</sup>. L5 ET and IT neuron subclasses clearly align between human and mouse using  
466 snRNA-seq in M1 (Extended Data Fig. 3) and in temporal<sup>2</sup> and fronto-insular cortex<sup>12</sup>. Betz cells in L5  
467 of primate M1 connect to spinal motor-neurons via the pyramidal tracts and are predicted to be L5 ET  
468 neurons. The species aligned transcriptomic types allow for the identification of genes whose  
469 expression may contribute to conserved ET versus IT features and primate-specific physiology,  
470 anatomy, and connectivity. Furthermore, Patch-seq methods that jointly measure the transcriptome,  
471 physiological properties and morphology of cells, allow the direct identification and characterization of  
472 L5 ET and IT neurons across mouse, non-human primate, and human. As primate physiology  
473 experiments are largely restricted to macaque, we also profiled L5 of macaque M1 with snRNA-seq  
474 (Cv3) to allow accurate Patch-seq mapping.

475

476 L5 ET neurons had many DEGs compared to L5 IT neurons in all 4 species. Approximately 50 DEGs  
477 were conserved across all species and similarity to human varied as a function of evolutionary distance  
478 (Fig. 7a, Supplementary Table 20). Several genes encoding ion channel subunits were enriched in ET  
479 versus IT neurons in all species, potentially mediating conserved ET physiological properties (Fig. 7b).  
480 A number of additional potassium and calcium channels were primate-enriched (Fig. 7c), potentially  
481 underlying primate-specific ET or Betz cell physiology. Interestingly, many of these primate-specific ET-

482 enriched genes showed gradually increasing ET specificity in species more closely related to human.  
483 To explore this idea of gradual evolutionary change further, we identified genes with increasing L5 ET  
484 versus IT specificity as a function of evolutionary distance from human (Fig. 7d, Supplementary Table  
485 21). Interestingly, this gene set was highly enriched for genes associated with axon guidance including  
486 members of the Robo, Slit and Ephrin gene families. These genes are potential candidates for  
487 regulating the cortico-motoneuronal connections associated with increasingly dexterous fine motor  
488 control across these species <sup>23</sup>.

489  
490 To investigate if transcriptomically defined L5 ET types contain anatomically-defined Betz cells, FISH  
491 for L5 ET neurons was combined with immunolabeling against SMI-32, a protein enriched in Betz cells  
492 and other long-range projecting neurons in macaque <sup>47-49</sup> (Fig. 7e). Cells consistent with the size and  
493 shape of Betz cells were identified in two L5 ET clusters (Exc L5 *FEZF2 ASGR2* and Exc L5 *FEZF2*  
494 *CSN1S1*). Similar to previous reports on von Economo neurons in the insular cortex <sup>12</sup>, ET clusters in  
495 M1 also included neurons with non-Betz morphologies.

496  
497 To facilitate cross-species comparisons of Betz cells and mouse ET neurons we made patch clamp  
498 recordings from L5 neurons in acute and cultured slice preparations of mouse and macaque M1. For a  
499 subset of recordings, Patch-seq analysis was applied for transcriptomic cell type identification  
500 (Extended Data Fig. 10h). To permit visualization of cells in heavily myelinated macaque M1, we used  
501 AAV viruses to drive fluorophore expression in glutamatergic neurons in macaque slice culture  
502 (Extended Data Fig. 10g). As shown in Figure 7f, Patch-seq neurons mapping to the macaque Betz/ET  
503 cluster (Exc L5 *FEZF2 LOC114676463*) had large somata (diameter > 65  $\mu\text{m}$ ) and long “tap root” basal  
504 dendrites, canonical hallmarks of Betz cell morphology <sup>17,50</sup>. A unique opportunity to record from  
505 neurosurgical tissue excised from human premotor cortex (near the confluence of the precentral and  
506 superior frontal gyri) during an epilepsy treatment surgery using the same methods as for macaque  
507 yielded multiple neurons that mapped transcriptomically to one of the Betz-containing cell types and  
508 had canonical Betz cell morphology (Fig. 7g). Macaque and human ET neurons were grouped for

509 physiological analysis because intrinsic properties were not significantly different, and many  
510 corticospinal axons originate from premotor cortex<sup>23</sup>.  
511  
512 Shared transcriptomic profiles of mouse, primate, and human L5 ET neurons predicted conservation of  
513 some physiological properties of rodent and primate neurons. Transcriptomically-defined ET neurons  
514 across species expressed high levels of genes encoding an HCN channel-subunit and a regulatory  
515 protein (*HCN1* and *PEX5L*; Fig. 7b). We hypothesized that HCN-dependent membrane properties,  
516 which are used to distinguish rodent ET from IT neurons<sup>51</sup>, would similarly separate cell types in  
517 primates. Some primate L5 neurons possessed distinctive HCN-related properties such as a lower  
518 input resistance ( $R_N$ ) and a peak resonance ( $f_R$ ) in voltage response around 3-9 Hz (Fig. 7h,i), similar to  
519 rodent ET neurons. To determine whether HCN-related physiology is a conserved feature of L5  
520 neurons, we grouped all neurons into physiologically defined ET and non-ET neurons based on their  $R_N$   
521 and  $f_R$ . We asked whether these physiologically-defined neurons corresponded to genetically-defined  
522 ET/Betz or non-ET neurons using Patch-seq and cell-type specific mouse lines. For mouse M1, the ET-  
523 specific *Thy1-YFP*<sup>21,52</sup> and IT specific *Etv1-EGFP*<sup>53</sup> mouse lines preferentially labeled physiologically  
524 defined ET and non-ET neurons, respectively (Fig. 7j). For primates, transcriptomically-defined Betz  
525 cells were physiologically defined ET neurons, whereas transcriptomically defined non-ET neurons  
526 were physiologically defined non-ET neurons (Fig. 7k). Thus, there was broad correspondence  
527 between physiologically-defined and genetically-defined ET neurons in both mouse and primate M1.  
528 There were notable differences in physiology between mouse and primate ET neurons, however. A  
529 greater fraction of primate ET neurons exhibited an exceptionally low  $R_N$  compared to mouse (Fig. 7l).  
530 Additional differences in action potential properties across cell types and species may be explained in  
531 part by differences in the expression of ion channel-related genes (Fig. 7c, Extended Data Fig. 10).  
532  
533 Most strikingly, primate Betz/ET neurons displayed a distinctive biphasic-firing pattern during long spike  
534 trains. The firing rate of both primate and mouse non-ET neurons decreased to a steady state within  
535 the first second of a 10 second depolarizing current injection, whereas the firing rate of mouse ET

536 neurons increased moderately over the same time period (Fig. 7m,n; Extended Data Fig. 10m,n). The  
537 acceleration in rodent ET neurons has been attributed to the expression of Kv1-containing voltage-  
538 gated  $K^+$  channels that are encoded by genes like the conserved ET gene *KCNA1*. In macaque and  
539 human ET/Betz neurons, a distinctive biphasic pattern was characterized by an early cessation of firing  
540 followed by a sustained and dramatic increase in firing later in the current injection. Thus, while ET  
541 neurons in both primate and rodent M1 displayed spike frequency acceleration, the temporal dynamics  
542 and magnitude of this acceleration appears to be a unique feature of primate ET/Betz neurons. These  
543 data emphasize how transcriptomic data from this specialized neuron type can be linked to shared and  
544 unique physiological properties across species.

545

## 546 Discussion

547 Comparative analysis is a powerful strategy to understand brain structure and function. Species  
548 conservation is strong evidence for functional relevance under evolutionary constraints that can help  
549 identify critical molecular and regulatory mechanisms<sup>54,55</sup>. Conversely, divergence indicates adaptive  
550 specialization, which may be essential to understand the mechanistic underpinnings of human brain  
551 function and susceptibility to human-specific diseases. In the current study, we applied a comparative  
552 approach to understand conserved and species-specific features of M1 at the level of cell types using  
553 single-nucleus RNA-seq (Cv3 and SSV4), open chromatin (SNARE-seq2 and ATAC-seq) and DNA-  
554 methylation (snmC-seq2) technologies. Integrated analysis of over 450,000 nuclei in human, non-  
555 human primates (marmoset, a New World monkey, and to a lesser degree macaque, an Old World  
556 monkey that is evolutionarily more closely related to humans), and mouse (see also companion paper  
557 <sup>6</sup>) yielded a high-resolution, multimodal classification of cell types in each species, and a coarser  
558 consensus classification conserved between rodent and primate lineages. Robust species conservation  
559 strongly argues for the functional relevance of this consensus cellular architecture. Species  
560 specializations are also apparent, both in the additional granularity in cell types within species and  
561 differences between conserved cell types. A comparative evolutionary approach provides an anchor  
562 point to define the cellular architecture of any tissue and to discover species-specific adaptations.

563

564 A key result of the current study is the identification of a consensus classification of cell types across  
565 species that allows the comparison of relative similarities in human compared to common mammalian  
566 model organisms in biomedical research. Prior studies have demonstrated that high resolution cellular  
567 taxonomies can be generated in mouse, non-human primate and human cortex, and that there is  
568 generally good concordance across species<sup>2,11</sup>. However, inconsistencies in the methods and  
569 sampling depths used made strong conclusions difficult, compounded by the analysis of different  
570 cortical regions in different species. The current study overcame these challenges by focusing on M1, a  
571 functionally and anatomically conserved cortical region across mammals, and comparing a variety of  
572 methods on similarly isolated tissues (and the same specimens from human and marmoset). Several  
573 important points emerged from these integrated analyses. First, with deeper sampling and the same  
574 methodology (snRNA-seq with Cv3), a similar cellular complexity on the order of 100 cell types was  
575 seen in all three species. The highest resolution molecular classification was seen with RNA-seq  
576 compared to epigenomic methods, and among RNA-seq methods with those that allow the most cells  
577 to be analyzed. Strikingly, the molecular classifications were well aligned across all methods tested,  
578 albeit at different levels of resolution as a function of the information content of the assay and the  
579 number of cells profiled. All methods were consistent at the level of subclasses as defined above, both  
580 across methods and species; significantly better alignment was achieved among species based on  
581 transcriptomics, and with epigenomic methods in some subclasses. Mismatches in cellular sampling  
582 affect the ability to compare across species; for example, higher non-neuronal sampling in mouse and  
583 marmoset increased detection of rare cell types compared to human. One important comparison was  
584 between plate-based (SSv4) and droplet-based (Cv3) RNA-seq of human nuclei, where we compared  
585 results between approximately 10,000 SSv4 and 100,000 Cv3 nuclei. On average, SSv4 detected 30%  
586 more genes per nucleus and enabled comparisons of isoform usage between cell types, albeit with 20-  
587 fold greater sequencing depth. However, SSv4 cost 10 times as much as Cv3 and did not allow  
588 detection of additional cell types.

589

590 The snmC-seq2 clustering aligned closely with the transcriptomic classification, although with  
591 significantly lower resolution in rarer subclasses. Hypo-methylated sites correlated with gene  
592 expression and specific transcription factor binding motifs were enriched in cell type specific sites.  
593 Multi-omic SNARE-seq2 measured RNA profiles of nuclei that allowed high confidence assignment to  
594 transcriptomic clusters. Examining accessible chromatin (AC) regions within the same nuclei led to  
595 strong correlations between cell subclass or type gene expression and active regulatory regions of  
596 open chromatin. Using this strategy, gene regulatory activities could be identified within RNA-defined  
597 cell populations (including RNA consensus clusters) that could not be resolved from AC data alone  
598 (Extended Data Fig. 6a, Supplementary Table 15). By joint consideration of these epigenomic  
599 modalities, glutamatergic neurons were found to have more hypo-methylated DMRs and differentially  
600 accessible chromatin, consistent with having larger somata and expressing more genes. Within-  
601 species, cell types have many more unique AC sites than uniquely expressed marker genes. At the  
602 same time, there is striking conservation across species of subclass TFBS motif enrichment within AC  
603 and hypo-methylated DMRs. Most subclasses have distinct motifs, although L2/3 and L6 IT and *Lamp5*  
604 and *Sncg* subclasses share many motifs and are more clearly distinguished based on gene expression.  
605 Taken together, these results show a robust cell type classification that is consistent at the level of  
606 subclasses both across transcriptomic and chromatin measures and across species, with additional cell  
607 type-level granularity identified with transcriptomics.

608

609 Alignment across species allowed a comparison of relative similarities and differences between  
610 species. A common (and expected) theme was that more closely related species are more similar to  
611 one another. This was true at the level of gene expression and epigenome patterning across cell types,  
612 and in the precision with which transcriptomically-defined cell types could be aligned across species.  
613 For example, human and marmoset GABAergic types could be aligned at higher resolution than human  
614 and mouse. Human was more similar to macaque than to marmoset. This indicates that cell type  
615 similarity increases as a function of evolutionary distance to our closest common ancestors with mouse  
616 (~70 mya), marmoset (~40 mya), and macaque (~25 mya). Interestingly, many gene expression

617 differences may change gradually over evolution. This is apparent in the graded changes in expression  
618 levels of genes enriched in L5 ET versus L5 IT neurons and in the reduced performance of cell type  
619 classification based on marker gene expression that is correlated with evolutionary distance between  
620 species.

621

622 Several prominent species differences in cell type proportions were observed. First, the ratio of  
623 glutamatergic excitatory projection neurons compared to GABAergic inhibitory interneurons was 2:1 in  
624 human compared to 3:1 in marmoset and 5:1 in mouse and leads to a profound shift in the overall  
625 excitation-inhibition balance of the cortex. A similar species difference has been described based on  
626 histological measures (reviewed in <sup>28</sup>), indicating that snRNA-seq gives a reasonably accurate  
627 measurement of cell type proportions. Surprisingly, the relative proportions of GABAergic subclasses  
628 and types were similar across species. These results suggest a developmental shift in the size of the  
629 GABAergic progenitor pool in the ganglionic eminences or an extended period of neurogenesis and  
630 migration. A decreased proportion of the subcortically targeting L5 ET neurons in human was also  
631 seen, as previously shown in temporal <sup>2</sup> and frontoinsular <sup>12</sup> cortex. This shift likely reflects the  
632 evolutionary increase in cortical neurons relative to their subcortical targets <sup>56</sup> and was less prominent  
633 in M1, suggesting regional variation in the proportion of L5 ET neurons. Finally, a large increase in the  
634 proportion of L2 and L3 IT neurons was seen in human compared to mouse and marmoset. This  
635 increase parallels the disproportionate expansion of human cortical area and supragranular layers that  
636 contain neurons projecting to other parts of the cortex, presumably to facilitate greater corticocortical  
637 communication. Interestingly, L2 and L3 IT neurons appear to be particularly highly variable across  
638 cortical areas and species, and also are more diverse and specialized in human compared to mouse  
639 (see companion paper <sup>44</sup>).

640

641 A striking and somewhat paradoxical observation is the high degree of species specialization of  
642 consensus types. The majority of DEGs between cell types were consistently species-specific. This  
643 result suggests that the conserved cellular features of a cell type are largely due to a minority of DEGs



644 with conserved expression patterns. The current study demonstrates this point for one of the most  
645 distinctive brain cell types, the cortical *Pvalb*-expressing GABAergic ChC. ChCs in mouse, non-human  
646 primate, and human have 100-150 genes with highly enriched expression compared to other *Pvalb*-  
647 expressing interneurons (BCs); however, only 25 of these ChC-enriched genes are shared across  
648 species. This small overlapping gene set includes several transcription factors and a member of the  
649 netrin family (*UNC5B*) that could be responsible for AIS targeting. Binding sites for these TFs are  
650 enriched in ChC cluster regions of open chromatin and in hypo-methylated regions around ChC-  
651 enriched genes. While these associations between genes and cellular phenotypes for conserved and  
652 divergent features remain to be tested, a comparative strategy can identify these core conserved genes  
653 and make strong predictions about the TF code for cell types and the genes responsible for their  
654 evolutionarily constrained functions.

655

656 M1 is an agranular cortex lacking a L4, although a recent study demonstrated that there are neurons  
657 with L4-like properties in mouse<sup>14</sup>. Here we confirm and extend this finding in human M1. We find a L4-  
658 like neuron type in M1 that aligns to a L4 type in human MTG and is scattered between the deep part of  
659 L3 and the superficial part of L5 where L4 would be if aggregated into a layer. However, MTG  
660 contained several additional L4 types not found in M1, and with a much higher frequency. The human  
661 M1 L4-like type is part of the L5 IT\_1 consensus cluster that includes several IT types in all species,  
662 including two L4-like types in mouse (L4/5 IT\_1 and L4/5 IT\_2) that also express the canonical L4  
663 marker *Rorb* (see companion paper<sup>6</sup>). Therefore, it appears that M1 has L4-like cells from a  
664 transcriptomic perspective, but only a subset of the types compared to granular cortical areas, at much  
665 lower density, and scattered rather than aggregated into a tight layer.

666

667 The most distinctive cellular hallmark of M1 in primates and cats is the enormous Betz cell, which  
668 contributes to direct corticospinal connections to spinal motoneurons in primates that participate in fine  
669 motor control<sup>15,16,57-59</sup>. Intracellular recordings from cats have shown highly distinctive characteristics  
670 including HCN channel-related membrane properties, spike frequency acceleration, and extremely fast

671 maintained firing rates<sup>19,20</sup>. However, they have never been recorded in primates using patch clamp  
672 physiology due to the high degree of myelination in M1 that prevents their visualization, and the inability  
673 to obtain motor cortex tissue from neurosurgical procedures which are careful to be function-sparing. A  
674 goal of the current project was to identify the transcriptomic cluster corresponding to Betz cells and use  
675 this to understand gene expression that may underlie their distinctive properties and species  
676 specializations. We have recently taken a similar approach to study von Economo neurons in the  
677 fronto-insular cortex, showing they are found within a transcriptomic class consisting of ET neurons<sup>12</sup>.  
678 Betz cells are classical ET neurons that, together with the axons of smaller corticospinal neurons, make  
679 up part of the pyramidal tract from the cortex to the spinal cord<sup>16,60</sup>. We show that neurons with Betz  
680 cell morphology label with markers for the M1 ET clusters. Like von Economo neurons, there does not  
681 appear to be an exclusively Betz transcriptomic type. Rather, M1 ET clusters are not exclusive for  
682 neurons with Betz morphology, and we find more than one ET cluster contains neurons with Betz  
683 morphology.

684

685 Although comparative transcriptomic alignments provide strong evidence for functional similarity, the  
686 distinctions between corticospinal neurons across species or even between L5 ET and IT neuron types  
687 in primates or humans has not been demonstrated physiologically. We recently developed a suite of  
688 methodologies for studying specific neuron types in human and non-human tissues, including triple  
689 modality Patch-seq to combine physiology, morphology and transcriptome analysis, acute and cultured  
690 slice physiology in adult human neurosurgical resections and macaque brain, and AAV-based neuronal  
691 labeling to allow targeting of neurons in highly myelinated tissues (companion paper<sup>44, 61</sup>). Specifically,  
692 these tools allow the targeting of L5 neurons in mouse and non-human primate and the assignment of  
693 neurons to their transcriptomic types using Patch-seq, which we facilitated by generating and aligning a  
694 L5 transcriptomic classification in macaque where such analyses could be performed. We show here  
695 that several of the characteristic features of L5 ET versus IT neurons are conserved, and can be  
696 reliably resolved from one another in mouse and non-human primate. Furthermore, macaque neurons  
697 with Betz-like morphologies mapped to the Betz-containing clusters. However, as predicted by

698 differences in ion channel-related gene expression, not all physiological features were conserved  
699 between macaque and mouse ET neurons. Betz/ET neurons had the distinctive pauses, bursting and  
700 spike-frequency acceleration described previously in cats but not seen in rodents<sup>19,20</sup>. Finally, we had  
701 access to an extremely rare human neurosurgical case where a region of premotor cortex was  
702 resected. Similar to macaque M1, this premotor region contained large neurons with characteristic  
703 Betz-like morphology that mapped transcriptomically to the Betz-containing clusters. Together these  
704 results highlight the predictive power of transcriptomic mapping and cross-species inference of cell  
705 types for L5 pyramidal neurons including the Betz cells. Furthermore, these data are consistent with  
706 observations that Betz cells may not in fact be completely restricted to M1 but distribute across other  
707 proximal motor-related areas that contribute to the pyramidal tract<sup>62</sup>. Finally, a number of ion channels  
708 that may contribute to conserved ET versus IT features as well as species specializations of Betz cell  
709 function were identified that provide candidate genes to explore gene-function relationships. For  
710 example, axon guidance-associated genes are enriched in Betz-containing ET neuron types in  
711 primates, possibly explaining why Betz cells in primates directly contact spinal motor neurons rather  
712 than spinal interneurons as in rodents. Thus, as the comparative approach is helpful in identifying core  
713 conserved molecular programs, it may be equally valuable to understand what is different in human or  
714 can be well modeled in closer non-human primate relatives. This is particularly relevant in the context of  
715 Betz cells and other ET neuron types that are selectively vulnerable in amyotrophic lateral sclerosis,  
716 some forms of frontotemporal dementia, and other neurodegenerative conditions.

717

## 718 References

- 719 1. Tasic, B. *et al.* Shared and distinct transcriptomic cell types across neocortical areas. *Nature* **563**,  
720 72–78 (2018).
- 721 2. Hodge, R. D. *et al.* Conserved cell types with divergent features in human versus mouse cortex.  
722 *Nature* **573**, 61–68 (2019).
- 723 3. Tasic, B. *et al.* Adult mouse cortical cell taxonomy revealed by single cell transcriptomics. *Nat.*  
724 *Neurosci.* **19**, 335–346 (2016).
- 725 4. Lake, B. B. *et al.* Neuronal subtypes and diversity revealed by single-nucleus RNA sequencing of  
726 the human brain. *Science* **352**, 1586–1590 (2016).
- 727 5. Luo, C. *et al.* Single-cell methylomes identify neuronal subtypes and regulatory elements in  
728 mammalian cortex. *Science* **357**, 600–604 (2017).
- 729 6. Yao, Z. *et al.* An integrated transcriptomic and epigenomic atlas of mouse primary motor cortex cell  
730 types. *bioRxiv* 2020.02.29.970558 (2020) doi:10.1101/2020.02.29.970558.
- 731 7. Lake, B. B. *et al.* Integrative single-cell analysis of transcriptional and epigenetic states in the  
732 human adult brain. *Nat. Biotechnol.* **36**, 70–80 (2018).
- 733 8. Zeisel, A. *et al.* Brain structure. Cell types in the mouse cortex and hippocampus revealed by  
734 single-cell RNA-seq. *Science* **347**, 1138–1142 (2015).
- 735 9. Gray, L. T. *et al.* Layer-specific chromatin accessibility landscapes reveal regulatory networks in  
736 adult mouse visual cortex. *Elife* **6**, (2017).
- 737 10. Lee, D.-S. *et al.* Simultaneous profiling of 3D genome structure and DNA methylation in single  
738 human cells. *Nat. Methods* **16**, 999–1006 (2019).
- 739 11. Krienen, F. M., Goldman, M., Zhang, Q. & del Rosario, R. Innovations in primate interneuron  
740 repertoire. *bioRxiv* (2019).
- 741 12. Hodge, R. D. *et al.* Transcriptomic evidence that von Economo neurons are regionally specialized  
742 extratelencephalic-projecting excitatory neurons. *Nat. Commun.* **11**, 1172 (2020).
- 743 13. La Manno, G. *et al.* Molecular Diversity of Midbrain Development in Mouse, Human, and Stem

- 744 Cells. *Cell* **167**, 566–580.e19 (2016).
- 745 14. Yamawaki, N., Borges, K., Suter, B. A., Harris, K. D. & Shepherd, G. M. G. A genuine layer 4 in  
746 motor cortex with prototypical synaptic circuit connectivity. *Elife* **3**, e05422 (2014).
- 747 15. Betz, W. Anatomischer Nachweis zweier Gehirncentra. *Zentralbl Med Wiss* **12**, (1874).
- 748 16. Lassek, A. M. The Human Pyramidal Tract II. A Numerical Investigation of the Betz Cells of the  
749 Motor Area. *J. Nerv. Ment. Dis.* **94**, 225–226 (1941).
- 750 17. Jacobs, B. *et al.* Comparative morphology of gigantopyramidal neurons in primary motor cortex  
751 across mammals. *J. Comp. Neurol.* **526**, 496–536 (2018).
- 752 18. Kaiserman-Abramof, I. R. & Peters, A. Some aspects of the morphology of Betz cells in the  
753 cerebral cortex of the cat. *Brain Res.* **43**, 527–546 (1972).
- 754 19. Spain, W. J., Schwindt, P. C. & Crill, W. E. Post-inhibitory excitation and inhibition in layer V  
755 pyramidal neurones from cat sensorimotor cortex. *The Journal of Physiology* vol. 434 609–626  
756 (1991).
- 757 20. Chen, W., Zhang, J. J., Hu, G. Y. & Wu, C. P. Electrophysiological and morphological properties of  
758 pyramidal and nonpyramidal neurons in the cat motor cortex in vitro. *Neuroscience* **73**, 39–55  
759 (1996).
- 760 21. Miller, M. N., Okaty, B. W. & Nelson, S. B. Region-Specific Spike-Frequency Acceleration in Layer  
761 5 Pyramidal Neurons Mediated by Kv1 Subunits. *Journal of Neuroscience* vol. 28 13716–13726  
762 (2008).
- 763 22. Gu, Z. *et al.* Control of species-dependent cortico-motoneuronal connections underlying manual  
764 dexterity. *Science* **357**, 400–404 (2017).
- 765 23. Lemon, R. N. Descending pathways in motor control. *Annu. Rev. Neurosci.* **31**, 195–218 (2008).
- 766 24. Stuart, T. *et al.* Comprehensive Integration of Single-Cell Data. *Cell* **177**, 1888–1902.e21 (2019).
- 767 25. Oberheim, N. A. *et al.* Uniquely Hominid Features of Adult Human Astrocytes. *Journal of*  
768 *Neuroscience* vol. 29 3276–3287 (2009).
- 769 26. Colombo, J. A. The interlaminar glia: from serendipity to hypothesis. *Brain Struct. Funct.* **222**,  
770 1109–1129 (2017).

- 771 27. Bakken, T. E. *et al.* Single-nucleus and single-cell transcriptomes compared in matched cortical  
772 cell types. *PLoS One* **13**, e0209648 (2018).
- 773 28. Džaja, D., Hladnik, A., Bičanić, I., Baković, M. & Petanjek, Z. Neocortical calretinin neurons in  
774 primates: increase in proportion and microcircuitry structure. *Front. Neuroanat.* **8**, 103 (2014).
- 775 29. DeFelipe, J., Alonso-Nanclares, L. & Arellano, J. I. Microstructure of the neocortex: comparative  
776 aspects. *J. Neurocytol.* **31**, 299–316 (2002).
- 777 30. Crow, M., Paul, A., Ballouz, S., Huang, Z. J. & Gillis, J. Characterizing the replicability of cell types  
778 defined by single cell RNA-sequencing data using MetaNeighbor. *Nat. Commun.* **9**, 884 (2018).
- 779 31. Boldog, E. *et al.* Transcriptomic and morphophysiological evidence for a specialized human cortical  
780 GABAergic cell type. *Nat. Neurosci.* **21**, 1185–1195 (2018).
- 781 32. Paul, A. *et al.* Transcriptional Architecture of Synaptic Communication Delineates GABAergic  
782 Neuron Identity. *Cell* **171**, 522–539.e20 (2017).
- 783 33. Verkhratsky, A. & Nedergaard, M. The homeostatic astroglia emerges from evolutionary  
784 specialization of neural cells. *Philos. Trans. R. Soc. Lond. B Biol. Sci.* **371**, (2016).
- 785 34. Nortley, R. *et al.* Amyloid  $\beta$  oligomers constrict human capillaries in Alzheimer's disease via  
786 signaling to pericytes. *Science* vol. 365 eaav9518 (2019).
- 787 35. La Manno, G. *et al.* RNA velocity of single cells. *Nature* **560**, 494–498 (2018).
- 788 36. Riccomagno, M. M. *et al.* The RacGAP  $\beta$ 2-Chimaerin selectively mediates axonal pruning in the  
789 hippocampus. *Cell* **149**, 1594–1606 (2012).
- 790 37. Chen, S., Lake, B. B. & Zhang, K. High-throughput sequencing of the transcriptome and chromatin  
791 accessibility in the same cell. *Nat. Biotechnol.* **37**, 1452–1457 (2019).
- 792 38. Nongluk Plongthongkum, Dinh Diep, Song Chen, Blue B. Lake, Kun Zhang. Scalable Dual-omic  
793 Profiling with Single-nucleus Chromatin Accessibility and mRNA Expression Sequencing 2  
794 (SNARE-Seq2). (2020).
- 795 39. Pliner, H. A. *et al.* Cicero Predicts cis-Regulatory DNA Interactions from Single-Cell Chromatin  
796 Accessibility Data. *Mol. Cell* **71**, 858–871.e8 (2018).
- 797 40. Schep, A. N., Wu, B., Buenrostro, J. D. & Greenleaf, W. J. chromVAR: inferring transcription-

- 798 factor-associated accessibility from single-cell epigenomic data. *Nat. Methods* **14**, 975–978 (2017).
- 799 41. Luo, C. *et al.* Robust single-cell DNA methylome profiling with snmC-seq2. *Nat. Commun.* **9**, 3824  
800 (2018).
- 801 42. Fornes, O. *et al.* JASPAR 2020: update of the open-access database of transcription factor binding  
802 profiles. *Nucleic Acids Res.* **48**, D87–D92 (2020).
- 803 43. Bernard, A. *et al.* Transcriptional architecture of the primate neocortex. *Neuron* **73**, 1083–1099  
804 (2012).
- 805 44. Berg, J. *et al.* Human cortical expansion involves diversification and specialization of supragranular  
806 intratelencephalic-projecting neurons. (2020).
- 807 45. von Economo, C. & Koskinas, G. N. *Die Cytoarchitektonik der Hirnrinde des Erwachsenen*  
808 *Menschen*. (J. Springer, 1925).
- 809 46. Somogyi, P., Freund, T. F. & Cowey, A. The axo-axonic interneuron in the cerebral cortex of the  
810 rat, cat and monkey. *Neuroscience* **7**, 2577–2607 (1982).
- 811 47. Hof, P. R., Nimchinsky, E. A. & Morrison, J. H. Neurochemical phenotype of corticocortical  
812 connections in the macaque monkey: quantitative analysis of a subset of neurofilament protein-  
813 immunoreactive projection neurons in frontal, parietal, temporal, and cingulate cortices. *J. Comp.*  
814 *Neurol.* **362**, 109–133 (1995).
- 815 48. Tsang, Y. M., Chiong, F., Kuznetsov, D., Kasarskis, E. & Geula, C. Motor neurons are rich in non-  
816 phosphorylated neurofilaments: cross-species comparison and alterations in ALS. *Brain Res.* **861**,  
817 45–58 (2000).
- 818 49. Preuss, T. M., Stepniowska, I., Jain, N. & Kaas, J. H. Multiple divisions of macaque precentral  
819 motor cortex identified with neurofilament antibody SMI-32. *Brain Research* vol. 767 148–153  
820 (1997).
- 821 50. Scheibel, M. E., Davies, T. L., Lindsay, R. D. & Scheibel, A. B. Basilar dendrite bundles of giant  
822 pyramidal cells. *Exp. Neurol.* **42**, 307–319 (1974).
- 823 51. Baker, A. *et al.* Specialized Subpopulations of Deep-Layer Pyramidal Neurons in the Neocortex:  
824 Bridging Cellular Properties to Functional Consequences. *J. Neurosci.* **38**, 5441–5455 (2018).

- 825 52. Feng, G. *et al.* Imaging neuronal subsets in transgenic mice expressing multiple spectral variants  
826 of GFP. *Neuron* **28**, 41–51 (2000).
- 827 53. Groh, A. *et al.* Cell-Type Specific Properties of Pyramidal Neurons in Neocortex Underlying a  
828 Layout that Is Modifiable Depending on the Cortical Area. *Cerebral Cortex* vol. 20 826–836 (2010).
- 829 54. Tosches, M. A. *et al.* Evolution of pallium, hippocampus, and cortical cell types revealed by single-  
830 cell transcriptomics in reptiles. *Science* **360**, 881–888 (2018).
- 831 55. Arendt, D. *et al.* The origin and evolution of cell types. *Nat. Rev. Genet.* **17**, 744–757 (2016).
- 832 56. Herculano-Houzel, S., Catania, K., Manger, P. R. & Kaas, J. H. Mammalian Brains Are Made of  
833 These: A Dataset of the Numbers and Densities of Neuronal and Nonneuronal Cells in the Brain of  
834 Glires, Primates, Scandentia, Eulipotyphlans, Afrotherians and Artiodactyls, and Their Relationship  
835 with Body Mass. *Brain Behav. Evol.* **86**, 145–163 (2015).
- 836 57. Rivara, C.-B., Sherwood, C. C., Bouras, C. & Hof, P. R. Stereologic characterization and spatial  
837 distribution patterns of Betz cells in the human primary motor cortex. *Anat. Rec. A Discov. Mol.*  
838 *Cell. Evol. Biol.* **270**, 137–151 (2003).
- 839 58. Evarts, E. V. Representation of movements and muscles by pyramidal tract neurons of the  
840 precentral motor cortex. in *Neurophysiological basis of normal and abnormal motor activities* 215–  
841 253 (Raven Press New York, 1967).
- 842 59. Evarts, E. V. RELATION OF DISCHARGE FREQUENCY TO CONDUCTION VELOCITY IN  
843 PYRAMIDAL TRACT NEURONS. *J. Neurophysiol.* **28**, 216–228 (1965).
- 844 60. Lassek, A. M. THE PYRAMIDAL TRACT: A STUDY OF RETROGRADE DEGENERATION IN THE  
845 MONKEY. *Arch NeurPsych* **48**, 561–567 (1942).
- 846 61. Ting, J. T. *et al.* A robust ex vivo experimental platform for molecular-genetic dissection of adult  
847 human neocortical cell types and circuits. *Sci. Rep.* **8**, 8407 (2018).
- 848 62. Vigneswaran, G., Kraskov, A. & Lemon, R. N. Large Identified Pyramidal Cells in Macaque Motor  
849 and Premotor Cortex Exhibit ‘Thin Spikes’: Implications for Cell Type Classification. *Journal of*  
850 *Neuroscience* vol. 31 14235–14242 (2011).
- 851 63. Krimer, L. S. *et al.* Cluster Analysis–Based Physiological Classification and Morphological



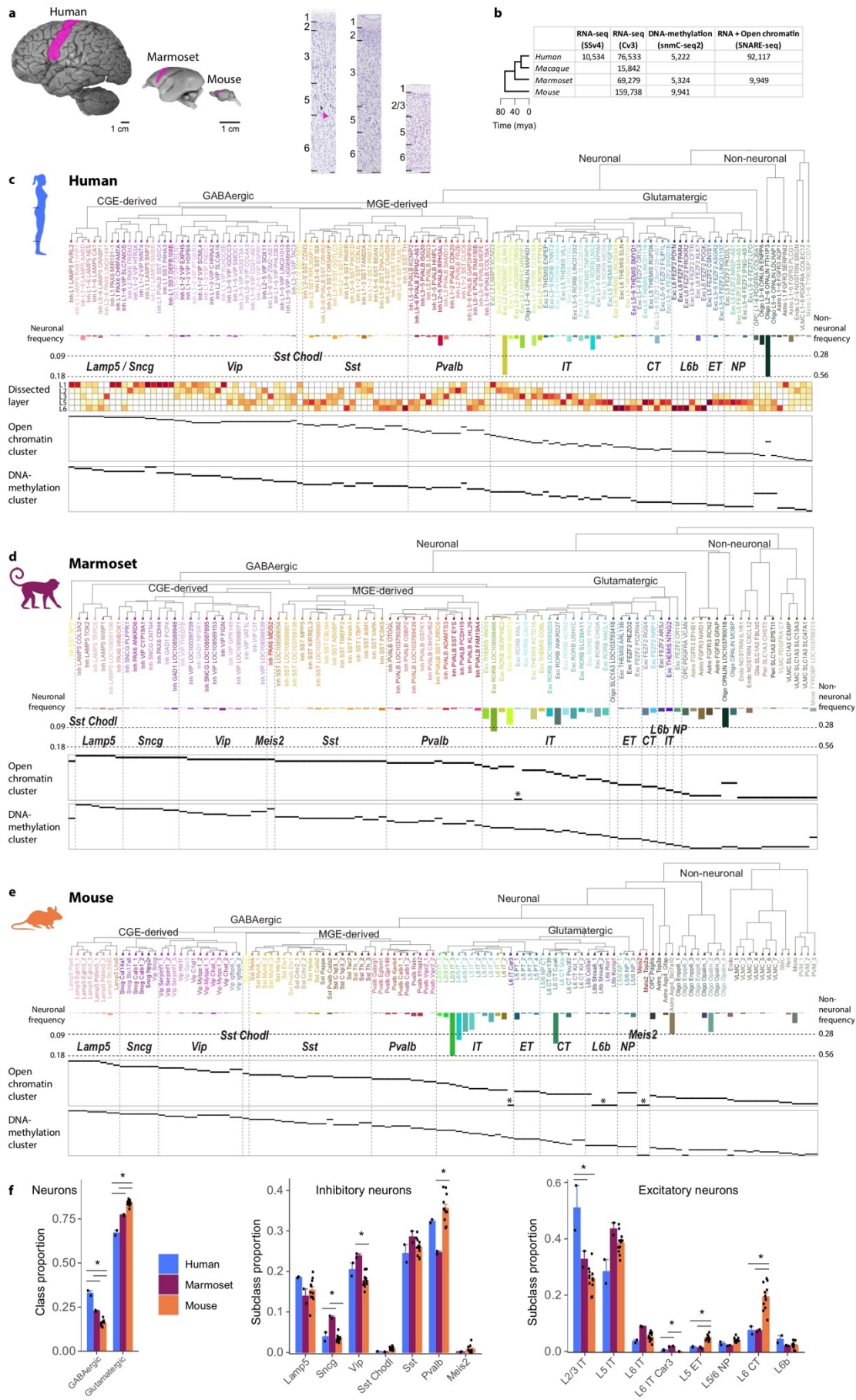
- 852 Properties of Inhibitory Neurons in Layers 2–3 of Monkey Dorsolateral Prefrontal Cortex. *J.*  
853 *Neurophysiol.* **94**, 3009–3022 (2005).
- 854 64. Rotaru, D. C. *et al.* Functional properties of GABA synaptic inputs onto GABA neurons in monkey  
855 prefrontal cortex. *J. Neurophysiol.* **113**, 1850–1861 (2015).
- 856 65. Fetz, E. E., Cheney, P. D., Mewes, K. & Palmer, S. Control of forelimb muscle activity by  
857 populations of corticomotoneuronal and rubromotoneuronal cells. *Prog. Brain Res.* **80**, 437–49;  
858 discussion 427–30 (1989).
- 859 66. Mi, H., Muruganujan, A., Ebert, D., Huang, X. & Thomas, P. D. PANTHER version 14: more  
860 genomes, a new PANTHER GO-slim and improvements in enrichment analysis tools. *Nucleic*  
861 *Acids Res.* **47**, D419–D426 (2019).
- 862 67. Koopmans, F. *et al.* SynGO: An Evidence-Based, Expert-Curated Knowledge Base for the  
863 Synapse. *Neuron* **103**, 217–234.e4 (2019).
- 864 68. Luo, C. *et al.* Single nucleus multi-omics links human cortical cell regulatory genome diversity to  
865 disease risk variants. *bioRxiv* 2019.12.11.873398 (2019) doi:10.1101/2019.12.11.873398.
- 866 69. Amemiya, H. M., Kundaje, A. & Boyle, A. P. The ENCODE Blacklist: Identification of Problematic  
867 Regions of the Genome. *Sci. Rep.* **9**, 9354 (2019).
- 868 70. Wolf, F. A., Angerer, P. & Theis, F. J. SCANPY: large-scale single-cell gene expression data  
869 analysis. *Genome Biol.* **19**, 15 (2018).
- 870 71. Traag, V. A., Waltman, L. & van Eck, N. J. From Louvain to Leiden: guaranteeing well-connected  
871 communities. *Sci. Rep.* **9**, 5233 (2019).
- 872 72. Guyon, I., Weston, J., Barnhill, S. & Vapnik, V. Gene Selection for Cancer Classification using  
873 Support Vector Machines. *Mach. Learn.* **46**, 389–422 (2002).
- 874 73. Brodersen, K. H., Ong, C. S., Stephan, K. E. & Buhmann, J. M. The Balanced Accuracy and Its  
875 Posterior Distribution. in *2010 20th International Conference on Pattern Recognition* 3121–3124  
876 (2010).
- 877 74. Lemaître, G., Nogueira, F. & Aridas, C. K. Imbalanced-learn: A Python Toolbox to Tackle the  
878 Curse of Imbalanced Datasets in Machine Learning. *J. Mach. Learn. Res.* **18**, 1–5 (2017).

- 879 75. Hie, B., Bryson, B. & Berger, B. Efficient integration of heterogeneous single-cell transcriptomes  
880 using Scanorama. *Nat. Biotechnol.* **37**, 685–691 (2019).
- 881 76. He, Y. *et al.* Spatiotemporal DNA Methylome Dynamics of the Developing Mammalian Fetus.  
882 doi:10.1101/166744.
- 883 77. McLeay, R. C. & Bailey, T. L. Motif Enrichment Analysis: a unified framework and an evaluation on  
884 ChIP data. *BMC Bioinformatics* **11**, 165 (2010).
- 885 78. Palmer, C., Liu, C. & Chun, J. Nuclei Isolation for SNARE-seq2 v1 (protocols.io.8tvhwn6).  
886 doi:10.17504/protocols.io.8tvhwn6.
- 887 79. Lun, A. T. L. *et al.* EmptyDrops: distinguishing cells from empty droplets in droplet-based single-  
888 cell RNA sequencing data. *Genome Biol.* **20**, 63 (2019).
- 889 80. Gayoso, A. & Shor, J. *GitHub: DoubletDetection*. (2019). doi:10.5281/zenodo.2678042.
- 890 81. Hahne, F. & Ivanek, R. Visualizing Genomic Data Using Gviz and Bioconductor. *Methods Mol. Biol.*  
891 **1418**, 335–351 (2016).
- 892 82. Buenrostro, J. D. *et al.* Single-cell chromatin accessibility reveals principles of regulatory variation.  
893 *Nature* **523**, 486–490 (2015).
- 894 83. Cusanovich, D. A. *et al.* Multiplex single-cell profiling of chromatin accessibility by combinatorial  
895 cellular indexing. *Science* vol. 348 910–914 (2015).
- 896 84. Yue, F. *et al.* A comparative encyclopedia of DNA elements in the mouse genome. *Nature* **515**,  
897 355–364 (2014).
- 898 85. Levine, J. H. *et al.* Data-Driven Phenotypic Dissection of AML Reveals Progenitor-like Cells that  
899 Correlate with Prognosis. *Cell* **162**, 184–197 (2015).
- 900 86. Graybuck, L. T. *et al.* Prospective, brain-wide labeling of neuronal subclasses with enhancer-driven  
901 AAVs. (2019) doi:10.1101/525014.
- 902 87. Ting, J. T., Daigle, T. L., Chen, Q. & Feng, G. Acute brain slice methods for adult and aging  
903 animals: application of targeted patch clamp analysis and optogenetics. *Methods Mol. Biol.* **1183**,  
904 221–242 (2014).
- 905 88. Chan, K. Y. *et al.* Engineered AAVs for efficient noninvasive gene delivery to the central and

906 peripheral nervous systems. *Nat. Neurosci.* **20**, 1172–1179 (2017).

907 89. Rudy, B. & McBain, C. J. Kv3 channels: voltage-gated K<sup>+</sup> channels designed for high-frequency  
908 repetitive firing. *Trends Neurosci.* **24**, 517–526 (2001).

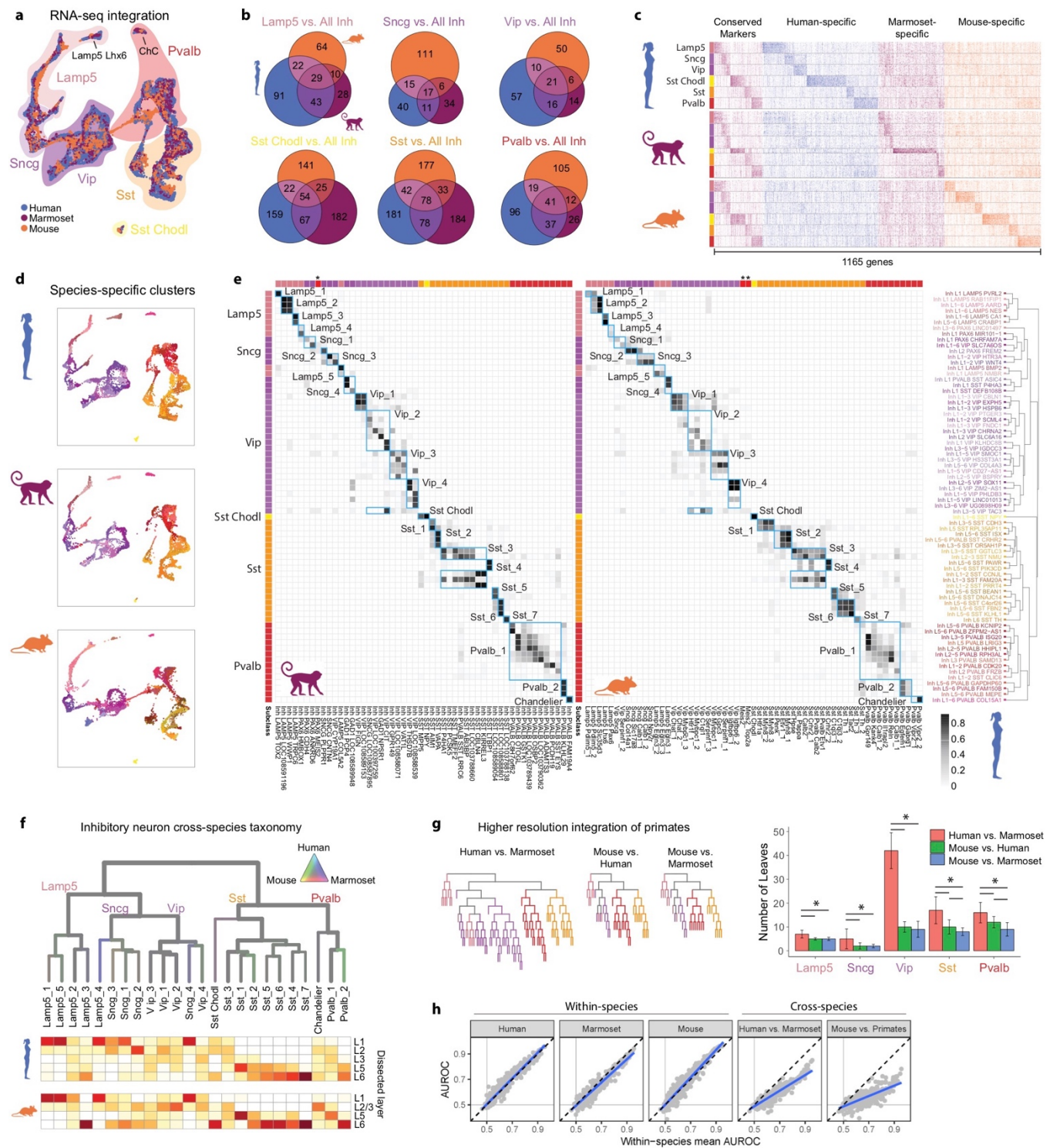
909



911 **Figure 1. Molecular taxonomy of cell types in M1 of human, marmoset, and mouse. a**, M1  
912 highlighted in lateral views of neocortex across species. Nissl-stained sections of M1 annotated with  
913 layers and showing the relative expansion of cortical thickness, particularly L2 and L3 in primates, and  
914 large pyramidal neurons or ‘Betz’ cells in human L5 (arrowhead). Scale bars, 100  $\mu$ m. **b**, Phylogeny of  
915 species and number of nuclei included in analysis for each molecular assay. All assays used nuclei  
916 isolated from the same donors for human and marmoset. SSv4, SMART-Seq v4; Cv3, Chromium v3;  
917 mya, millions of years ago. **c-e**, Dendrograms of cell types defined by RNA-seq (Cv3) for human (**c**),  
918 marmoset (**d**), and mouse (**e**) and annotated with cluster frequency and dissected layer (human only).  
919 Epigenomic clusters (in rows) aligned to RNA-seq clusters as indicated by horizontal black bars.  
920 Asterisks denote RNA clusters that lack corresponding epigenomic clusters. **f**, Relative proportions of  
921 cells in several classes and subclasses were significantly different between species based on an  
922 ANOVA followed by Tukey’s HSD tests (asterisk, adjusted  $P < 0.05$ ).

923

924



925

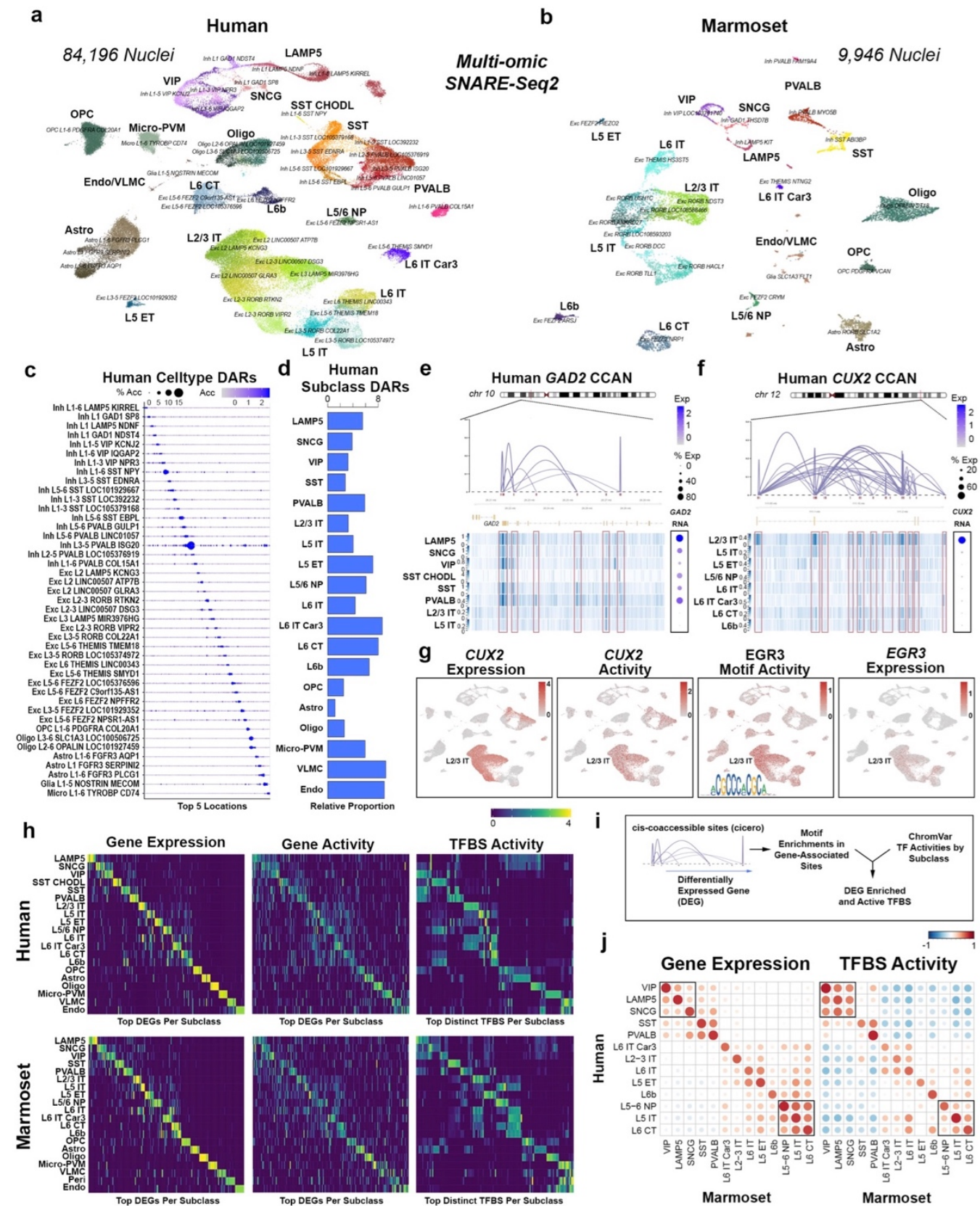
926 **Figure 2. Evolution of GABAergic neuron types across species. a**, UMAP projection of integrated

927 snRNA-seq data from human, marmoset, and mouse GABAergic neurons. Filled outlines indicate cell

928 subclasses. **b**, Venn diagrams indicating the number of shared DEGs across species by subclass.

929 DEGs were determined by ROC tests of each subclass versus all other GABAergic subclasses within a

930 species. **c**, Heatmap of all DEGs from **b** ordered by subclass and species enrichment. Heatmap shows  
931 gene expression scaled by column for up to 50 randomly sampled nuclei from each subclass for each  
932 species. **d**, UMAP projection from **a**, separated by species, and colored by within-species clusters. **e**,  
933 Cluster overlap heatmap showing the proportion of nuclei in each pair of species clusters that are  
934 mixed in the cross-species integrated space. Cross-species consensus clusters are indicated by  
935 labeled blue boxes. Human clusters (rows) are ordered by the dendrogram reproduced from **Figure 1c**.  
936 Marmoset (left columns) and mouse (right columns) clusters are ordered to align with human clusters.  
937 Color bars at top and left indicate subclasses of within-species clusters. Asterisks indicate marmoset  
938 and mouse Meis2 subclasses, which were not present in human. **f**, Dendrogram of GABAergic neuron  
939 consensus clusters with edges colored by species mixture (grey, well mixed). Below: Estimated spatial  
940 distributions of clusters based on layer dissections in human (top) and mouse (bottom). **g**,  
941 Dendrograms of pairwise species integrations, colored by subclass. Bar plots quantifying well-mixed  
942 leaf nodes. Significant differences (adjusted  $P < 0.05$ , Tukey's HSD test) between species are indicated  
943 for each subclass. **h**, Scatter plots of MetaNeighbor analysis showing the performance (AUROC) of  
944 gene-sets to classify GABAergic neurons within and between species. Blue lines, linear regression fits;  
945 black lines, mean within species performance; grey lines, performance equivalent to chance.  
946  
947



948

949

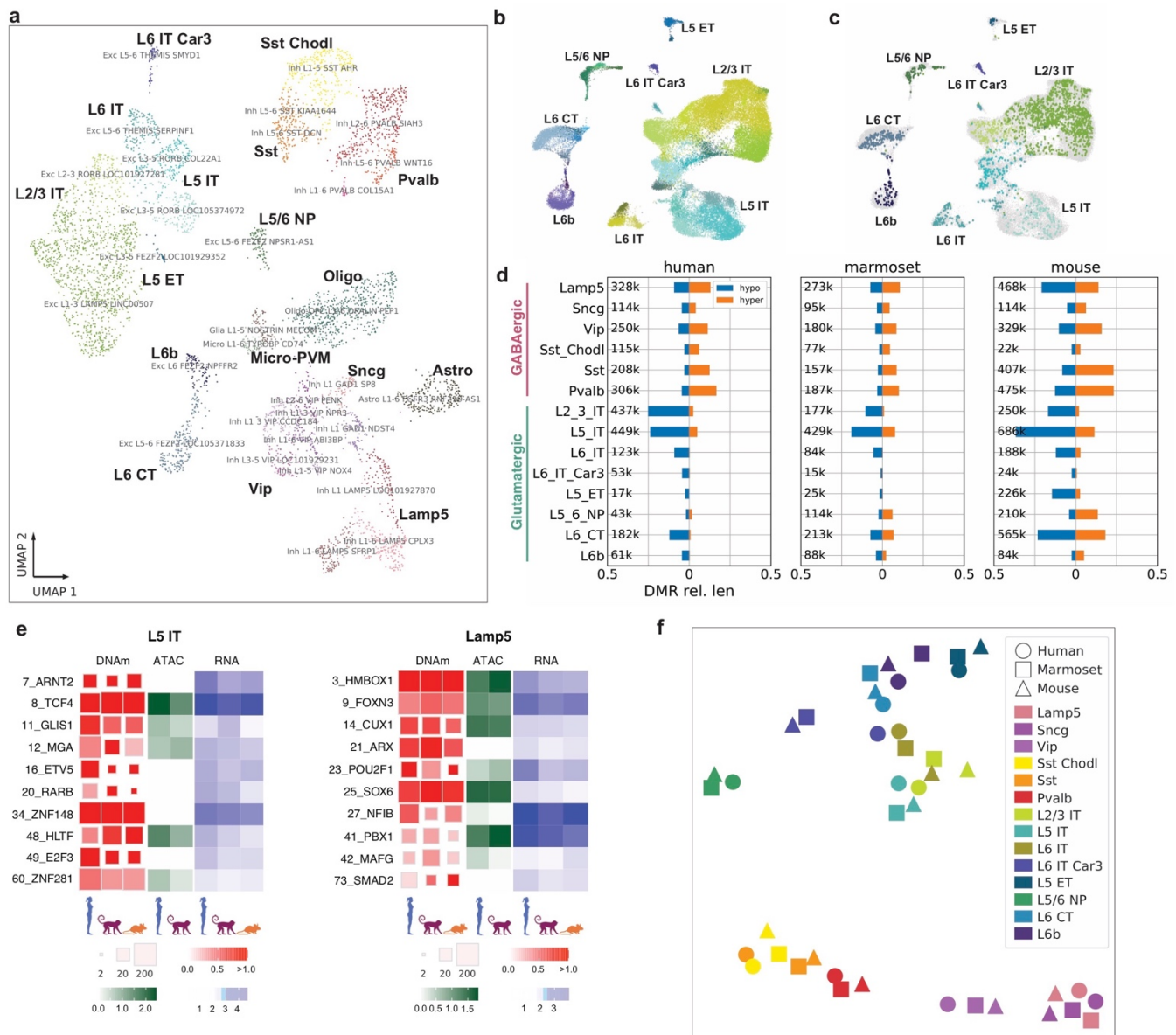
**Figure 3. Dual-omic expression and chromatin accessibility reveals regulatory processes**

950

**defining M1 cell types. a-b UMAP visualizations of human (a) and marmoset (b) M1 SNARE-Seq2**



951 data (2 individuals per species) indicating both subclass and accessibility-level cluster identities. **c**, Dot  
952 plot showing proportion and scaled average accessibility of differentially accessible regions (DARs)  
953 identified between human AC clusters (adjusted  $P < 0.001$ , log-fold change  $> 1$ , top 5 distinct sites per  
954 cluster). **d**, Proportion of total human or marmoset DARs identified between subclasses (adjusted  $P <$   
955  $0.001$ , log-fold change  $> 1$ ) after normalization to cluster sizes. **e-f**, Connection plots for cis-co-  
956 accessible network (CCAN) sites associated with the human *GAD2* (**e**) and *CUX2* (**f**) genes.  
957 Corresponding AC read pile-up tracts for GABAergic and select glutamatergic subclasses are shown.  
958 Right panels are dot plots showing the percentage of expressing nuclei and average gene expression  
959 values (log scale) for *GAD2* or *CUX2* within each of the clusters indicated. **g**, UMAP plots as in Figure  
960 5a (human) showing (scaled from low—gray to high—red) *CUX2* gene expression (RNA) and activity  
961 level predicted from AC data. UMAP plots for activity level of the *EGR3*-binding motif, identified using  
962 chromVAR and found to be enriched within *CUX2* co-accessible sites, and the corresponding  
963 expression (RNA) of the *EGR3* gene are shown. **h**, Heatmaps for human (top) and marmoset (bottom)  
964 showing TFBS enrichments, according to the scheme outlined in (**i**), within genes differentially  
965 expressed between subclasses and having at least two cis-co-accessible sites. Left panels show  
966 scaled average (log scale) gene expression values (RNA) for the top DEGs (adjusted  $P < 0.05$ , log-fold  
967 change  $> 1$ , top 10 distinct sites per cluster visualized), middle panels show the corresponding scaled  
968 average cicero gene activity scores and the right panels show scaled values for the corresponding top  
969 distinct chromVAR TFBS activities (adjusted  $P < 0.05$ , log-fold change  $> 0.5$ , top 10 distinct sites per  
970 cluster visualized). **j**, Correlation plots comparing scaled average gene expression profiles (left panel)  
971 or chromVAR TFBS activity scores (right panel) between human and marmoset matched subclasses.  
972  
973



974

975 **Figure 4. DNA methylation difference across clusters and species. a**, UMAP visualization of

976 human M1 DNAm-seq (snmC-seq2) data indicating both subclass and DNAm cluster identities. **b,c**,

977 UMAP visualization of integration between DNAm-seq and RNA-seq of human glutamatergic neurons

978 colored by cell subclass for all nuclei (**b**) or only nuclei profiled with DNAm-seq (**c**). **d**, Barplots of the

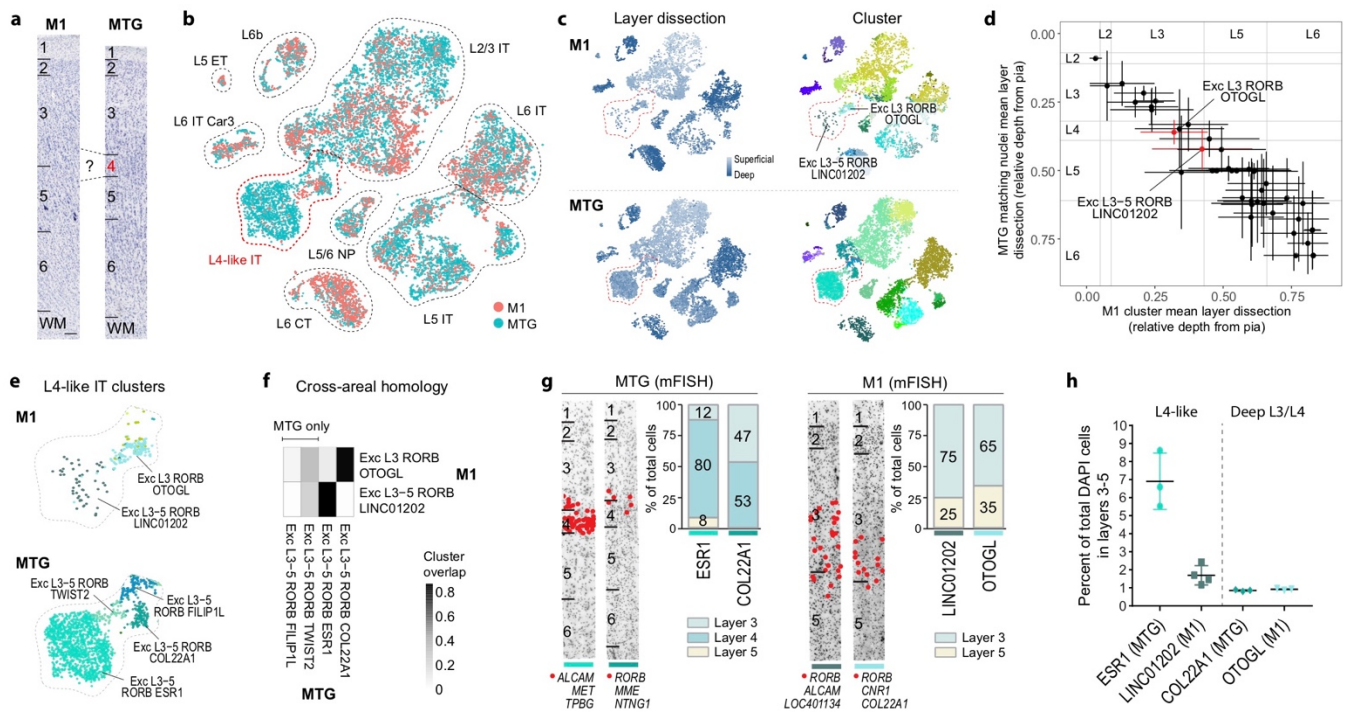
979 relative lengths of hypo- and hyper-methylated DMRs among cell subclasses across three species

980 normalized by cytosine coverage genome-wide (Methods). Total number of DMRs for each subclass

981 are listed (k, thousands). **e**, Distinct TF motif enrichment for L5 IT and *Lamp5* subclasses across

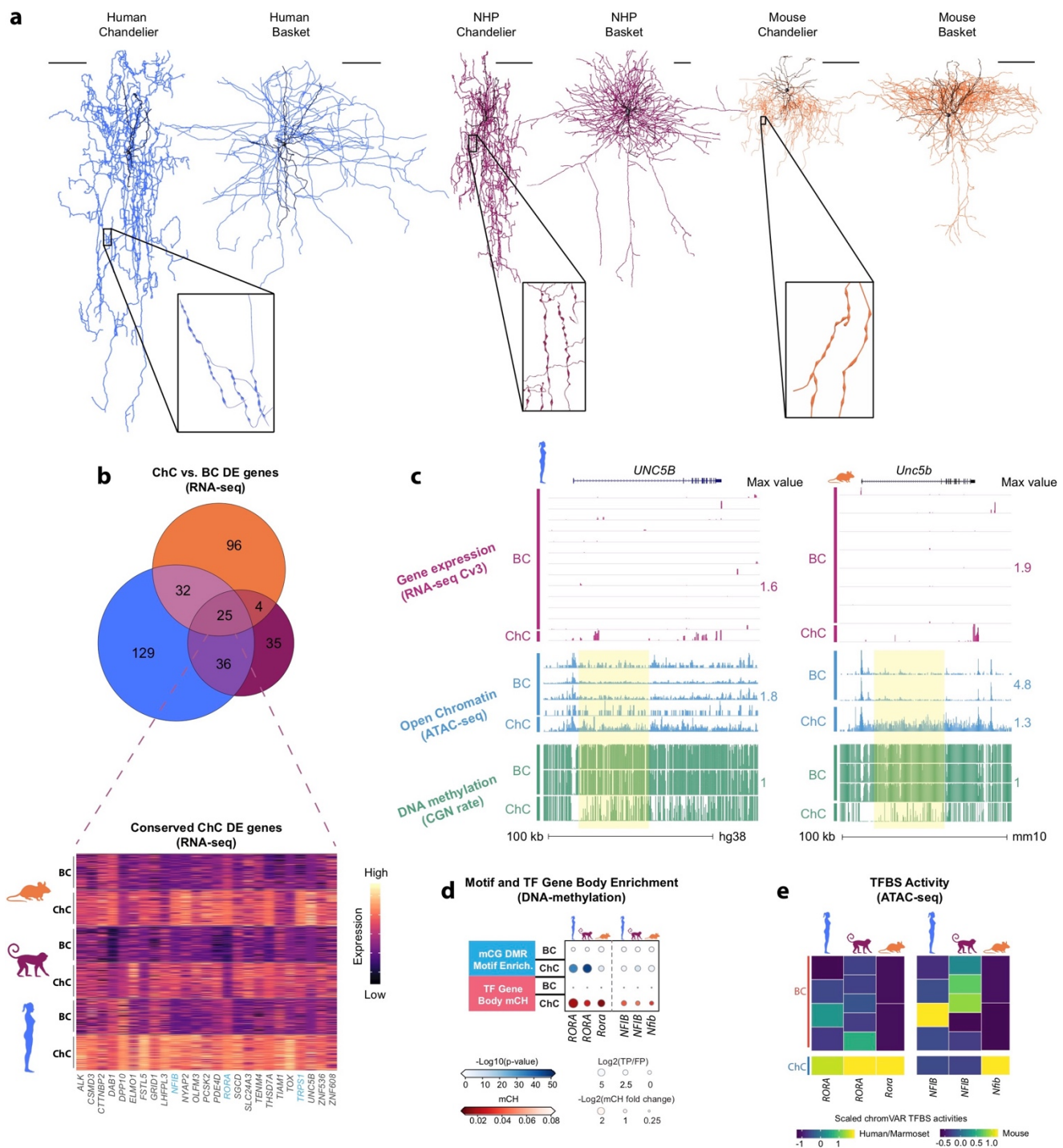
982 species. **f**, t-SNE visualization of subclass TF motif enrichment that is conserved across species.

983



984

985 **Figure 5. L4-like neurons identified in M1 based on cross-area cell type homology.** **a**, t-SNE  
 986 projection of glutamatergic neuronal nuclei from M1 and MTG based on similarity of integrated  
 987 expression levels. Nuclei are intermixed within all cell subclasses. **b**, Nuclei annotated based on the  
 988 relative depth of the dissected layer and within-area cluster. A subset of clusters from superficial layers  
 989 are highlighted. **c**, Proportion of nuclei in each cluster that overlap between areas. MTG clusters  
 990 *COL22A1* and *ESR1* map almost one-to-one with M1 clusters *OTOGL* and *LINC01202*, respectively. **d**,  
 991 Estimated relative depth from pia of M1 glutamatergic clusters and closest layer matching MTG neurons  
 992 based on similarity of integrated expression. Mean (points) and standard deviation (bars) of the  
 993 dissected layer are shown for each cluster and approximate layer boundaries are indicated for M1 and  
 994 MTG. **e**, Magnified view of L4-like clusters in M1 and MTG. Note that MTG clusters *FILIP1L* and  
 995 *TWIST2* have little overlap with any M1 clusters. **f**, Overlap of M1 and MTG clusters in integrated space  
 996 identifies two one-to-one cell type homologies and two MTG-specific clusters. **g**, ISH labeling of MTG  
 997 and M1 clusters quantifies differences in layer distributions for homologous types between cortical  
 998 areas. Cells (red dots) in each cluster were labeled using the markers listed below each representative  
 999 inverted image of a DAPI-stained cortical column. **h**, ISH estimated frequencies of homologous clusters  
 000 shows M1 has a 4-fold sparser L4-like type and similarly rare deep L3 type.



001

002 **Figure 6. Chandelier neurons have conserved molecular features that may contribute to similar**

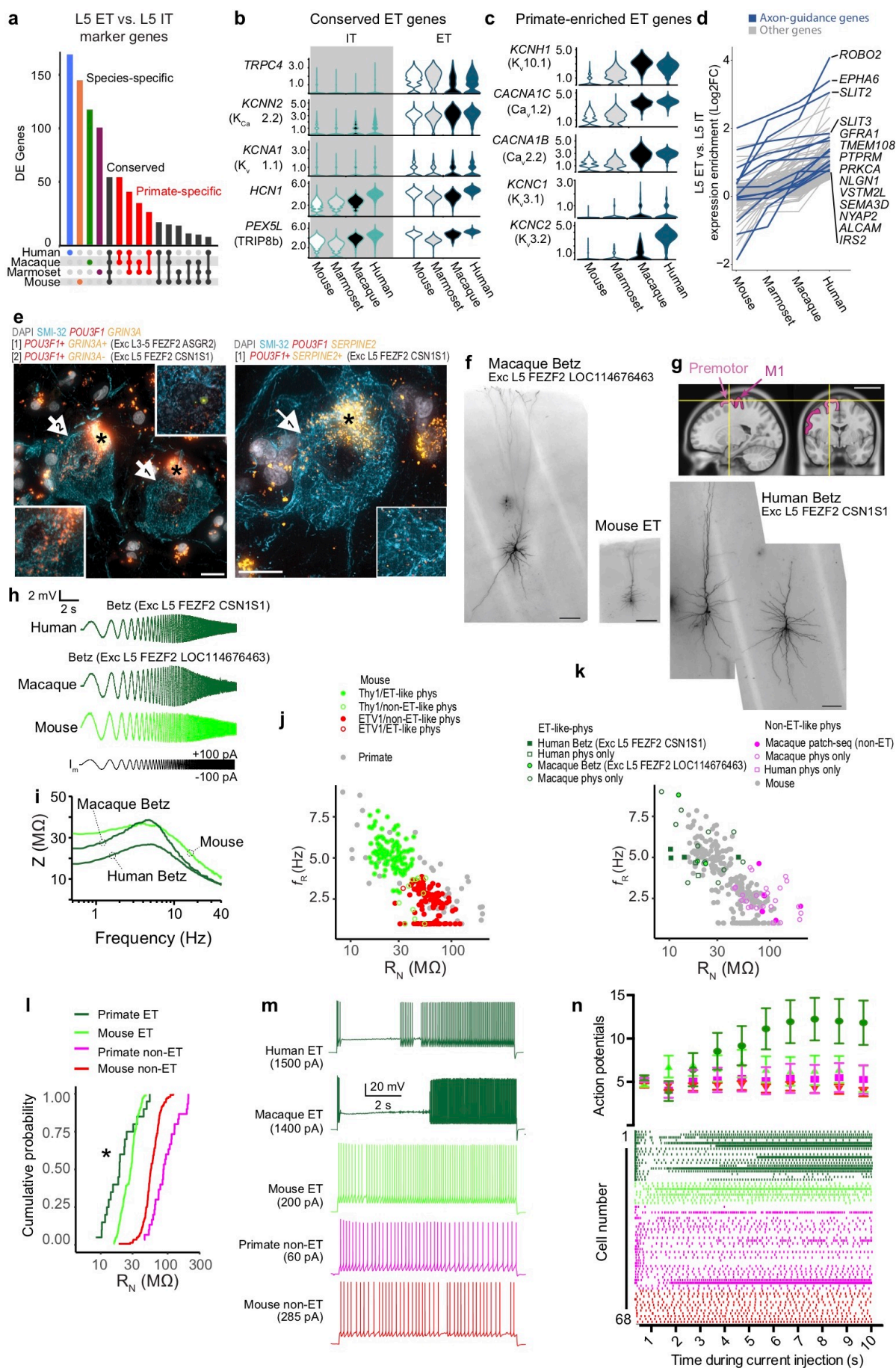
003 **morphology across species. a,** Representative ultrastructure reconstructions of a ChC and BC from

004 human (left), macaque (middle), and mouse (right). Insets show higher magnification of ChC axon

005 cartridges. Macaque reconstructions were from source data available in Neuromorpho<sup>63,64</sup>.

006 **b,** Venn diagram indicating the number of shared ChC-enriched genes across species (top). DEGs were

007 determined by a ROC test of ChCs against BCs within a species. Heatmap showing scaled expression  
008 of the 25 conserved DEGs in 100 randomly selected ChC and BC nuclei for each species (bottom);  
009 transcription factors are colored in blue. **c**, Genome browser tracks showing *UNC5B* locus in human  
010 (left) and mouse (right) ChCs and BCs. Tracks show aligned transcripts, regions of accessible  
011 chromatin, CGN methylation rate, and CHN methylation rate. Yellow highlights mark examples of ChC-  
012 enriched regions of accessible chromatin with hypo-methylated CGN. **d**, Heatmaps of TF gene body  
013 hypo-methylation (mCH) state (bottom half, red) and genome-wide enrichment of TF motif across mCG  
014 DMRs in ChCs and BCs (top half, blue). **e**, Scaled TFBS activities identified from SNARE-seq2 for  
015 human and marmoset according to the scheme in Figure 4i and from mouse snATAC-seq data, using  
016 genes enriched in ChC versus BC (Supplementary Table 19). Rows correspond to BC and ChC  
017 clusters identified in snATAC-seq and SNARE-seq2 datasets.  
018



020 **Figure 7. Betz cells have specialized molecular and physiological properties. a**, Upset plot  
021 showing conserved and divergent L5 ET glutamatergic neuron marker genes. DEGs were determined  
022 by performing a ROC test between L5 ET and L5 IT within each species. **b, c**, Violin plots of ion  
023 channel-related gene expression for genes that are enriched in **(b)** ET versus IT neurons and in **(c)**  
024 primate versus mouse ET neurons. Protein names are in parentheses. **d**, Line graph of 131 genes with  
025 expression enrichment in L5 ET versus IT neurons in human ( $>0.5 \log_2$  fold-change) that decreases  
026 with evolutionary distance from human. **e**, Two example photomicrographs of ISH labeled, SMI-32 IF  
027 stained Betz cells in L5 human M1. Cells corresponding to two L5 ET clusters are labeled based on two  
028 sets of marker genes. Insets show higher magnification of ISH in corresponding cells. Asterisks mark  
029 lipofuscin; scale bar, 20  $\mu\text{m}$ . **f, g**, Exemplar biocytin fills obtained from patch-seq experiments in  
030 human, macaque and mouse brain slices. The example human and macaque neurons mapped to a  
031 Betz cell transcriptomic cell type. Scale bars, 200  $\mu\text{m}$ . **g**, MRI image in sagittal and coronal planes and  
032 approximate location of excised premotor cortex tissue (yellow lines) and adjacent M1. **h**, Voltage  
033 responses to a chirp stimulus for the neurons shown in **f** and **g** (left human neuron). **i**, Corresponding  
034 ZAP profiles. All neurons were clustered into putative ET and non-IT neurons based upon their  
035 resonant frequency and input resistance. **j**, For mouse L5 neurons (*Thy1*-YFP line H, n=117; *Etv1*-  
036 EGFP line, n=123; unlabeled, n=21) 99.2 % of neurons in the *Etv1*-EGFP line possessed non-ET-like  
037 physiology, whereas, 91.4% of neurons in the *Thy1*-YFP line H had ET-like physiology. **k**, For primate  
038 L5 neurons (human, n=8, macaque n=42), all transcriptomically-defined Betz cells (human, n=4,  
039 macaque n=3) had ET-like physiology (human n=6, macaque, n=14), whereas all transcriptomically-  
040 defined non-ET neurons (human n=2, macaque n=3) had non-ET like physiology (human n=2,  
041 macaque n=28). **l**, Cumulative probability distribution of L5 neuron input resistance for primate versus  
042 mouse. \*  $p = 0.0064$ , Kolmogorov-Smirnov test between mouse and primate ET neurons. **m**, Example  
043 voltage responses to 10s step current injections for monkey, mouse and human ET and non-ET  
044 neurons. The amplitude of the current injection was adjusted to produce ~5 spikes during the first  
045 second. **n**, Raster plot (below) and average firing rate (above) during 1 s epochs during the 10s DC  
046 current injection. Primate ET neurons (pooled data from human and macaque) displayed a distinctive

047 decrease followed by a pronounced increase in firing rate over the course of the current injection.  
048 Notably, a similar biphasic-firing pattern is observed in macaque corticospinal neurons *in vivo* during  
049 prolonged motor movements<sup>65</sup>, suggesting that the firing pattern of these neurons during behavior is  
050 intimately tied to their intrinsic membrane properties.

051

## 052 Methods

### 053 ***Ethical compliance***

054 Postmortem adult human brain tissue was collected after obtaining permission from decedent next-of-  
055 kin. Postmortem tissue collection was performed in accordance with the provisions of the United States  
056 Uniform Anatomical Gift Act of 2006 described in the California Health and Safety Code section 7150  
057 (effective 1/1/2008) and other applicable state and federal laws and regulations. The Western  
058 Institutional Review Board reviewed tissue collection processes and determined that they did not  
059 constitute human subjects research requiring institutional review board (IRB) review.

060

### 061 ***Postmortem human tissue specimens***

062 Male and female donors 18–68 years of age with no known history of neuropsychiatric or neurological  
063 conditions ('control' cases) were considered for inclusion in the study (Extended Data Table 1). Routine  
064 serological screening for infectious disease (HIV, Hepatitis B, and Hepatitis C) was conducted using  
065 donor blood samples and only donors negative for all three tests were considered for inclusion in the  
066 study. Only specimens with RNA integrity (RIN) values  $\geq 7.0$  were considered for inclusion in the study.

067 Postmortem brain specimens were processed as previously described<sup>2</sup>. Briefly, coronal brain slabs  
068 were cut at 1cm intervals and frozen for storage at  $-80^{\circ}\text{C}$  until the time of further use. Putative hand and  
069 trunk-lower limb regions of the primary motor cortex were identified, removed from slabs of interest, and  
070 subdivided into smaller blocks. One block from each donor was processed for cryosectioning and



071 fluorescent Nissl staining (Neurotrace 500/525, ThermoFisher Scientific). Stained sections were  
072 screened for histological hallmarks of primary motor cortex. After verifying that regions of interest  
073 contained M1, blocks were processed for nucleus isolation as described below.

074

#### 075 ***Human RNA-sequencing, QC and clustering***

076 SMART-seq v4 nucleus isolation and sorting. Vibratome sections were stained with fluorescent Nissl  
077 permitting microdissection of individual cortical layers ([dx.doi.org/10.17504/protocols.io.7aehibe](https://doi.org/10.17504/protocols.io.7aehibe)).  
078 Nucleus isolation was performed as previously described ([dx.doi.org/10.17504/protocols.io.ztqf6mw](https://doi.org/10.17504/protocols.io.ztqf6mw)).  
079 NeuN staining was carried out using mouse anti-NeuN conjugated to PE (FCMAB317PE, EMD  
080 Millipore) at a dilution of 1:500. Control samples were incubated with mouse IgG1k-PE Isotype control  
081 (BD Biosciences, 555749). DAPI (4',6-diamidino-2-phenylindole dihydrochloride, ThermoFisher  
082 Scientific, D1306) was applied to nuclei samples at a concentration of 0.1 µg/ml. Single-nucleus sorting  
083 was carried out on either a BD FACSAria II SORP or BD FACSAria Fusion instrument (BD  
084 Biosciences) using a 130 µm nozzle. A standard gating strategy based on DAPI and NeuN staining was  
085 applied to all samples as previously described<sup>2</sup>. Doublet discrimination gates were used to exclude  
086 nuclei aggregates.

087

088 SMART-seq v4 RNA-sequencing. The SMART-Seq v4 Ultra Low Input RNA Kit for Sequencing (Takara  
089 #634894) was used per the manufacturer's instructions. Standard controls were processed with each  
090 batch of experimental samples as previously described. After reverse transcription, cDNA was amplified  
091 with 21 PCR cycles. The NexteraXT DNA Library Preparation (Illumina FC-131-1096) kit with  
092 NexteraXT Index Kit V2 Sets A-D (FC-131-2001, 2002, 2003, or 2004) was used for sequencing library  
093 preparation. Libraries were sequenced on an Illumina HiSeq 2500 instrument using Illumina High  
094 Output V4 chemistry.

095

096 SMART-seq v4 gene expression quantification. Raw read (fastq) files were aligned to the GRCh38  
097 human genome sequence (Genome Reference Consortium, 2011) with the RefSeq transcriptome

098 version GRCh38.p2 (current as of 4/13/2015) and updated by removing duplicate Entrez gene entries  
099 from the gtf reference file for STAR processing. For alignment, Illumina sequencing adapters were  
100 clipped from the reads using the fastqMCF program. After clipping, the paired-end reads were mapped  
101 using Spliced Transcripts Alignment to a Reference (STAR) using default settings. Reads that did not  
102 map to the genome were then aligned to synthetic construct (i.e. ERCC) sequences and the *E. coli*  
103 genome (version ASM584v2). Quantification was performed using summarizeOverlaps from the R  
104 package GenomicAlignments. Expression levels were calculated as counts per million (CPM) of exonic  
105 plus intronic reads.

106

107 10x Chromium RNA-sequencing. Nucleus isolation for 10x Chromium RNA-sequencing was conducted  
108 as described ([dx.doi.org/10.17504/protocols.io.y6rfzd6](https://doi.org/10.17504/protocols.io.y6rfzd6)). After sorting, single-nucleus suspensions were  
109 frozen in a solution of 1X PBS, 1% BSA, 10% DMSO, and 0.5% RNAsin Plus RNase inhibitor  
110 (Promega, N2611) and stored at -80°C. At the time of use, frozen nuclei were thawed at 37°C and  
111 processed for loading on the 10x Chromium instrument as described  
112 ([dx.doi.org/10.17504/protocols.io.nx3dfqn](https://doi.org/10.17504/protocols.io.nx3dfqn)). Samples were processed using the 10x Chromium Single-  
113 Cell 3' Reagent Kit v3. 10x chip loading and sample processing was done according to the  
114 manufacturer's protocol. Gene expression was quantified using the default 10x Cell Ranger v3 pipeline  
115 except substituting the curated genome annotation used for SMART-seq v4 quantification. Introns were  
116 annotated as "mRNA", and intronic reads were included in expression quantification.

117

118 Quality control of RNA-seq data. Nuclei were included for analysis if they passed all QC criteria.

119 SMART-seq v4 criteria:

- 120 > 30% cDNA longer than 400 base pairs
- 121 > 500,000 reads aligned to exonic or intronic sequence
- 122 > 40% of total reads aligned
- 123 > 50% unique reads
- 124 > 0.7 TA nucleotide ratio

125 Cv3 criteria:

126 > 500 (non-neuronal nuclei) or > 1000 (neuronal nuclei) genes detected

127 < 0.3 doublet score

128

129 Clustering RNA-seq data. Nuclei passing QC criteria were grouped into transcriptomic cell types using

130 a previously reported iterative clustering procedure (Tasic et al. 2018; Hodge, Bakken et al., 2019).

131 Briefly, intronic and exonic read counts were summed, and  $\log_2$ -transformed expression was centered

132 and scaled across nuclei. X- and Y-chromosomes and mitochondrial genes were excluded to avoid

133 nuclei clustering based on sex or nuclei quality. DEGs were selected, principal components analysis

134 (PCA) reduced dimensionality, and a nearest neighbor graph was built using up to 20 principal

135 components. Clusters were identified with Louvain community detection (or Ward's hierarchical

136 clustering if  $N < 3000$  nuclei), and pairs of clusters were merged if either cluster lacked marker genes.

137 Clustering was applied iteratively to each subcluster until clusters could not be further split.

138

139 Cluster robustness was assessed by repeating iterative clustering 100 times for random subsets of

140 80% of nuclei. A co-clustering matrix was generated that represented the proportion of clustering

141 iterations that each pair of nuclei were assigned to the same cluster. We defined consensus clusters by

142 iteratively splitting the co-clustering matrix as described (Tasic et al. 2018; Hodge, Bakken et al., 2019).

143 The clustering pipeline is implemented in the R package “scrattch.hicat”, and the clustering method is

144 provided by the “run\_consensus\_clust” function (<https://github.com/AllenInstitute/scrattch.hicat>).

145

146 Clusters were curated based on QC criteria or cell class marker expression (*GAD1*, *SLC17A7*,

147 *SNAP25*). Clusters were identified as donor-specific if they included fewer nuclei sampled from donors

148 than expected by chance. To confirm exclusion, clusters automatically flagged as outliers or donor-

149 specific were manually inspected for expression of broad cell class marker genes, mitochondrial genes

150 related to quality, and known activity-dependent genes.

151

152 ***Marmoset sample processing and nuclei isolation***

153 Marmoset experiments were approved by and in accordance with Massachusetts Institute of  
154 Technology IACUC protocol number 051705020. Two adult marmosets (2.3 and 3.1 years old; one  
155 male, one female; Extended Data Table 2) were deeply sedated by intramuscular injection of ketamine  
156 (20-40 mg/kg) or alfaxalone (5-10 mg/kg), followed by intravenous injection of sodium pentobarbital  
157 (10–30 mg/kg). When pedal withdrawal reflex was eliminated and/or respiratory rate was diminished,  
158 animals were transcardially perfused with ice-cold sucrose-HEPES buffer. Whole brains were rapidly  
159 extracted into fresh buffer on ice. Sixteen 2-mm coronal blocking cuts were rapidly made using a  
160 custom-designed marmoset brain matrix. Coronal slabs were snap-frozen in liquid nitrogen and stored  
161 at -80°C until use.

162

163 As with human samples, M1 was isolated from thawed slabs using fluorescent Nissl staining  
164 (Neurotrace 500/525, ThermoFisher Scientific). Stained sections were screened for histological  
165 hallmarks of primary motor cortex. Nuclei were isolated from the dissected regions following this  
166 protocol: <https://www.protocols.io/view/extraction-of-nuclei-from-brain-tissue-2srged6> and processed  
167 using the 10x Chromium Single-Cell 3' Reagent Kit v3. 10x chip loading and sample processing was  
168 done according to the manufacturer's protocol.

169

170 ***Marmoset RNA-sequencing, QC and clustering***

171 RNA-sequencing. Libraries were sequenced on NovaSeq S2 instruments (Illumina). Raw sequencing  
172 reads were aligned to calJac3. Mitochondrial sequence was added into the published reference  
173 assembly. Human sequences of RNR1 and RNR2 (mitochondrial) and RNA5S (ribosomal), were  
174 aligned using gmap to the marmoset genome and added to the calJac3 annotation. Reads that mapped  
175 to exons or introns of each assembly were assigned to annotated genes. Libraries were sequenced to a  
176 median read depth of 5.95 reads per unique molecular index (UMI). The alignment pipeline can be  
177 found at <https://github.com/broadinstitute/Drop-seq>.

178

179 Cell filtering. Cell barcodes were filtered to distinguish true nuclei barcodes from empty beads and PCR  
180 artifacts by assessing proportions of ribosomal and mitochondrial reads, ratio of intronic/exonic reads (>  
181 50% of intronic reads), library size (> 1000 UMIs) and sequencing efficiency (true cell barcodes have  
182 higher reads/UMI). The resulting digital gene expression matrix (DGE) from each library was carried  
183 forward for clustering.

184

185 Clustering. Clustering analysis proceeded as in Krienen et al (2019, bioRxiv). Briefly, independent  
186 component analysis. (ICA, using the fastICA package in R) was performed jointly on all marmoset  
187 DGEs after normalization and variable gene selection as in (Saunders et al 2018, *Cell*). The first-round  
188 clustering resulted in 15 clusters corresponding to major cell classes (neurons, glia, endothelial). Each  
189 cluster was curated as in (Saunders et al 2018, *Cell*) to remove doublets and outliers. Independent  
190 components (ICs) were partitioned into those reflecting artifactual signals (e.g. those for which cell  
191 loading indicated replicate or batch effects). Remaining ICs were used to determine clustering (Louvain  
192 community detection algorithm igraph package in R); for each cluster nearest neighbor and resolution  
193 parameters were set to optimize 1:1 mapping between each IC and a cluster.

194

### 195 ***Mouse snRNA-seq data generation and analysis***

196 Single-nuclei were isolated from mouse primary motor cortex, gene expression was quantified using  
197 Cv3 and SSv4 RNA-sequencing, and transcriptomic cell types and dendrogram were defined as  
198 described in a companion paper <sup>6</sup>.

199

### 200 ***Integrating and clustering human Cv3 and SSv4 snRNA-seq datasets***

201 To establish a set of human consensus cell types, we performed a separate integration of snRNA-seq  
202 technologies on the major cell classes (Glutamatergic, GABAergic, and Non-neuronal). Broadly, this  
203 integration is comprised of 6 steps: (1) subsetting the major cell class from each technology (e.g. Cv3  
204 GABAergic and SSv4 GABAergic); (2) finding marker genes for all clusters within each technology; (3)  
205 integrating both datasets with Seurat's standard workflow using marker genes to guide integration

206 (Seurat 3.1.1); (4) overclustering the data to a greater number of clusters than were originally identified  
207 within a given individual dataset; (5) finding marker genes for all integrated clusters; and (6) merging  
208 similar integrated clusters together based on marker genes until all merging criteria were sufficed,  
209 resulting in the final human consensus taxonomy.

210

211 More specifically, each expression matrix was  $\log_2(\text{CPM} + 1)$  transformed then placed into a Seurat  
212 object with accompanying metadata. Variable genes were determined by downsampling each  
213 expression matrix to a maximum of 300 nuclei per scrattch.hicat-defined cluster (from a previous step;  
214 see scrattch.hicat clustering) and running `select_markers` (scrattch.io 0.1.0) with `n` set to 20, to  
215 generate a list of up to 20 marker genes per cluster. The union of the Cv3 and SSv4 gene lists were  
216 then used as input for anchor finding, dimensionality reduction, and Louvain clustering of the full  
217 expression matrices. We used 100 dimensions for steps in the workflow, and 100 random starts during  
218 clustering. Louvain clustering was performed to overcluster the dataset to identify more integrated  
219 clusters than the number of scrattch.hicat-defined clusters. For example, GABAergic neurons had 79  
220 and 37 scrattch.hicat-defined clusters, 225 overclustered integrated clusters, and 72 final human  
221 consensus clusters after merging for Cv3 and SSv4 datasets, respectively. To merge the overclustered  
222 integrated clusters, up to 20 marker genes were found for each cluster to establish the neighborhoods  
223 of the integrated dataset. Clusters were then merged with their nearest neighbor if there were not a  
224 minimum of ten Cv3 and two SSv4 nuclei in a cluster, and a minimum of 4 DEGs that distinguished the  
225 query cluster from the nearest neighbor (note: these were the same parameters used to perform the  
226 initial scrattch.hicat clustering of each dataset).

227

### 228 ***Integrating and clustering MTG and M1 SSv4 snRNA-seq datasets***

229 To compare cell types between our M1 human cell type taxonomy and our previously described human  
230 MTG taxonomy <sup>2</sup>, we used Seurat's standard integration workflow to perform a supervised integration  
231 of the M1 and MTG SSv4 datasets. Intronic and exonic reads were summed into a single expression  
232 matrix for each dataset, CPM normalized, and placed into a Seurat object with accompanying

233 metadata. All nuclei from each major cell class were integrated and clustered separately. Up to 100  
234 marker genes for each cluster within each dataset were identified, and the union of these two gene lists  
235 was used as input to guide alignment of the two datasets during integration, dimensionality reduction,  
236 and clustering steps. We used 100 dimensions for all steps in the workflow.

237

### 238 ***Integrating Cv3 snRNA-seq datasets across species***

239 To identify homologous cell types across species, we used Seurat's SCTransform workflow to perform  
240 a separate supervised integration on each cell class across species. Raw expression matrices were  
241 reduced to only include genes with one-to-one orthologs defined in the three species (14,870 genes;  
242 downloaded from NCBI Homologene in November, 2019) and placed into Seurat objects with  
243 accompanying metadata. To avoid having one species dominate the integrated space and to account  
244 for potential differences in each species' clustering resolution, we downsampled the number of nuclei to  
245 have similar numbers across species at the subclass level (e.g. *Lamp5*, *Sst*, L2/3 IT, L6b, etc.). The  
246 species with the largest number of clusters under a given subclass was allowed a maximum of 200  
247 nuclei per cluster. The remaining species then split this theoretical maximum (200 nuclei times the max  
248 number of clusters under subclass) evenly across their clusters. For example, the L2/3 IT subclass had  
249 8, 4, and 3 clusters for human, marmoset, and mouse, respectively. All species were allowed a  
250 maximum of 1600 L2/3 IT nuclei total; or a maximum of 200 human, 400 marmoset, and 533 mouse  
251 nuclei per cluster. To integrate across species, all Seurat objects were merged and normalized using  
252 Seurat's SCTransform function. To better guide the alignment of cell types from each species, we found  
253 up to 100 marker genes for each cluster within a given species. We used the union of these gene lists  
254 as input for integration and dimensionality reduction steps, with 30 dimensions used for integration and  
255 100 for dimensionality reduction and clustering. Clustering the human-marmoset-mouse integrated  
256 space provided an additional quality control mechanism, revealing numerous small, species-specific  
257 integrated clusters that contained only low-quality nuclei (low UMIs and genes detected). We excluded  
258 4836 nuclei from the marmoset dataset that constituted low-quality integrated neuronal clusters.

259

260 To identify which clusters in our three species taxonomy aligned with macaque clusters from our L5  
261 dissected Cv3 dataset, we performed an identical integration workflow on Glutamatergic neurons as  
262 was used for the three species integration. Macaque clusters were assigned subclass labels based on  
263 their corresponding alignment with subclasses from the other species. The annotated L5 dissected  
264 macaque Cv3 dataset was then used as a reference for mapping macaque patch-seq nuclei (see  
265 section below).

266

### 267 ***Estimation of cell type homology***

268 To identify homologous groups from different species, we applied a tree-based method  
269 ([https://github.com/AllenInstitute/BICCN\\_M1\\_Evo](https://github.com/AllenInstitute/BICCN_M1_Evo) and package:  
270 <https://github.com/huqiwen0313/speciesTree>). In brief, the approach consists of 4 steps: 1) metacell  
271 clustering, 2) hierarchical reconstruction of a metacell tree, 3) measurements of species mixing and  
272 stability of splits and 4) dynamic pruning of the hierarchical tree.

273

274 Firstly, to reduce noise in single-cell datasets and to remove species-specific batch effects, we  
275 clustered cells into small highly similar groups based on the integrated matrix generated by Seurat, as  
276 described in the previous section. These cells were further aggregated into metacells and the  
277 expression values of the metacells were calculated by averaging the gene expression of individual cells  
278 that belong to each metacell. Correlation was calculated based on the metacell gene expression matrix  
279 to infer the similarity of each metacell cluster. Then hierarchical clustering was performed based on the  
280 metacell gene expression matrix using Ward's method. For each node or corresponding branch in the  
281 hierarchical tree, we calculated 3 measurements, and the hierarchical tree was visualized based on  
282 these measurements: 1) Cluster size visualized as the thickness of branches in the tree; 2) Species  
283 mixing calculated based on entropy of the normalized cell distribution and visualized as the color of  
284 each node and branch; 3) Stability of each node. The entropy of cells was calculated as:  $H =$   
285  $-\sum_i p_i \log p_i$ , where  $p_i$  is the probability of cells from one species appearing among all the cells in a  
286 node. We assessed the node stability by evaluating the agreement between the original hierarchical



287 tree and a result on a subsampled dataset calculated based on the optimal subtree in the subsampled  
288 hierarchical trees derived from subsampling 95% of cells in the original dataset. The entire subsampling  
289 process was repeated 100 times and the mean stability score for every node in the original tree was  
290 calculated. Finally, we recursively searched each node in the tree. If the heuristic criteria (see below)  
291 were not met for any node below the upper node, the entire subtree below the upper node was pruned  
292 and all the cells belonging to this subtree were merged into one homologous group.

293 To identify robust homologous groups, we applied criteria in two steps to dynamically search the cross-  
294 species tree. Firstly, for each node in the tree, we computed the mixing of cells from 3 species based  
295 on entropy and set it as a tuning parameter. For each integrated tree, we tuned the entropy parameter  
296 to make sure the tree method generated the highest resolution of homologous clusters without losing  
297 the ability to identify potential species-specific clusters. Nodes with entropy larger than 2.9 (for inhibitory  
298 neurons) or 2.75 (for excitatory neurons) were considered as well-mixed nodes. For example, an  
299 entropy of 2.9 corresponded to a mixture of human, marmoset, and mouse equal to (0.43, 0.37, 0.2) or  
300 (0.38, 0.30, 0.32). We recursively searched all the nodes in the tree until we found the node nearest the  
301 leaves of the tree that was well-mixed among species, and this node was defined as a well-mixed  
302 upper node. Secondly, we further checked the within-species cell composition for the subtrees below  
303 the well-mixed upper node to determine if further splits were needed. For the cells on the subtrees  
304 below the well mixed upper node, we measured the purity of within-species cell composition by  
305 calculating the percentage of cells that fall into a specific sub-group in each individual species. If the  
306 purity for any species was larger than 0.8, we went one step further below the well mixed upper node  
307 so that its children were selected. Any branches below these nodes (or well-mixed upper node if the  
308 within-species cell composition criteria was not met) were pruned and cells from these nodes were  
309 merged into the same homologous groups, then the final integrated tree was generated.

310 As a final curation step, the homologous groups generated by the tree method were merged to be  
311 consistent with within-species clusters. We defined consensus types by comparing the overlap of  
312 within-species clusters between human and marmoset and human and mouse, as previously described

313 <sup>2</sup>. For each pair of human and mouse clusters and human and marmoset clusters, the overlap was  
314 defined as the sum of the minimum proportion of nuclei in each cluster that overlapped within each leaf  
315 of the pruned tree. This approach identified pairs of clusters that consistently co-clustered within one or  
316 more leaves. Cluster overlaps varied from 0 to 1 and were visualized as a heatmap with human M1  
317 clusters in rows and mouse or marmoset M1 clusters in columns. Cell type homologies were identified  
318 as one-to-one, one-to-many, or many-to many so that they were consistent in all three species. For  
319 example, the Vip\_2 consensus type could be resolved into multiple homologous types between human  
320 and marmoset but not human and mouse, and the coarser homology was retained. Consensus type  
321 names were assigned based on the annotations of member clusters from human and mouse and  
322 avoided specific marker gene names due to the variability of marker expression across species.

323

324 To quantify cell type alignment between pairs of species, we pruned the hierarchical tree described  
325 above based on the stability and mixing of two species. We performed this analysis for human-  
326 marmoset, human-mouse, and marmoset-mouse and compared the alignment resolution of each  
327 subclass. The pruning criteria were tuned to fit the two-species comparison and to remove bias, and we  
328 set the same criteria for all comparisons (entropy cutoff 3.0). Specifically, for each subclass and  
329 pairwise species comparison, we calculated the number of leaves in the pruned tree. We repeated this  
330 analysis on the 100 subsampled datasets and calculated the mean and standard deviation of the  
331 number of leaves in the pruned trees. For each subclass, we tested for significant differences in the  
332 average number of leaves across pairs of species using an ANOVA test followed by post-hoc Tukey  
333 HSD tests.

334

### 335 ***Marker determination for cell type clusters by NS-Forest v2.1***

336 NS-Forest v2.1 was used to determine the minimum set of marker genes whose combined expression  
337 identified cells of a given type with maximum classification accuracy (T. Bakken et al. 2017; Aevermann  
338 et al. 2018). (<https://github.com/JCVenterInstitute/NSForest/releases>). Briefly, for each cluster NS-  
339 Forest produces a Random Forest (RF) model using a one vs all binary classification approach. The

340 top ranked genes from RF are then filtered by expression level to retain genes that are expressed in at  
341 least 50% of the cells within the target cluster. The selected genes are then reranked by Binary Score  
342 calculated by first finding median cluster expression values for a given gene and dividing by the target  
343 median cluster expression value. Next, one minus this scaled value is calculated resulting in 0 for the  
344 target cluster and 1 for clusters that have no expression, while negative scaled values are set to 0.  
345 These values are then summed and normalized by dividing by the total number of clusters. In the ideal  
346 case, where all off-target clusters have no expression, the binary score is 1. Finally, for the top 6 binary  
347 genes optimal expression level cutoffs are determined and all permutations of genes are evaluated by  
348 f-beta score, where the beta is weighted to favor precision. This f-beta score indicates the power of  
349 discrimination for a cluster and a given set of marker genes. The gene combination giving the highest f-  
350 beta score is selected as the optimal marker gene combination. Marker gene sets for human, mouse  
351 and marmoset primary motor cortex are listed in Supplementary Tables 4, 5, and 6, respectively, and  
352 were used to construct the semantic cell type definitions provided in Supplementary Table 1.

353

### 354 ***Calculating differentially expressed genes (DEGs)***

355 To identify subclass level DEGs that are conserved and divergent across species, we used the  
356 integrated Seurat objects from the species integration step. Seurat objects for each major cell class  
357 were downsampled to have up to 200 cells per species cell type. Positive DEGs were then found using  
358 Seurat's `FindAllMarkers` function using the ROC test with default parameters. We compared each  
359 subclass within species to all remaining nuclei in that class and used the SCT normalized counts to test  
360 for differential expression. For example, human *Sst* nuclei were compared to all other GABAergic  
361 human neurons using the ROC test. Venn diagrams were generated using the `eulerr` package (6.0.0) to  
362 visualize the relationship of DEGs across species for a given subclass. Heatmaps of DEGs for all  
363 subclasses under a given class were generated by downsampling each subclass to 50 random nuclei  
364 per species. SCT normalized counts were then scaled and visualized with Seurat's `DoHeatmap`  
365 function.

366

367 To identify ChC DEGs that are enriched over BCs, we used the integrated Seurat objects from the  
368 species integration step. The *Pvalb* subclass was subset and species cell types were then designated  
369 as either ChCs or BCs. Positive DEGs were then found using Seurat's `FindAllMarkers` function  
370 using the ROC test to compare ChCs and BCs for each species. Venn diagrams were generated using  
371 the `eulerr` package (6.0.0) to visualize the relationship of ChC-enriched DEGs across species.  
372 Heatmaps of conserved DEGs were generated by downsampling the dataset to have 100 randomly  
373 selected BCs and ChCs from each species. SCT normalized counts were then scaled and visualized  
374 with Seurat's `DoHeatmap` function.

375

376 We used the four species (human, macaque, marmoset, and mouse) integrated Glutamatergic Seurat  
377 object from the species integration step for all L5 ET DEG figures. L5 ET and L5 IT subclasses were  
378 downsampled to 200 randomly selected nuclei per species. A ROC test was then performed using  
379 Seurat's `FindAllMarkers` function between the two subclasses for each species to identify L5 ET-  
380 specific marker genes. We then used the `UpSetR` (1.4.0) package to visualize the intersections of the  
381 marker genes across all four species as an upset plot. To determine genes that decrease in expression  
382 across evolutionary distance in L5 ET neurons, we found the log-fold change between L5 ET and L5 IT  
383 for each species across all genes. We then filtered the gene lists to only include genes that had a trend  
384 of decreasing log-fold change (human > macaque > marmoset > mouse). Lastly, we excluded any gene  
385 that did not have a log-fold change of 0.5 or greater in the human comparison. These 131 genes were  
386 then used as input for GO analysis with the PANTHER Classification System<sup>66</sup> for the biological  
387 process category, with organism set to *Homo sapiens*. All significant GO terms for this gene list were  
388 associated with cell-cell adhesion and axon-guidance, and are colored blue in the line graph of their  
389 expression enrichment.

390

### 391 ***Estimating differential isoform usage between human and mouse***

392 To assess changes of isoform usage between mouse and human, we used SSV4 data with full  
393 transcript coverage and estimated isoform abundance in each cell subclasses. To mitigate low read

394 depth in each cell, we aggregated reads from all cells in each subclass. We estimated the relative  
395 isoform usage in each subclass by calculating its genic proportion (P), defined as the ratio (R) of  
396 isoform expression to the gene expression, where  $R = (P_{\text{human}} - P_{\text{mouse}}) / (P_{\text{human}} + P_{\text{mouse}})$ . For a common  
397 set of transcripts for mouse and human, we used UCSC browser TransMapV5 set of human transcripts  
398 (hg38 assembly, Gencode v31 annotations) mapped to the mouse genome (mm10 assembly)  
399 <http://hgdownload.soe.ucsc.edu/gbdb/mm10/transMap/V5/mm10.ensembl.transMapV5.bigPsl>. We  
400 considered only medium to highly expressed isoforms, which have abundance > 10 TPM (Transcripts  
401 per Million) and  $P > 0.2$  in either mouse or human and gene expression > 10 TPM in both mouse and  
402 human.

403

404 Calculating isoform abundance in each cell subclass:

- 405 1) Aggregated reads from each subclass
- 406 2) Mapped reads to the mouse or human reference genome with STAR 2.7.3a using default  
407 parameters
- 408 3) Transformed genomic coordinates into transcriptomic coordinates using STAR parameter: --  
409 quantMode TranscriptomeSAM
- 410 4) Quantified isoform and gene expression using RSEM 1.3.3 parameters: --bam --seed 12345 --  
411 paired-end --forward-prob 0.5 --single-cell-prior --calc-ci

412

413 Estimating statistical significance:

- 414 1) Calculated the standard deviation of isoform genic proportion ( $P_{\text{human}}$  and  $P_{\text{mouse}}$ ) from the  
415 RSEM's 95% confidence intervals of isoform expression
- 416 2) Calculated the P-value using normal distribution for the ( $P_{\text{human}} - P_{\text{mouse}}$ ) and the summed  
417 (mouse + human) variance
- 418 3) Bonferroni-adjusted P-values by multiplying nominal P-values by the number of medium to  
419 highly expressed isoforms in each subclass

420

421 ***Species cluster dendrograms***

422 DEGs for a given species were identified using Seurat's `FindAllMarkers` function with a Wilcox test  
423 and comparing each cluster to every other cluster under the same subclass, with `logfc.threshold` set to  
424 0.7 and `min.pct` set to 0.5. The union of up to 100 genes per cluster with the highest `avg_logFC` were  
425 used. The average  $\log_2$  expression of the DEGs were then used as input for the `build_dend` function  
426 from `scrattch.hicat` to create the dendrograms. This was performed on both human and marmoset  
427 datasets. For mouse dendrogram methods, see the companion paper <sup>6</sup>.

428

429 ***Multiplex fluorescent in situ hybridization (FISH)***

430 Fresh-frozen human postmortem brain tissues were sectioned at 14-16  $\mu\text{m}$  onto Superfrost Plus glass  
431 slides (Fisher Scientific). Sections were dried for 20 minutes at  $-20^\circ\text{C}$  and then vacuum sealed and  
432 stored at  $-80^\circ\text{C}$  until use. The RNAscope multiplex fluorescent v1 kit was used per the manufacturer's  
433 instructions for fresh-frozen tissue sections (ACD Bio), except that fixation was performed for 60  
434 minutes in 4% paraformaldehyde in 1X PBS at  $4^\circ\text{C}$  and protease treatment was shortened to 5 minutes.  
435 Primary antibodies were applied to tissues after completion of mFISH staining. Primary antibodies used  
436 were mouse anti-GFAP (EMD Millipore, MAB360, 1:250 dilution) and mouse anti-Neurofilament H  
437 (SMI-32, Biolegend, 801701). Secondary antibodies were goat anti-mouse IgG (H+L) Alexa Fluor  
438 conjugates (594, 647). Sections were imaged using a 60X oil immersion lens on a Nikon TiE  
439 fluorescence microscope equipped with NIS-Elements Advanced Research imaging software (version  
440 4.20). For all RNAscope mFISH experiments, positive cells were called by manually counting RNA  
441 spots for each gene. Cells were called positive for a gene if they contained  $\geq 3$  RNA spots for that

442 gene. Lipofuscin autofluorescence was distinguished from RNA spot signal based on the larger size of  
443 lipofuscin granules and broad fluorescence spectrum of lipofuscin.

444

#### 445 ***Gene family conservation***

446 To investigate the conservation and divergence of gene family coexpression between primates and  
447 mouse, MetaNeighbor analysis<sup>30</sup> was performed using gene groups curated by the HUGO Gene  
448 Nomenclature Committee (HGNC) at the European Bioinformatics Institute  
449 (<https://www.genenames.org>; downloaded January 2020) and by the Synaptic Gene Ontology (SynGO)  
450<sup>67</sup> (downloaded February 2020). HGNC annotations were propagated via the provided group hierarchy  
451 to ensure the comprehensiveness of parent annotations. Only groups containing five or more genes  
452 were included in the analysis.

453

454 After splitting data by class, MetaNeighbor was used to compare data at the cluster level using labels  
455 from cross-species integration with Seurat. Cross-species comparisons were performed at two levels of  
456 the phylogeny: 1) between the two primate species, marmoset and human; and 2) between mouse and  
457 primates. In the first case, the data from the two species were each used as the testing and training set  
458 across two folds of cross-validation, reporting the average performance (AUROC) across folds. In the  
459 second case, the primate data were used as an aggregate training set, and performance in mouse was  
460 reported. Results were compared to average within-species performance.

461

#### 462 ***Replicability of clusters***

463 MetaNeighbor was used to provide a measure of neuronal subclass and cluster replicability within and  
464 across species. For this application, we tested all pairs of species (human-marmoset, marmoset-  
465 mouse, human-mouse) as well as testing within each species. After splitting the data by class, highly  
466 variable genes were identified using the `get_variable_genes` function from MetaNeighbor, yielding 928  
467 genes for GABAergic and 763 genes for Glutamatergic neuron classes, respectively. These were used

468 as input for the MetaNeighborUS function, which was run using the fast\_version and one\_vs\_best  
469 parameters set to TRUE. Using the one\_vs\_best parameter means that only the two closest  
470 neighboring clusters are tested for their similarity to the training cluster, with results reported as the  
471 AUROC for the closest neighbor over the second closest. AUROCs are plotted in heatmaps in  
472 Extended Data Figures 2 and 3. Data to reproduce these figures can be found in Supplementary Table  
473 9, and scripts are on GitHub (<http://github.com/gillislab/MetaNeighbor>).

474

### 475 ***Single-cell methylome data (snmC-seq2): Sequencing and quantification***

476 Library preparation and Illumina sequencing. Detailed methods for bisulfite conversion and library  
477 preparation were previously described for snmC-seq2<sup>5,41</sup>. The snmC-seq2 libraries generated from  
478 mouse brain tissues were sequenced using an Illumina Novaseq 6000 instrument with S4 flowcells and  
479 150 bp paired-end mode.

480

481 Mapping and feature count pipeline. We implemented a versatile mapping pipeline ([http://cemba-](http://cemba-data.rtfid.io)  
482 [data.rtfid.io](http://cemba-data.rtfid.io)) for all the single-cell methylome based technologies developed by our group<sup>5,41,68</sup>. The  
483 main steps of this pipeline included: 1) demultiplexing FASTQ files into single-cell; 2) reads level QC; 3)  
484 mapping; 4) BAM file processing and QC; and 5) final molecular profile generation. The details of the  
485 five steps for snmC-seq2 were described previously<sup>41</sup>. We mapped all the reads from the three  
486 corresponding species onto the human hg19 genome, the marmoset ASM275486v1 genome, and the  
487 mouse mm10 genome. After mapping, we calculated the methyl-cytosine counts and total cytosine  
488 counts for two sets of genome regions in each cell: the non-overlapping chromosome 100-kb bins of  
489 each genome, the methylation levels of which were used for clustering analysis, and the gene body  
490 regions, the methylation levels of which were used for cluster annotation and integration with RNA  
491 expression data.

492

### 493 ***snmC-seq2: Quality control and preprocessing***



494 Cell filtering. We filtered the cells based on these main mapping metrics: 1) mCCC rate < 0.03. mCCC  
495 rate reliably estimates the upper bound of bisulfite non-conversion rate<sup>5</sup>; 2) overall mCG rate > 0.5; 3)  
496 overall mCH rate < 0.2; 4) total final reads > 500,000; and 5) bismark mapping rate > 0.5. Other metrics  
497 such as genome coverage, PCR duplicates rate, and index ratio were also generated and evaluated  
498 during filtering. However, after removing outliers with the main metrics 1-5, few additional outliers can  
499 be found.

500

501 Feature filtering. 100kb genomic bin features were filtered by removing bins with mean total cytosine  
502 base calls < 250 or > 3000. Regions overlap with the ENCODE blacklist<sup>69</sup> were also excluded from  
503 further analysis.

504

505 Computation and normalization of the methylation rate. For CG and CH methylation, the computation of  
506 methylation rate from the methyl-cytosine and total cytosine matrices contains two steps: 1) prior  
507 estimation for the beta-binomial distribution and 2) posterior rate calculation and normalization per cell.  
508 Step 1. For each cell we calculated the sample mean,  $m$ , and variance,  $v$ , of the raw mc rate ( $mc / cov$ )  
509 for each sequence context (CG, CH). The shape parameters ( $\alpha, \beta$ ) of the beta distribution were then  
510 estimated using the method of moments:

$$511 \quad \alpha = m(m(1 - m)/v - 1)$$

$$512 \quad \beta = (1 - m)(m(1 - m)/v - 1)$$

513 This approach used different priors for different methylation types for each cell and used weaker prior to  
514 cells with more information (higher raw variance).

515

516 Step 2. We then calculated the posterior:  $\widehat{mc} = \frac{\alpha + mc}{\alpha + \beta + cov}$ . We normalized this rate by the cell's global  
517 mean methylation,  $m = \alpha / (\alpha + \beta)$ . Thus, all the posterior  $\widehat{mc}$  with 0  $cov$  will be constant 1 after  
518 normalization. The resulting normalized  $mc$  rate matrix contains no NA (not available) value, and  
519 features with less  $cov$  tend to have a mean value close to 1.

520

521 Selection of highly variable features. Highly variable methylation features were selected based on a  
522 modified approach using the scanpy package *scanpy.pp.highly\_variable\_genes* function <sup>70</sup>. In brief, the  
523 *scanpy.pp.highly\_variable\_genes* function normalized the dispersion of a gene by scaling with the  
524 mean and standard deviation of the dispersions for genes falling into a given bin for mean expression of  
525 genes. In our modified approach, we reasoned that both the mean methylation level and the mean *cov*  
526 of a feature (100kb bin or gene) could impact *mc* rate dispersion. We grouped features that fall into a  
527 combined bin of mean and *cov*, and then normalized the dispersion within each *mean-cov* group. After  
528 dispersion normalization, we selected the top 3000 features based on normalized dispersion for  
529 clustering analysis.

530

531 Dimension reduction and combination of different mC types. For each selected feature, *mc* rates were  
532 scaled to unit variance, and zero mean. PCA was then performed on the scaled *mc* rate matrix. The  
533 number of significant PCs was selected by inspecting the variance ratio of each PC using the elbow  
534 method. The CH and CG PCs were then concatenated together for further analysis in clustering and  
535 manifold learning.

536

### 537 ***snmC-seq2: Data analysis***

538 Consensus clustering on concatenated PCs. We used a consensus clustering approach based on  
539 multiple Leiden-clustering <sup>71</sup> over K-Nearest Neighbor (KNN) graph to account for the randomness of  
540 the Leiden clustering algorithms. After selecting dominant PCs from PCA in both mCH and mCG  
541 matrix, we concatenated the PCs together to construct a KNN graph using *scanpy.pp.neighbors* with  
542 Euclidean distance. Given fixed resolution parameters, we repeated the Leiden clustering 300 times on  
543 the KNN graph with different random starts and combined these cluster assignments as a new feature  
544 matrix, where each single Leiden result is a feature. We then used the outlier-aware DBSCAN  
545 algorithm from the scikit-learn package to perform consensus clustering over the Leiden feature matrix  
546 using the hamming distance. Different epsilon parameters of DBSCAN are traversed to generate  
547 consensus cluster versions with the number of clusters that range from minimum to the maximum

548 number of clusters observed in the multiple Leiden runs. Each version contained a few outliers that  
549 usually fall into three categories: 1) cells located between two clusters that had gradient differences  
550 instead of clear borders; 2) cells with a low number of reads that potentially lack information in essential  
551 features to determine the specific cluster; and 3) cells with a high number of reads that were potential  
552 doublets. The amount of type 1 and 2 outliers depends on the resolution parameter and is discussed in  
553 the choice of the resolution parameter section. The type 3 outliers were very rare after cell filtering. The  
554 supervised model evaluation then determined the final consensus cluster version.

555

556 Supervised model evaluation on the clustering assignment. For each consensus clustering version, we  
557 performed a Recursive Feature Elimination with Cross-Validation (RFECV)<sup>72</sup> process from the scikit-  
558 learn package to evaluate clustering reproducibility. We first removed the outliers from this process,  
559 and then we held out 10% of the cells as the final testing dataset. For the remaining 90% of the cells,  
560 we used tenfold cross-validation to train a multiclass prediction model using the input PCs as features  
561 and *sklearn.metrics.balanced\_accuracy\_score*<sup>73</sup> as an evaluation score. The multiclass prediction  
562 model is based on *BalancedRandomForestClassifier* from the imblearn package that accounts for  
563 imbalanced classification problems<sup>74</sup>. After training, we used the 10% testing dataset to test the model  
564 performance using the *balanced\_accuracy\_score* score. We kept the best model and corresponding  
565 clustering assignments as the final clustering version. Finally, we used this prediction model to predict  
566 outliers' cluster assignments, we rescued the outlier with prediction probability > 0.3, otherwise labeling  
567 them as outliers.

568

569 Choice of resolution parameter. Choosing the resolution parameter of the Leiden algorithm is critical for  
570 determining the final number of clusters. We selected the resolution parameter by three criteria: 1. The  
571 portion of outliers < 0.05 in the final consensus clustering version. 2. The ultimate prediction model  
572 accuracy > 0.95. 3. The average cell per cluster  $\geq 30$ , which controls the cluster size to reach the

573 minimum coverage required for further epigenome analysis such as DMR calls. All three criteria  
574 prevented the over-splitting of the clusters; thus, we selected the maximum resolution parameter under  
575 meeting the criteria using a grid search.

576

577 Three-level of iterative clustering analysis. We used an iterative approach to cluster the data into three  
578 levels of categories with the consensus clustering procedure described above. In the first level termed  
579 CellClass, clustering analysis is done on all cells. The resulting clusters are then manually merged into  
580 three canonical classes, glutamatergic neurons, GABAergic neurons, and non-neurons, based on  
581 marker genes. The same clustering procedure was then conducted within each CellClass to get  
582 clusters as the MajorType level. Within each MajorType, we got the final clusters as the SubTypes in  
583 the same way.

584

585 Integrating cell clusters identified from snmC-seq2 and from Cv3. We identified gene markers based on  
586 gene body mCH hypo-methylation for each level of clustering of snmC-seq2 data using our in-house  
587 analysis utilities ([https://github.com/lhqing/cemba\\_data](https://github.com/lhqing/cemba_data)), and identified gene markers for cell class from  
588 Cv3 analysis using scanpy<sup>70</sup>. We then used Scanorama<sup>75</sup> to integrate the two modalities.

589

590 Calling CG differentially methylated regions (DMRs). We identified CG DMRs using methylpy  
591 (<https://github.com/yupenghe/methylpy>) as previously described<sup>76</sup>. Briefly, we first called CG  
592 differentially methylated sites and then merged them into blocks if they both showed similar sample-  
593 specific methylation patterns and were within 250bp. Normalized relative lengths of DMRs (Figure 4d)  
594 were calculated by summation of lengths of DMRs and 250bp around divided by numbers of cytosine  
595 covered in sequencing.

596

597 TFBS motif enrichment analysis. For each cell subclass (cluster), we performed TFBS motif enrichment  
598 analysis for its hypo-methylated DMRs against the hypo-methylated DMRs from other cell subclasses  
599 (clusters) using software AME<sup>77</sup>. DMRs and 250bp regions around were used in the analysis.

600

### 601 ***SNARE-Seq2: Sample preparation***

602 Human and marmoset primary motor cortex nuclei were isolated for SNARE-seq2 according to the  
603 following protocol: <https://www.protocols.io/view/nuclei-isolation-for-snare-seq2-8tvhwn6><sup>7,78</sup>.

604 Fluorescence-activated nuclei sorting (FANS) was then performed on a FACSAria Fusion (BD  
605 Biosciences, Franklin Lakes, NJ) gating out debris from FSC and SSC plots and selecting DAPI<sup>+</sup>  
606 singlets (Extended Data Fig. 5a). Samples were kept on ice until sorting was complete and were used  
607 immediately for SNARE-seq2.

608

### 609 ***SNARE-Seq2: Library preparation and sequencing***

610 A detailed step-by-step protocol for SNARE-Seq2 has been outlined in a companion paper<sup>38</sup>. The  
611 resulting AC libraries were sequenced on MiSeq (Illumina) (R1: 75 cycles for the 1<sup>st</sup> end of AC DNA  
612 read, R2: 94 cycles for cell barcodes and UMI read, R3: 8 cycles for i5 read, R4: 75 cycles for the 2<sup>nd</sup>  
613 end of AC DNA read) for library validation, then on NovaSeq6000 (Illumina) using 300 cycles reagent  
614 kit for data generation. RNA libraries were combined at equimolar ratio and sequenced on MiSeq  
615 (Illumina) (Read 1: 70 cycles for the cDNA read, Index 1: 6 cycles for i7 read, Read 2: 94 cycles for cell  
616 barcodes and UMI read) for library validation, then on NovaSeq6000 (Illumina) using 200 cycles  
617 reagent kit for data generation.

618

### 619 ***SNARE-Seq2: Data processing***

620 A detailed step-by-step SNARE-seq2 data processing pipeline has been provided in a companion  
621 paper<sup>38</sup>. For RNA data, this has involved the use of dropEst to extract cell barcodes and STAR  
622 (v2.5.2b) to align tagged reads to the genome (GRCh38 version 3.0.0 for human; GCF 000004665.1  
623 *Callithrix jacchus*-3.2, marmoset). For AC data, this involved snaptools for alignment to the genome

624 (cellranger-atac-GRCh38-1.1.0 for human, GCF 000004665.1 *Callithrix jacchus*-3.2, marmoset) and to  
625 generate snap objects for processing using the R package snapATAC.

626

### 627 ***SNARE-Seq2: Data analysis***

628 RNA quality filtering. For SNARE-Seq2 data, quality filtering of cell barcodes and clustering analysis  
629 were first performed on transcriptomic (RNA) counts and used to inform on subsequent accessible  
630 chromatin quality filtering and analysis. Each cell barcode was tagged by an associated library batch ID  
631 (for example MOP1, MOP2... etc.), RNA read counts associated with dT and n6 adaptor primers were  
632 merged, libraries were combined for each sample within each experiment and empty barcodes  
633 removed using the emptyDrops() function of DropletUtils<sup>79</sup>, mitochondrial transcripts were removed,  
634 doublets were identified using the DoubletDetection software<sup>80</sup> and removed. All samples were  
635 combined across experiments within species and cell barcodes having greater than 200 and less than  
636 7500 genes detected were kept for downstream analyses. To further remove low quality datasets, a  
637 gene UMI ratio filter (gene.vs.molecule.cell.filter) was applied using Pagoda2 ([https://github.com/hms-](https://github.com/hms-dbmi/pagoda2)  
638 [dbmi/pagoda2](https://github.com/hms-dbmi/pagoda2)).

639

640 RNA data clustering. For human SNARE-seq2 RNA data, clustering analysis was first performed using  
641 Pagoda2 where counts were normalized to the total number per nucleus and batch variations were  
642 corrected by scaling expression of each gene to the dataset-wide average. After variance  
643 normalization, the top 6000 over-dispersed genes were used for principal component analysis.  
644 Clustering was performed using an approximate k-nearest neighbor graph (k values between 50 – 500)  
645 based on the top 75 principal components and cluster identities were determined using the infomap  
646 community detection algorithm. Major cell types were identified using a common set of broad cell type  
647 marker genes: *GAD1/GAD2* (GABAergic neurons), *SLC17A7/SATB2* (glutamatergic neurons),  
648 *PDGFRA* (oligodendrocyte progenitor cells), *AQP4* (astrocytes), *PLP1/MOBP* (oligodendrocytes),  
649 *MRC1* (perivascular macrophages), *PTPRC* (T cells), *PDGFRB* (vascular smooth muscle cells), *FLT1*  
650 (vascular endothelial cells), *DCN* (vascular fibroblasts), *APBB1IP* (microglia) (Extended Data Fig. 5c).

651 Low quality clusters that showed very low gene/UMI detection rates, low marker gene detection and/or  
652 mixed cell type marker profiles were removed. Oligodendrocytes were over-represented (54,080 total),  
653 possibly reflecting a deeper subcortical sampling than intended, therefore, to ensure a more balanced  
654 distribution of cell types, we capped the number of oligodendrocytes at 5000 total and repeated the  
655 PAGODA2 clustering as above. To achieve optimal clustering of the different cell types, different k  
656 values were used to identify cluster subpopulations for different cell types (L2/3 glutamatergic neurons,  
657 k = 500; all other glutamatergic neurons, astrocytes, oligodendrocytes, OPCs, k = 100; GABAergic  
658 neurons, vascular cells, microglia/perivascular macrophages, k = 50). To assess the appropriateness of  
659 the chosen k values, clusters were compared against SMARTer clustering of data generated on human  
660 M1 through correlation of cluster-averaged scaled gene expression values using the corrplot package  
661 (<https://github.com/taiyun/corrplot>) (Extended Data Fig. 5d). For cluster visualization, uniform manifold  
662 approximation and projection (UMAP) dimensional reduction was performed in Seurat (version 3.1.0)  
663 using the top 75 principal components identified using Pagoda2. For marmoset, clustering was initially  
664 performed using Seurat, where the top 2000 variable features were selected from the mean variance  
665 plot using the 'vst' method and used for principal component analysis. UMAP embeddings were  
666 generated using the top 75 principal components. To harmonize cellular populations across platforms  
667 and modalities, snRNA-seq within-species cluster identities were then predicted from both human and  
668 marmoset data. We used an iterative nearest centroid classifier algorithm (Methods, 'Mapping of  
669 samples to reference taxonomies') to generate probability scores for each SNARE-seq2 nuclei mapping  
670 to their respective species' snRNA-seq reference cluster (Cv3 for marmoset and SMART-Seqv4 for  
671 human). Comparing the predicted RNA cluster assignment of each nuclei with Pagoda2-identified  
672 clusters showed highly consistent cluster membership using Jaccard similarity index (Extended Data  
673 Fig. 5e), confirming the robustness of these cell identities discovered using different analysis platforms.  
674

675 AC quality filtering and peak calling. Initial analysis of corresponding SNARE-Seq2 chromatin  
676 accessibility data was performed using SnapATAC software (version 2)  
677 (<https://github.com/r3fang/SnapATAC>) (<https://doi.org/10.1101/615179>). Snap objects were generated

678 by combining individual snap files across libraries within each species. Cell barcodes were included for  
679 downstream analyses only if cell barcodes passed RNA quality filtering (above) and showed greater  
680 than 1000 read fragments and 500 UMI. Read fragments were then binned to 5000 bp windows of the  
681 genome and only cell barcodes showing the fraction of binned reads within promoters greater than 10%  
682 (15% for marmoset) and less than 80% were kept for downstream analysis. Peak regions were called  
683 independently for RNA cluster, subclass and class groupings using MACS2 software  
684 (<https://github.com/taoliu/MACS>) using the following options "--nomodel --shift 100 --ext 200 --qval 5e-2  
685 -B --SPMR". Peak regions were combined across peak callings and used to generate a single peak  
686 count matrix (cell barcodes by chromosomal peak locations) using the "createPmat" function of  
687 SnapATAC.  
688  
689 AC data clustering. The peak count matrices were filtered to keep only locations from chromosomes 1-  
690 22, x or y, and processed using Seurat (version 3.1.0) and Signac (version 0.1.4) software <sup>24</sup>  
691 (<https://satijalab.org>). All peaks having at least 100 counts (20 for marmoset) across cells were used for  
692 dimensionality reduction using latent semantic indexing ("RunLSI" function) and visualized by UMAP  
693 using the first 50 dimensions (40 for marmoset).  
694  
695 Calculating gene activity scores. For a gene activity matrix from accessibility data, cis-co-accessible  
696 sites and gene activity scores were calculated using Cicero software (v1.2.0) <sup>39</sup> ([https://cole-trapnell-](https://cole-trapnell-lab.github.io/cicero-release/)  
697 [lab.github.io/cicero-release/](https://cole-trapnell-lab.github.io/cicero-release/)). The binary peak matrix was used as input with expression family variable  
698 set to "binomialff" to make the aggregated input Cicero CDS object using the AC peak-derived UMAP  
699 coordinates and setting 50 cells to aggregate per bin. Co-accessible sites were then identified using the  
700 "run\_cicero" function using default settings and modules of cis-co-accessible sites identified using the  
701 "generate\_ccans" function. Co-accessible sites were annotated to a gene if they fell within a region  
702 spanning 10,000 bp upstream and downstream of the gene's transcription start site (TSS). The Cicero  
703 gene activity matrix was then calculated using the "build\_gene\_activity\_matrix" function using a co-  
704 accessibility cutoff of 0.25 and added to a separate assay of the Seurat object.



705

706 Integrating RNA/AC data modalities. For reconciliation of differing resolutions achievable from RNA and  
707 accessible chromatin (Extended Data Fig. 5f-k), integrative analysis was performed using Seurat.  
708 Transfer anchors were identified between the activity and RNA matrices using the  
709 “FindTransferAnchors” function. For human, transfer anchors were generated using an intersected list  
710 of variable genes identified from Pagoda2 analysis of RNA clusters (top 2000 genes) and marker genes  
711 for clusters identified from SSV4 data (2492 genes having  $\beta$ -scores > 0.4), and canonical correlation  
712 analysis (CCA) for dimension reduction. For marmoset, transfer anchors were generated using an  
713 intersected list of variable genes identified using Seurat (top 2000 genes) and DEGs identified between  
714 marmoset consensus clusters (Cv3 snRNA-seq data,  $P < 0.05$ , top 100 markers per cluster). Imputed  
715 RNA expression values were then calculated using the “TransferData” function from the Cicero gene  
716 activity matrix using normalized RNA expression values for reference and LSI for dimension reduction.  
717 RNA and imputed expression data were merged, a UMAP co-embedding and shared nearest neighbor  
718 (SNN) graph generated using the top 50 principal components (40 for marmoset) and clusters identified  
719 (“FindClusters”) using a resolution of 4. Resulting integrated clusters were compared against  
720 consensus RNA clusters by calculating jaccard similarity scores using `scratch.hicat` software. Cell  
721 populations identified as T-cells from Pagoda2 analysis (human only) and those representing low  
722 quality integrated clusters, showing a mixture of disparate cell types, were removed from these  
723 analyses. RNA clusters were assigned to co-embedded clusters based on the highest jaccard similarity  
724 score and frequency and then merged to generate the best matched co-embedded clusters, taking in  
725 account cell type and subclass to ensure more accurate merging of ambiguous populations. This  
726 enabled AC-level clusters that directly matched the RNA-defined populations (Extended Data Fig. 5k).  
727 For consensus cluster and subclass level predictions (Extended Data Fig. 5g) the Seurat  
728 “TransferData” function was used to transfer RNA consensus cluster or subclass labels to AC data  
729 using the pre-computed transfer anchors and LSI dimensionality reduction.

730

731 Final AC peak and gene activity matrices. A final combined list of peak regions was then generated  
732 using MACS2 as detailed above for all cell populations corresponding to RNA consensus (> 100  
733 nuclei), accessibility-level, subclass (> 50 nuclei) and class level barcode groupings. The corresponding  
734 peak by cell barcode matrix generated by SnapATAC was used to establish a Seurat object as outlined  
735 above, with peak counts, Cicero gene activity scores and RNA expression values for matched cell  
736 barcodes contained within different assay slots.

737

738 Transcription factor motif analyses. Jaspas motifs (JASPAR2020, all vertebrate) were used to generate  
739 a motif matrix and motif object that was added to the Seurat object using Signac (“CreateMotifMatrix”,  
740 “CreateMotifObject”, “AddMotifObject”) and GC content, region lengths and dinucleotide base  
741 frequencies calculated using the “RegionStats” function. Motif enrichments within specific chromosomal  
742 sites were calculated using the FindMotifs function. For motif activity scores, chromVAR  
743 (<https://greenleafab.github.io/chromVAR>) was performed according to default parameters (marmoset)  
744 or using Signac “RunChromVAR” function on the peak count matrix (human). The chromVAR deviation  
745 score matrix was then added to a separate assay slot of the Seurat object and differential activity of  
746 TFBS between different populations were assessed using the “Find[All]Markers” function through  
747 logistic regression and using the number of peak counts as a latent variable.

748

749 Differentially accessible regions (DARs) between cell populations (Fig. 4b) were identified using the  
750 “find\_all\_diff” function (<https://github.com/yanwu2014/chromfunks>) and p-values calculated using a  
751 hypergeometric test. For visualization, the top DARs (q value < 0.001 and log-fold change > 1) were  
752 selected and the top distinct sites visualized by dot plot in Seurat. For motif enrichment analyses, peak  
753 counts associated with the clusters selected for comparison (all subclasses, all AC-level clusters,  
754 *PVALB*-positive for ChC analyses) were used to identify cis-co-accessible site networks or CCANs  
755 using cicero as indicated above. Peak locations were annotated to the nearest gene (10,000 bases  
756 upstream and downstream of the TSS) and only genes identified from SNARE-seq2 RNA data as being  
757 differentially expressed (Seurat, Wilcoxon Rank Sum test) within the clusters of interest (adjusted P <

758 0.05, average log-fold change > 0.5) were used. Genes having more than one co-accessible site were  
759 assessed for motif enrichments within all overlapping sites using the “FindMotifs” function in Signac  
760 (using peaks for all cell barcodes for subclass and AC-level, or only peaks for ChC or L5 ET cells).  
761 Motifs were then trimmed to only those showing significant differential activity (chromVAR) between the  
762 clusters of interest ( $P < 0.05$ ) as assessed using the “FindMarkers” function on the chromVAR assay  
763 slot using Seurat and using the number of total peaks as a latent variable. The top distinct genes  
764 (subclass, AC-level) or all genes (ChC, Betz) used for motif enrichment analysis were visualized for  
765 scaled average RNA expression levels and scaled average cicero gene activities using the ggHeat  
766 plotting function (SWNE package, <https://github.com/yanwu2014/swne>). Top chromVAR TFBS activities  
767 were also visualized using ggHeat.

768

769 Correlation plots. For correlation of RNA expression and associated AC activities for consensus and  
770 AC-level clusters (Extended Data Fig. 6a-b), average scaled expression values were generated and  
771 pairwise correlations performed for marker genes identified from an intersected list of variable genes  
772 identified from Pagoda2 analysis of RNA clusters (top 2000 genes) and marker genes for clusters  
773 identified from SSV4 data (2492 genes having  $\beta$ -scores > 0.4). For correlation across species,  
774 expression values for genes used to integrate human and marmoset GABAergic and glutamatergic  
775 clusters (Cv3 scRNA-seq data), or chromVAR TFBS activity scores for all Jaspar motifs were averaged  
776 by subclass, scaled (trimming values to a minimum of 0 and a maximum of 4) for each species  
777 separately, then correlated and visualized using corrplot.

778

779 Plots and figures. All UMAP, feature, dot, and violin plots were generated using Seurat. Connection  
780 plots were generated using cicero and peak track gradient heatmaps were generated using Gviz<sup>81</sup> from  
781 bedGraph files generated during peak calling using SnapATAC. Correlation plots were generated using  
782 the corrplot package.

783

784 ***Mouse chandelier cell ATAC-Seq: Data acquisition and analysis***

785 Chandelier cells are rare in mouse cortex and were enriched by isolating individual neurons from  
786 transgenically-labelled mouse primary visual cortex (VISp). Many of the transgenic mouse lines have  
787 previously been characterized by single-cell RNA-seq<sup>1</sup>. Single-cell suspensions of cortical neurons  
788 were generated as described previously<sup>1</sup> and subjected to tagmentation (ATAC-seq)<sup>82,83</sup>. Mixed  
789 libraries, containing 60 to 96 samples were sequenced on an Illumina MiSeq. In total, 4,275 single-cells  
790 were collected from 36 driver-reporter combinations in 67 mice. After sequencing, raw FASTQ files  
791 were aligned to the GRCm38 (mm10) mouse genome using Bowtie v1.1.0 as previously described<sup>9</sup>.  
792 Following alignment, duplicate reads were removed using samtools rmdup, which yielded only single  
793 copies of uniquely mapped paired reads in BAM format. Quality control filtering was applied to select  
794 samples with >10,000 uniquely mapped paired-end fragments, >10% of which were longer than 250  
795 base pairs and with >25% of their fragments overlapping high-depth cortical DNase-seq peaks from  
796 ENCODE<sup>84</sup>. The resulting dataset contained a total of 2,799 samples.

797

798 To increase the cell-type resolution of chromatin accessibility profiles beyond that provided by driver  
799 lines, a feature-free method for computation of pairwise distances (Jaccard) was used. Using Jaccard  
800 distances, principal component analysis (PCA) and t-distributed stochastic neighbor embedding (t-SNE)  
801 were performed, followed by Phenograph clustering<sup>85</sup>. This clustering method grouped cells from  
802 class-specific driver lines together, but also segregated them into multiple clusters. Phenograph-defined  
803 neighborhoods were assigned to cell subclasses and clusters by comparison of accessibility near  
804 transcription start site (TSS  $\pm$  20 kb) to median expression values of scRNA-seq clusters at the cell type  
805 and at the subclass level from mouse primary visual cortex<sup>86</sup>. From this analysis, a total of 226  
806 samples were assigned to *Pvalb* and 124 samples to *Pvalb Vipr2* (ChC) clusters. The sequence data  
807 for these samples were grouped together and further processed through the Snap-ATAC pipeline.

808

809 Mouse scATAC-seq peak counts for *Pvalb* and ChC were used to generate a Seurat object as outlined  
810 for human and marmoset SNARE-Seq2 AC data. Cicero cis-co-accessible sites were identified, gene  
811 activity scores calculated, and motif enrichment analyses performed as outlined above. Genes used for

812 motif enrichment were ChC markers identified from differential expression analysis between *PVALB*-  
813 *positive* clusters in mouse Cv3 scRNA-seq data (adjusted  $P < 0.05$ ).

814

### 815 ***Patch-seq neuronal physiology, morphology, and transcriptomics***

816 Subjects. The human neurosurgical specimen was obtained from a 61-year old female patient that  
817 underwent deep tumor resection (glioblastoma) from the frontal lobe at a local hospital (Harborview  
818 Medical Center). The patient provided informed consent and experimental procedures were approved  
819 by the hospital institute review board before commencing the study. Post-hoc analysis revealed that the  
820 neocortical tissue obtained from this patient was from a premotor region near the confluence of the  
821 superior frontal gyrus and the precentral gyrus (Fig. 7g). All procedures involving macaques and mice  
822 were approved by the Institutional Animal Care and Use Committee at either the University of  
823 Washington or the Allen Institute for Brain Science. Macaque M1 tissue was obtained from male (n=4)  
824 and female (n=5) animals (mean age=  $10 \pm 2.21$  years) designated for euthanasia via the Washington  
825 National Primate Research Center's Tissue Distribution Program. Mouse M1 tissue was obtained from  
826 4-12 week old male and female mice from the following transgenic lines: *Thy1h-eyfp* (B6.Cg-Tg(*Thy1*-  
827 YFP)-HJrs/J: JAX Stock No. 003782), *Etv1-egfp* Tg(*Etv1*-EGFP)BZ192Gsat/Mmucd (*etv1*) mice  
828 maintained with the outbred Charles River Swiss Webster background (CrI:CFW(SW) CR Stock No.  
829 024), and C57BL/6-Tg(*Pvalb*-tdTomato)15Gfng/J: JAX stock No. 027395.

830

831 Brain slice preparation. Brain slice preparation was similar for *Pvalb*-TdTomato mice, macaque and  
832 human samples. Upon resection, human neurosurgical tissue was immediately placed in a chilled and  
833 oxygenated solution formulated to prevent excitotoxicity and preserve neural function<sup>87</sup>. This artificial  
834 cerebral spinal fluid (NMDG aCSF) consisted of (in mM): 92 with N-methyl-D-glucamine (NMDG), 2.5  
835 KCl, 1.25 NaH<sub>2</sub>PO<sub>4</sub>, 30 NaHCO<sub>3</sub>, 20 4-(2-hydroxyethyl)-1-piperazineethanesulfonic acid (HEPES), 25  
836 glucose, 2 thiourea, 5 Na-ascorbate, 3 Na-pyruvate, 0.5 CaCl<sub>2</sub>·4H<sub>2</sub>O and 10 MgSO<sub>4</sub>·7H<sub>2</sub>O. The pH of  
837 the NMDG aCSF was titrated to pH 7.3–7.4 with concentrated hydrochloric acid and the osmolality was  
838 300-305 mOsmoles/Kg. The solution was pre-chilled to 2-4°C and thoroughly bubbled with carbogen

839 (95% O<sub>2</sub>/5% CO<sub>2</sub>) prior to collection. Macaques were anesthetized with sevoflurane gas during which  
840 the entire cerebrum was extracted and placed in the same protective solution described above. After  
841 extraction, macaques were euthanized with sodium-pentobarbital. We dissected the trunk/limb area of  
842 the primary motor cortex for brain slice preparation. *Pvalb*-TdTomato mice were deeply anesthetized by  
843 intraperitoneal administration of Advertin (20mg/kg IP) and were perfused through the heart with NMDG  
844 aCSF (bubbled with carbogen).

845

846 Brains were sliced at 300-micron thickness on a vibratome using the NMDG protective recovery  
847 method and a zirconium ceramic blade<sup>61,87</sup>. Mouse brains were sectioned coronally, and human and  
848 macaque brains were sectioned such that the angle of slicing was perpendicular to the pial surface.  
849 After sections were obtained, slices were transferred to a warmed (32-34° C) initial recovery chamber  
850 filled with NMDG aCSF under constant carbogenation. After 12 minutes, slices were transferred to a  
851 chamber containing an aCSF solution consisting of (in mM): 92 NaCl, 2.5 KCl, 1.25 NaH<sub>2</sub>PO<sub>4</sub>, 30  
852 NaHCO<sub>3</sub>, 20 HEPES, 25 glucose, 2 thiourea, 5 Na-ascorbate, 3 Na-pyruvate, 2 CaCl<sub>2</sub>·4H<sub>2</sub>O and 2  
853 MgSO<sub>4</sub>·7H<sub>2</sub>O continuously bubbled with 95% O<sub>2</sub>/5% CO<sub>2</sub>. Slices were held in this chamber for use in  
854 acute recordings or transferred to a 6-well plate for long-term culture and viral transduction. Cultured  
855 slices were placed on membrane inserts and wells were filled with culture medium consisting of 8.4 g/L  
856 MEM Eagle medium, 20% heat-inactivated horse serum, 30 mM HEPES, 13 mM D-glucose, 15 mM  
857 NaHCO<sub>3</sub>, 1 mM ascorbic acid, 2 mM MgSO<sub>4</sub>·7H<sub>2</sub>O, 1 mM CaCl<sub>2</sub>·4H<sub>2</sub>O, 0.5 mM GlutaMAX-I, and 1 mg/L  
858 insulin (Ting et al 2018). The slice culture medium was carefully adjusted to pH 7.2-7.3, osmolality of  
859 300-310 mOsmoles/Kg by addition of pure H<sub>2</sub>O, sterile-filtered and stored at 4°C for up to two weeks.  
860 Culture plates were placed in a humidified 5% CO<sub>2</sub> incubator at 35°C and the slice culture medium was  
861 replaced every 2-3 days until end point analysis. 1-3 hours after brain slices were plated on cell culture  
862 inserts, brain slices were infected by direct application of concentrated AAV viral particles over the slice  
863 surface (Ting et al 2018).

864

865 Thy1 and Etv1 mice were deeply anesthetized by IP administration of ketamine (130 mg/kg) and  
866 xylazine (8.8 mg/kg) mix and were perfused through the heart with chilled (2-4°C) sodium-free aCSF  
867 consisting of (in mM): 210 Sucrose, 7 D-glucose, 25 NaHCO<sub>3</sub>, 2.5 KCl, 1.25 NaH<sub>2</sub>PO<sub>4</sub>, 7 MgCl<sub>2</sub>, 0.5  
868 CaCl<sub>2</sub>, 1.3 Na-ascorbate, 3 Na-pyruvate bubbled with carbogen (95% O<sub>2</sub>/5% CO<sub>2</sub>). Near coronal slices  
869 300 microns thick were generated using a Leica vibratome (VT1200) in the same sodium-free aCSF  
870 and were transferred to warmed (35°C) holding solution (in mM): 125 NaCl, 2.5 KCl, 1.25 NaH<sub>2</sub>PO<sub>4</sub>, 26  
871 NaHCO<sub>3</sub>, 2 CaCl<sub>2</sub>, 2 MgCl<sub>2</sub>, 17 dextrose, and 1.3 sodium pyruvate bubbled with carbogen (95% O<sub>2</sub>/5%  
872 CO<sub>2</sub>). After 30 minutes of recovery, the chamber holding slices was allowed to cool to room  
873 temperature.

874

875 Patch clamp electrophysiology. Macaque, human and *Pvalb*-TdTomato mouse brain slices were placed  
876 in a submerged, heated (32-34°C) recording chamber that was continually perfused (3-4 mL/min) with  
877 aCSF under constant carbogenation and containing (in mM) 1): 119 NaCl, 2.5 KCl, 1.25 NaH<sub>2</sub>PO<sub>4</sub>, 24  
878 NaHCO<sub>3</sub>, 12.5 glucose, 2 CaCl<sub>2</sub>·4H<sub>2</sub>O and 2 MgSO<sub>4</sub>·7H<sub>2</sub>O (pH 7.3-7.4). Slices were viewed with an  
879 Olympus BX51WI microscope and infrared differential interference contrast (IR-DIC) optics and a 40x  
880 water immersion objective. The infragranular layers of macaque primary motor cortex and human  
881 premotor cortex are heavily myelinated, which makes visualization of neurons under IR-DIC virtually  
882 impossible. To overcome this challenge, we labeled neurons using various viral constructs in  
883 organotypic slice cultures (Extended Data Fig. 10g).

884 Patch pipettes (2-6 MΩ) were filled with an internal solution containing (in mM): 110.0 K-gluconate,  
885 10.0 HEPES, 0.2 EGTA, 4 KCl, 0.3 Na<sub>2</sub>-GTP, 10 phosphocreatine disodium salt hydrate, 1 Mg-ATP, 20  
886 μg/ml glycogen, 0.5U/μL RNase inhibitor (Takara, 2313A) and 0.5% biocytin (Sigma B4261), pH 7.3.  
887 Fluorescently labeled neurons from *Thy1* or *Etv1* mice were visualized through a 40x objective using  
888 either Dodt contrast with a CCD camera (Hamamatsu) and/or a 2-photon imaging/ uncaging system  
889 from Prairie (Bruker) Technologies. Recordings were made in aCSF: (in mM): 125 NaCl, 3.0 KCl, 1.25  
890 NaH<sub>2</sub>PO<sub>4</sub>, 26 NaHCO<sub>3</sub>, 2 CaCl<sub>2</sub>, 1 MgCl<sub>2</sub>, 17 dextrose, and 1.3 sodium pyruvate bubbled with  
891 carbogen (95% O<sub>2</sub>/5% CO<sub>2</sub>) at 32-35°, with synaptic inhibition blocked using 100 μM picrotoxin.

892 Sylgard-coated patch pipettes (3-6 M $\Omega$ ) were filled with an internal solution containing (in mM): 135 K-  
893 gluconate, 12 KCl, 11 HEPES, 4 MgATP, 0.3 NaGTP, 7 K<sub>2</sub>-phosphocreatine, 4 Na<sub>2</sub>-phosphocreatine (pH  
894 7.42 with KOH) with neurobiotin (0.1-0.2%), Alexa 594 (40  $\mu$ M) and Oregon Green BAPTA 6F (100  
895  $\mu$ M).

896

897 Whole cell somatic recordings were acquired using either a Multiclamp 700B amplifier, or an AxoClamp  
898 2B amplifier (Molecular Devices) and were digitized using an ITC-18 (HEKA). Data acquisition software  
899 was either MIES (<https://github.com/AllenInstitute/MIES/>) or custom software written in Igor Pro.

900 Electrical signals were digitized at 20-50 kHz and filtered at 2-10 kHz. Upon attaining whole-cell current  
901 clamp mode, the pipette capacitance was compensated and the bridge was balanced. Access  
902 resistance was monitored throughout the recording and was 8-25 M $\Omega$ .

903

904 Data analysis. Data were analyzed using custom analysis software written in Igor Pro. All

905 measurements were made at resting membrane potential. Input resistance ( $R_N$ ) was measured from a  
906 series of 1 s hyperpolarizing steps from -150 pA to +50 pA in +20 pA increments. For neurons with low  
907 input resistance (e.g. the Betz cells) this current injection series was scaled by upwards of 4x. Input

908 resistance ( $R_N$ ) was calculated from the linear portion of the current–steady state voltage relationship

909 generated in response to these current injections. Resonance ( $f_R$ ) was determined from the voltage

910 response to a constant amplitude sinusoidal current injection (Chirp stimulus). The chirp stimulus

911 increased in frequency either linearly from 1-20 Hz over 20 s or logarithmically from 0.2-40 Hz over 20s.

912 The amplitude of the Chirp was adjusted in each cell to produce a peak-to-peak voltage deflection of

913  $\sim$ 10 mV. The impedance amplitude profile (ZAP) was constructed from the ratio of the fast Fourier

914 transform of the voltage response to the fast Fourier transform of the current injection. ZAPs were

915 produced by averaging at least three presentations of the Chirp and were smoothed using a running

916 median smoothing function. The frequency corresponding to the peak impedance ( $Z_{max}$ ) was defined as

917 the resonant frequency. Spike input/output curves were constructed in response to 1 s step current



918 injections (50 pA-500 pA in 50 pA steps). For a subset of experiments, this current injection series was  
919 extended to 3A in 600 pA steps to probe the full dynamic range of low  $R_N$  neurons. Spike frequency  
920 acceleration analysis was performed for current injections producing  $\sim 10$  spikes during the 1 s step.  
921 Acceleration ratio was defined as the ratio of the second to the last interspike interval. To examine the  
922 dynamics of spike timing over longer periods, we also measured spiking in response to 10 s step  
923 current injections in which the amplitude of the current was adjusted to produce  $\sim 5$  spikes in the first  
924 second. Action potential properties were measured for currents near rheobase. Action potential  
925 threshold was defined as the voltage at which the first derivative of the voltage response exceeded 20  
926 V/s. AP width was measured at half the amplitude between threshold and the peak voltage. Fast AHP  
927 was defined relative to threshold. We clustered mouse, macaque and human pyramidal neurons into  
928 two broad groups based on their  $R_N$  and  $f_R$  using Ward's algorithm.

929

### 930 Viral vector production and transduction.

931 Recombinant AAV vectors were produced by triple-transfection of ITR-containing enhancer plasmids  
932 along with AAV helper and rep/cap plasmids using the AAV293 cell line, followed by harvest,  
933 purification and concentration of the viral particles. The AAV293 packaging cell line and plasmid  
934 supplying the helper function are available from a commercial source (Cell Biolabs). The PHP.eB  
935 capsid variant was generated by Dr. Viviana Gradinaru at the California Institute of Technology<sup>88</sup> and  
936 the DNA plasmid for AAV packaging is available from Addgene (plasmid#103005). Quality control of  
937 the packaged AAV was determined by viral titering to determine an adequate concentration was  
938 achieved ( $>5E^{12}$  viral genomes per mL), and by sequencing the AAV genome to confirm the identity of  
939 the viral vector that was packaged. Human and NHP L5 ET neurons including Betz cells were targeted  
940 in cultured slices by transducing the slices with viral vectors that either generically label neurons (AAV-  
941 hSyn1-tdTomato), or that enrich for L5 ET neurons by expressing reporter transgene under the control  
942 of the msCRE4 enhancer<sup>86</sup>.

943

944 Processing of Patch-seq samples. For a subset of experiments, the nucleus was extracted at the end of  
945 the recording and processed for RNA-sequencing. Prior to data collection for these experiments, all  
946 surfaces were thoroughly cleaned with RNase Zap. The contents of the pipette were expelled into a  
947 PCR tube containing lysis buffer (Takara, 634894). cDNA libraries were produced using the SMART-  
948 Seq v4 Ultra Low Input RNA Kit for Sequencing according to the manufacturer's instructions. We  
949 performed reverse transcription and cDNA amplification for X PCR cycles. Sample proceeded through  
950 Nextera NT DNA Library Preparation using Nextera XT Index Kit V2 Set A(FC-131-2001).

951  
952 Mapping of samples to reference taxonomies. To identify which cell type a given patch-seq nuclei  
953 mapped to, we used our previously described nearest centroid classifier <sup>1</sup>. Briefly, a centroid classifier  
954 was constructed for Glutamatergic reference data (human SSv4 or macaque Cv3) using marker genes  
955 for each cluster. Patch-seq nuclei were then mapped to the appropriate species reference 100 times,  
956 using 80% of randomly sampled marker genes during each iteration. Probabilities for each nuclei  
957 mapping to each cluster were computed over the 100 iterations, resulting in a confidence score ranging  
958 from 0 to 100. We identified four human patch-seq nuclei that mapped with > 85% confidence and four  
959 macaque nuclei that mapped with > 93% confidence to a cluster in the L5 ET subclass.

960

## 961 Data availability

962 Raw sequence data are available for download from the Neuroscience Multi-omics Archive  
963 (<https://nemoarchive.org/>) and the Brain Cell Data Center (<https://biccn.org/data>). Visualization and  
964 analysis tools are available at NeMO Analytics (Individual species:  
965 [https://nemoanalytics.org//index.html?layout\\_id=ac9863bf](https://nemoanalytics.org//index.html?layout_id=ac9863bf); Integrated species:  
966 [https://nemoanalytics.org//index.html?layout\\_id=34603c2b](https://nemoanalytics.org//index.html?layout_id=34603c2b)) and Cytosplore Viewer  
967 (<https://viewer.cytosplore.org/>). These tools allow users to compare cross-species datasets and  
968 consensus clusters via genome and cell browsers and calculate differential expression within and  
969 among species. A semantic representation of the cell types defined through these studies is available in

970 the provisional Cell Ontology (<https://bioportal.bioontology.org/ontologies/PCL>; Supplementary Table  
971 1).

972

## 973 Code availability

974 Code to reproduce figures will be available for download from

975 [https://github.com/AllenInstitute/BICCN\\_M1\\_Evo](https://github.com/AllenInstitute/BICCN_M1_Evo).

976

## 977 Acknowledgements

978 We thank the Tissue Procurement, Tissue Processing and Facilities teams at the Allen Institute for  
979 Brain Science for assistance with the transport and processing of postmortem and neurosurgical brain  
980 specimens; the Technology team at the Allen Institute for assistance with data management; M.  
981 Vawter, J. Davis and the San Diego Medical Examiner's Office for assistance with postmortem tissue  
982 donations. We thank Ximena Opitz-Araya and Allen Institute for Brain Science Viral Technology team  
983 for AAV packaging. We thank Lindsay Ng, Dijon Hill and Ram Rajanbabu for patching the human and  
984 mouse cells in the figure describing chandelier neurons and Sara Kebede, Alice Mukora, Grace  
985 Willams for reconstructing them. This work was funded by the Allen Institute for Brain Science and by  
986 US National Institutes of Health grant U01 MH114812-02 to E.S.L. Support for the development of NS-  
987 Forest v.2 and the provisional cell ontology was provided by the Chan–Zuckerberg Initiative DAF, an  
988 advised fund of the Silicon Valley Community Foundation (2018-182730). G.Q. is supported by NSF  
989 CAREER award 1846559. This work was partially supported by an NWO Gravitation project:  
990 BRAINSCAPES: A Roadmap from Neurogenetics to Neurobiology (NWO: 024.004.012) and NWO  
991 TTW project 3DOMICS (NWO: 17126). This project was supported in part by NIH grants  
992 P51OD010425 from the Office of Research Infrastructure Programs (ORIP) and UL1TR000423 from  
993 the National Center for Advancing Translational Sciences (NCATS). Its contents are solely the  
994 responsibility of the authors and do not necessarily represent the official view of NIH, ORIP, NCATS,  
995 the Institute of Translational Health Sciences or the University of Washington National Primate

996 Research Center. This work is supported in part by NIH BRAIN Initiative award RF1MH114126 from the  
997 National Institute of Mental Health to E.S.L., J.T.T., and B.P.L., NIH BRAIN Initiative award  
998 U19MH121282 to J.R.E., the National Institute on Drug Abuse award R01DA036909 to B.T., National  
999 Institute of Neurological Disorders and Stroke award R01NS044163 to W.J.S. and the California  
000 Institute for Regenerative Medicine (GC1R-06673-B) and the Chan Zuckerberg Initiative DAF, an  
001 advised fund of the Silicon Valley Community Foundation (2018–182730) to R.H.S. J.R.E. is an  
002 Investigator of the Howard Hughes Medical Institute. The authors thank the Allen Institute founder, Paul  
003 G. Allen, for his vision, encouragement and support.

004

## 005 Author contributions

006 RNA data generation: A.M.Y., A.R., A.T., B.B.L., B.T., C.D.K., C.R., C.R.P., C.S.L., D.B., D.D., D.M.,  
007 E.S.L., E.Z.M., F.M.K., G.F., H.T., H.Z., J.C., J.G., J.S., K.C., K.L., K.S., K.S., K.Z., M.G., M.K., M.T.,  
008 N.D., N.M.R., N.P., R.D.H., S.A.M., S.D., S.L., T.C., T.E.B., T.P., W.J.R. mC data generation: A.B.,  
009 A.I.A., A.R., C.L., H.L., J.R.E., J.R.N., R.G.C. ATAC data generation: A.E.S., B.B.L., B.R., B.T., C.R.P.,  
010 C.S.L., D.D., J.C., K.Z., L.T.G., N.P., S.P., W.J.R., X.H., X.W. Electrophysiology, morphology, and  
011 Patch-seq data generation: A.L.K., B.E.K., D.M., E.S.L., G.D.H., J.G., J.T.T., K.S., M.T., N.D., S.A.S.,  
012 S.O., T.L.D., T.P., W.J.S. Data archive and infrastructure: A.E.S., A.M., B.R.H., H.C.B., J.A.M., J.G.,  
013 J.K., J.O., M.M., O.R.W., R.H., S.A.A., S.S., Z.Y. Cytosplere Viewer software: B.P.L., B.V.L., J.E., T.H.  
014 Data analysis: A.D., B.B.L., B.D.A., B.E.K., B.P.L., B.V.L., D.D., E.A.M., E.S.L., F.M.K., F.X., H.L., J.E.,  
015 J.G., J.G., J.R.E., J.T.T., K.S., M.C., N.D., N.L.J., O.P., P.V.K., Q.H., R.F., R.H.S., R.Z., S.F., S.O.,  
016 T.E.B., T.H., W.D., W.T., Y.E.L., Z.Y. Data interpretation: A.D., A.R., B.B.L., B.E.K., B.T., C.K., C.L.,  
017 E.S.L., F.X., H.L., H.Z., J.G., J.G., J.R.E., J.T.T., M.C., M.H., N.D., N.L.J., P.R.H., P.V.K., Q.H., R.D.H.,  
018 R.H.S., R.Z., S.D., S.O., T.E.B., W.T., Y.E.L., Z.Y. Writing manuscript: A.D., B.B.L., B.E.K., C.K.,  
019 E.S.L., F.M.K., M.C., N.D., N.L.J., P.R.H., Q.H., R.H.S., T.E.B., W.J.S., W.T.

020

021 Competing interests

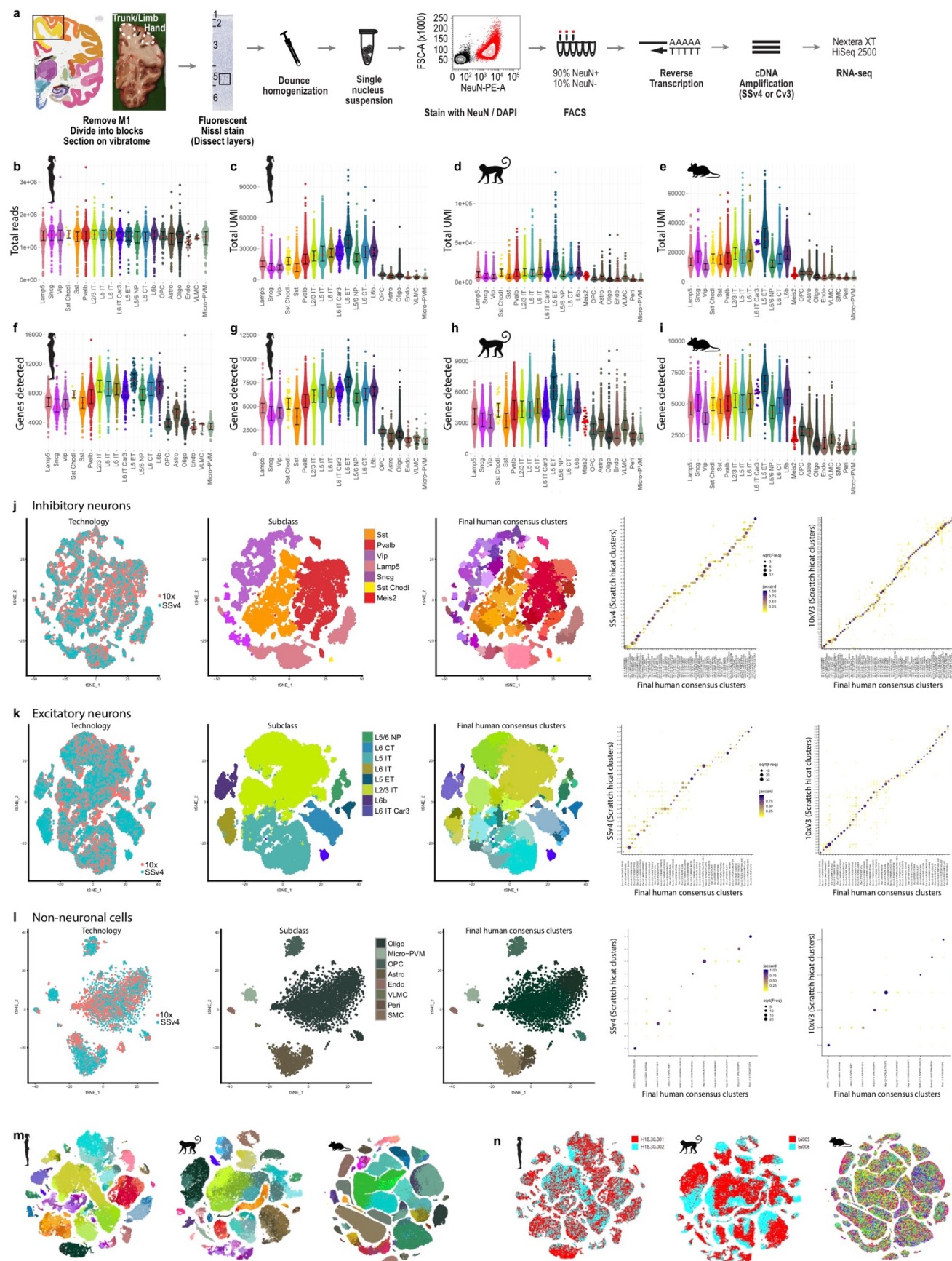
022 A.R. is an equity holder and founder of Celsius Therapeutics, a founder of Immunitas, and an SAB  
023 member in Syros Pharmaceuticals, Neogene Therapeutics, Asimov, and Thermo Fisher Scientific. B.R.  
024 is a shareholder of Arima Genomics, Inc. K.Z. is a co-founder, equity holder and serves on the  
025 Scientific Advisor Board of Singlera Genomics. P.V.K. serves on the Scientific Advisory Board to  
026 Celsius Therapeutics Inc.

027

028 Materials & Correspondence

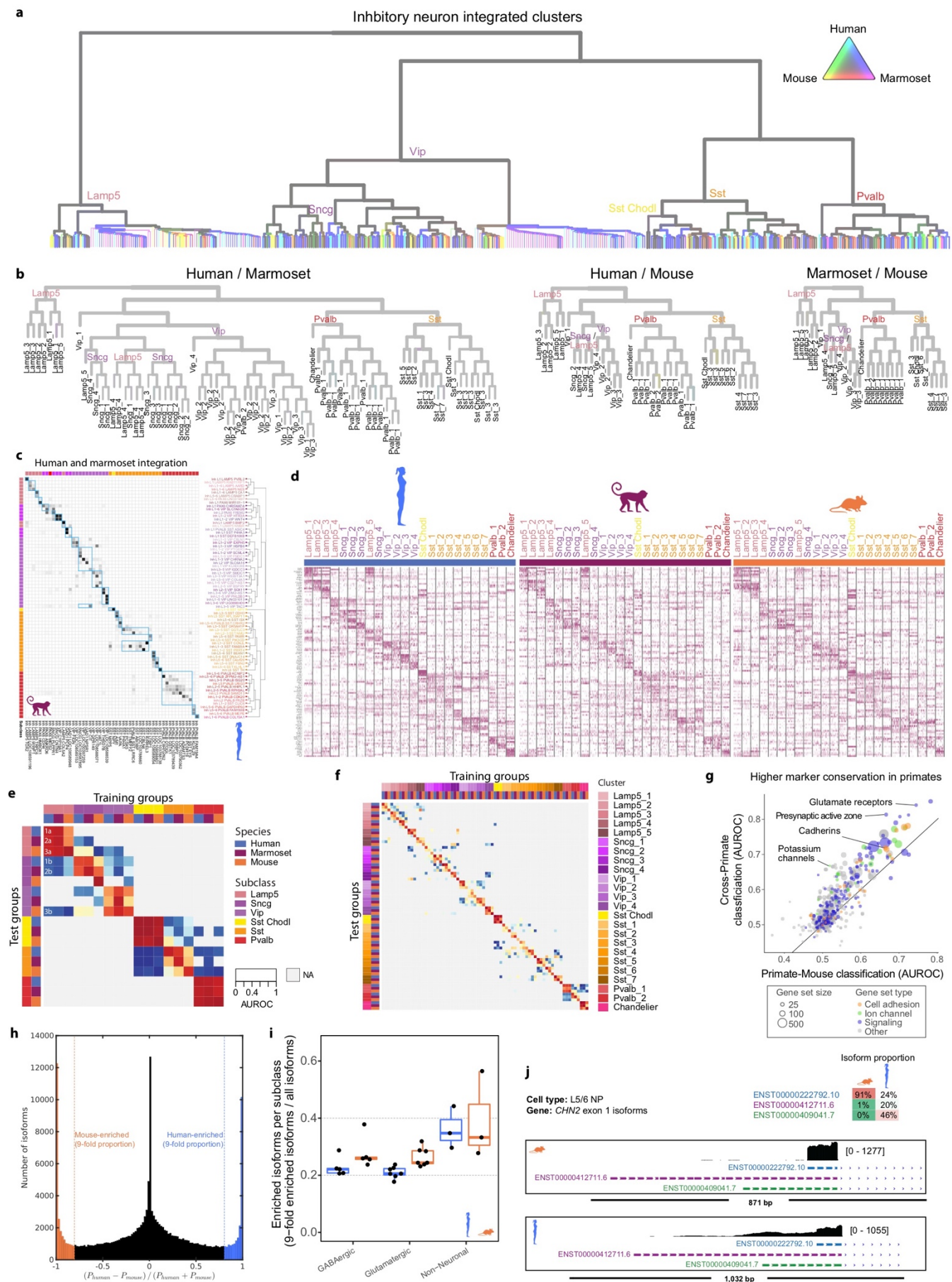
029 Correspondence and requests for materials should be addressed to E.S.L. and T.E.B.

030



032 **Extended Data Figure 1. RNA-seq quality metrics and integration of human datasets. a,**  
033 Schematic of single-nucleus isolation from M1 of post-mortem human brain and profiling with RNA-seq.  
034 Box in the Nissl image highlights a cluster of Betz cells in L5. **b,** Using SSV4, > 1 million total reads  
035 were sequenced across all subclasses in human. **c-e,** Using Cv3, total unique molecular identifiers  
036 (UMI) varies between subclasses, and these differences are shared across species. **f-i,** Gene detection  
037 (expression > 0) is highest in human using SSV4 (**e**) and lowest for marmoset using Cv3 (**h**). Note that  
038 the average read depth used for SSV4 was approximately 20-fold greater than for Cv3 (target 60,000  
039 reads per nucleus). **j-k,** tSNE projections of single nuclei based on expression of several thousand  
040 genes with variable gene expression and colored by cluster label (**j**) or donor (**k**). **l-n,** Integration of  
041 SSV4 and Cv3 RNA-seq datasets from human single nuclei isolated from GABAergic (**l**) and  
042 glutamatergic (**m**) neurons and non-neuronal cells (**n**). Left: UMAP visualizations colored by RNA-seq  
043 technology, cell subclass, and unsupervised consensus clusters. Right: Confusion matrices show  
044 membership of SSV4 and Cv3 nuclei within integrated consensus clusters.

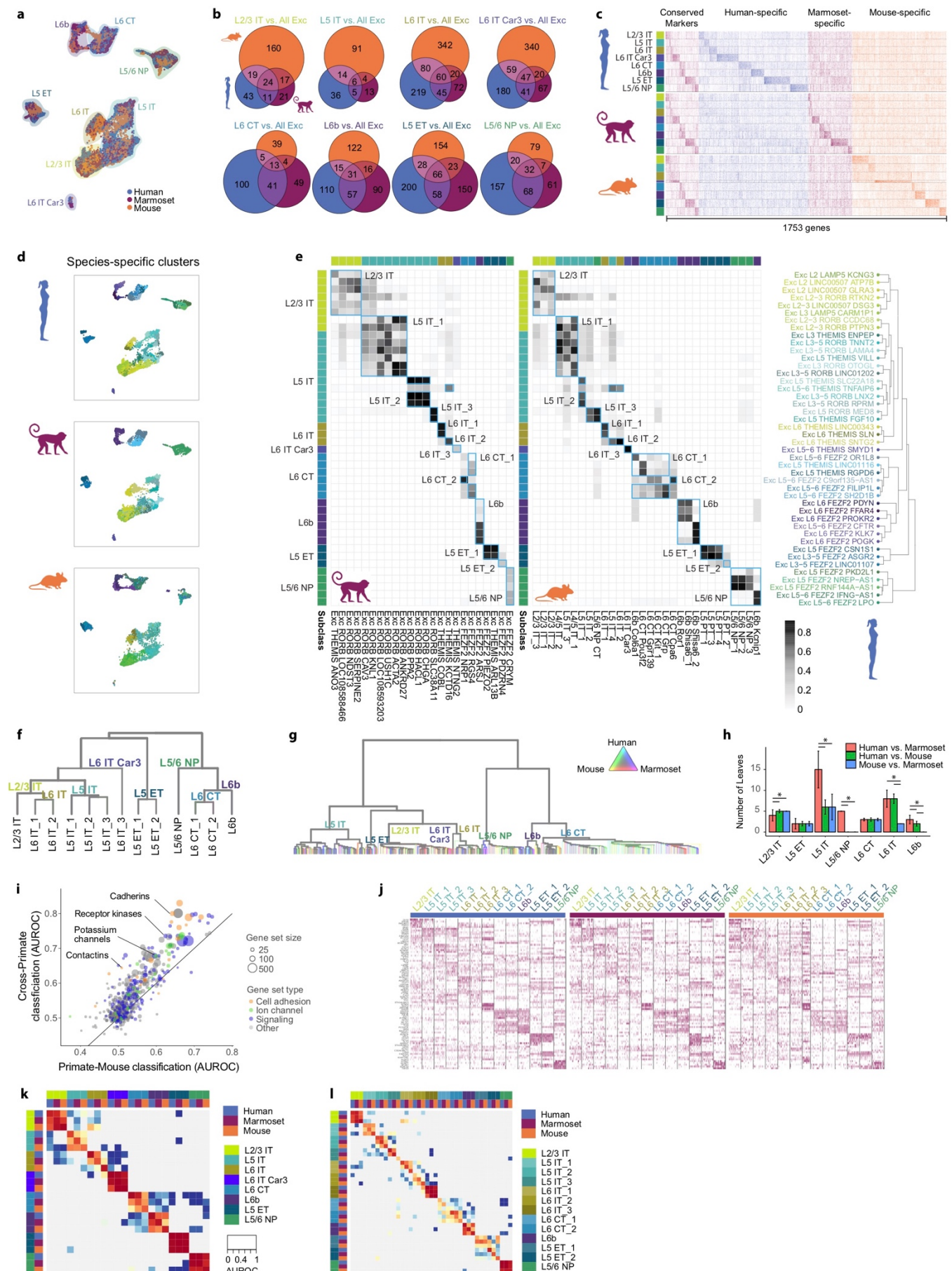
045





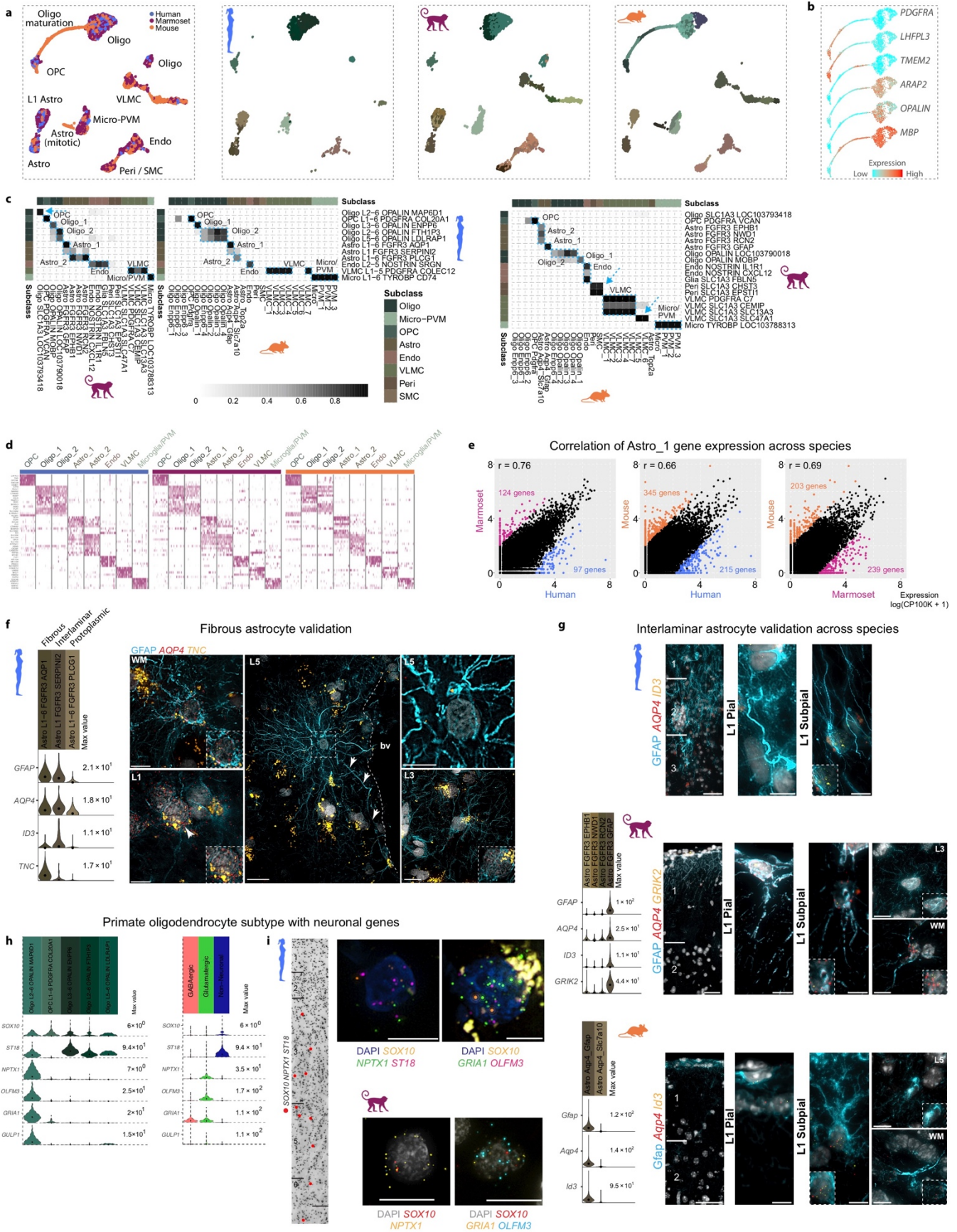
047 **Extended Data Figure 2. RNA-seq integration of GABAergic neurons across species. a,**  
048 Dendrogram of GABAergic neuron clusters from unsupervised clustering of integrated RNA-seq data  
049 from human, marmoset and mouse. Edge thickness indicates the relative number of nuclei, and edge  
050 color indicates species mixing (grey is well mixed). Major branches are labeled by subclass.  
051 Dendrogram shown in **Figure 2f** is derived from this tree based on pruning species-specific branches.  
052 **b,** Dendrograms of pairwise species integrations from **Figure 2g** with leaves labeled by cross-species  
053 clusters and edges colored by species mixing. **c,** Cluster overlap heatmap from human-marmoset  
054 pairwise Seurat integration showing the proportion of within-species clusters that coalesce within  
055 integrated clusters. Columns and rows are ordered as in **Figure 2e** with cross-species consensus  
056 clusters indicated by blue boxes. Top and left color bars indicate subclasses of within-species clusters.  
057 **d,** Heatmaps showing scaled expression of the top 5 marker genes for each GABAergic cross-species  
058 cluster, and 5 marker genes for *Lamp5* and *Sst*. Initial genes were identified by performing a Wilcox test  
059 of every integrated cluster against every other GABAergic nuclei. Additional DEGs were identified for  
060 *Lamp5* and *Sst* cross-species clusters, by comparing one of the cross-species clusters to all other  
061 related nuclei (e.g. *Sst\_1* against all other *Sst*). **e-f,** Heatmap of 1-vs-best MetaNeighbor scores for  
062 GABAergic subclasses (**e**) and clusters (**f**). Each column shows the performance for a single training  
063 group across the three test datasets. AUROCs are computed between the two closest neighbors in the  
064 test dataset, where the closer neighbor will have the higher score, and all others are shown in gray  
065 (NA). For example, in **e** the first column contains results of training on human *Lamp5*, labeled with  
066 numbers to indicate test datasets, where 1 is human, 2 is marmoset and 3 is mouse, and letters to  
067 indicate closest (**a**) and second-closest (**b**) neighboring groups. Dark red 3x3 blocks along the diagonal  
068 indicate high transcriptomic similarity across all three species. **g,** Scatter plot of MetaNeighbor analysis  
069 showing the performance (AUROC) of gene sets to classify GABAergic neuron consensus types by  
070 training with human or marmoset data and testing with the other species (Cross-Primate, y-axis) or  
071 training with primate data and testing with mouse (Primate-Mouse, x-axis). Gene set size and type are  
072 indicated by point size and color, respectively. **h,** Histogram of the relative difference in isoform genic  
073 proportion (P) between human and mouse for all subclass comparisons. All moderately to highly

074 expressed isoforms were included (gene TPM > 10 in both species; isoform TPM > 10 and proportion >  
075 0.2 in either species). Vertical lines indicate >9-fold change in mouse or human. **i**, Proportion of all  
076 isoforms in **h** that switch between species (FDR  $P < 0.05$ ; >9-fold change in  $P$ ) summarized by  
077 subclass and grouped by cell class. **j**, Comparison between species of isoform genic proportions for the  
078 top three most common isoforms of Chimerin 2 (*CHN2*) expressed in the L5/6 NP subclass. Genome  
079 browser tracks of RNA-seq (SSv4) reads in human and mouse at the *CHN2* locus.  
080



082 **Extended Data Figure 3. Glutamatergic neuron cell type homology across species. a**, UMAP  
083 visualization of integrated snRNA-seq data from human, marmoset, and mouse glutamatergic neurons.  
084 Highlighted colors indicate subclass. **b**, Venn diagrams indicating number of shared DEGs across  
085 species by subclass. DEGs determined by ROC test of subclass against all other glutamatergic  
086 subclasses within a species. **c**, Heatmap of all DEGs from **b** ordered by subclass and species  
087 enrichment. Heatmap shows expression scaled by column for up to 50 randomly sampled nuclei from  
088 each subclass for each species. **d**, UMAP visualization of integrated snRNA-seq data with projected  
089 nuclei split by species. Colors indicate different within-species clusters. **e**, Cluster overlap heatmap  
090 showing the proportion of within-species clusters that coalesce with a given integrated cross-species  
091 cluster. Cross-species clusters are labelled and indicated by blue boxes with human-marmoset overlap  
092 shown to the left and human-mouse overlap shown to the right. Top and left axes indicate the subclass  
093 of a given within-species cluster by color. Bottom axis indicates marmoset (left) and mouse (right)  
094 within species clusters. Right axis shows the glutamatergic branch of the human dendrogram from  
095 **Figure 1c**. **f**, Dendrogram of glutamatergic neuron cross-species clusters. **g**, Unpruned dendrogram of  
096 glutamatergic neuron clusters from unsupervised clustering of integrated RNA-seq data. Edge  
097 thickness indicates the relative number of nuclei, and edge color indicates species mixing. Major  
098 branches are labeled by subclass. **h**, Bar plots quantifying the number of well-mixed clusters from  
099 unsupervised clustering of pairwise species integrations. Significant differences (adjusted  $P < 0.05$ ,  
100 Tukey's HSD test) between species are indicated for each subclass. **i**, Scatter plot of MetaNeighbor  
101 analysis showing the performance (AUROC) of gene sets to classify glutamatergic neuron consensus  
102 types by training with human or marmoset data and testing with the other species (Cross-Primate, y-  
103 axis) or training with primate data and testing with mouse (Primate-Mouse, x-axis). Gene set size and  
104 type are indicated by point size and color, respectively. **j**, Heatmaps showing scaled expression of  
105 marker genes for each glutamatergic cross-species cluster. The top 5 marker genes for each cross-  
106 species cluster are shown, with an additional 5 genes for L5 ET, L5 IT, and L6 IT. Initial genes were  
107 identified by performing a Wilcox test of every integrated cluster against every other glutamatergic  
108 nuclei. Additional DEGs were identified for L5 ET, L5 IT, and L6 IT cross-species clusters, by

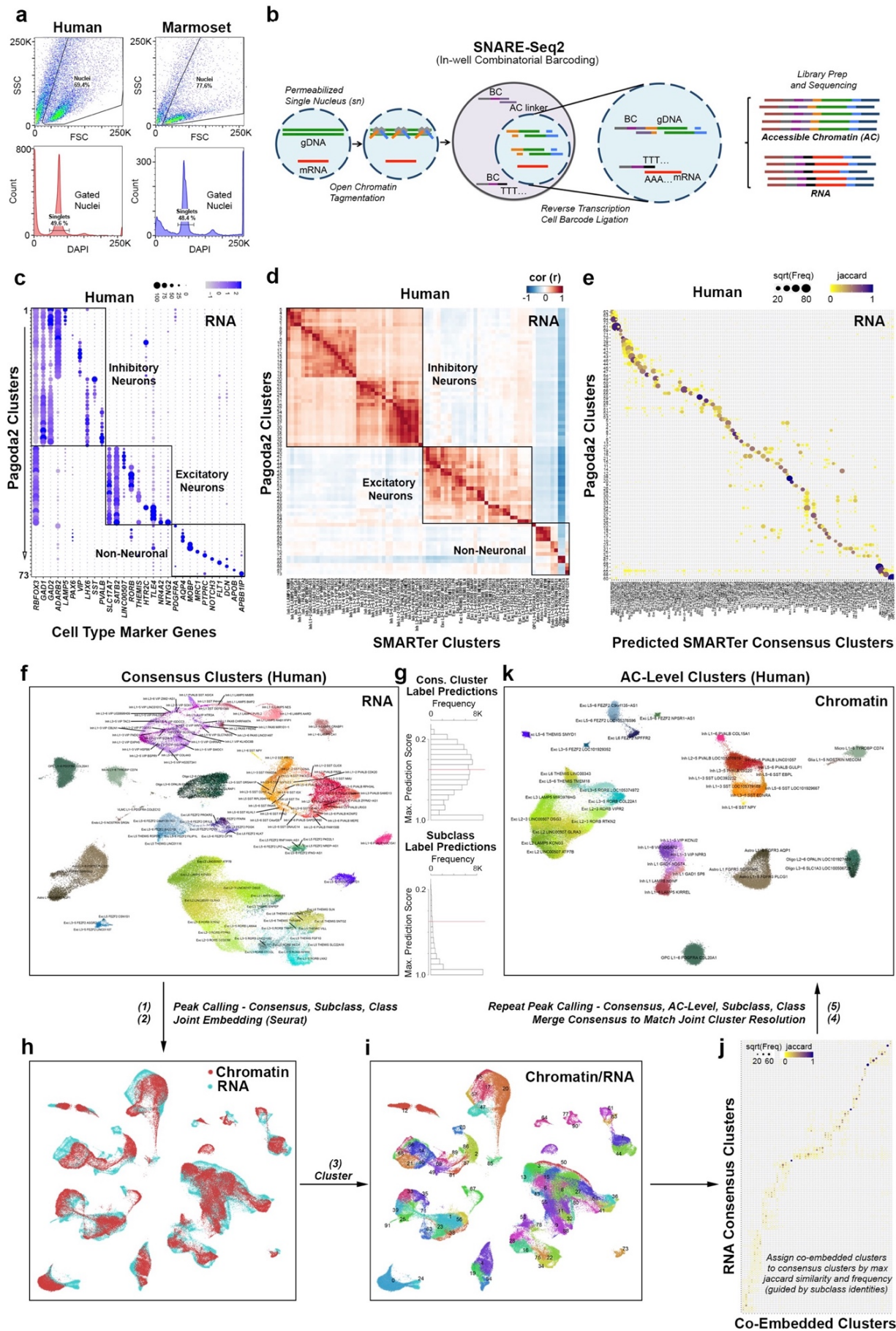
109 comparing one of the cross-species clusters to all other related nuclei (e.g. L5 IT\_1 against all other L5  
110 IT). **k, I**, Heatmap of 1-vs-best MetaNeighbor scores for glutamatergic subclasses (**k**) and clusters (**I**).  
111 Results are displayed as in **Extended Data Fig. 2e,f**.  
112



114 **Extended Data Figure 4. Non-neuronal cell type homology across species.** **a**, UMAP plots of  
115 integrated RNA-seq data for non-neuronal nuclei, colored by species and within-species clusters. Note  
116 that some cell types are present in only one or two species. **b**, UMAP of mouse oligodendrocyte  
117 precursors and mature cells showing expression levels of marker genes for different stages of cell  
118 maturation. **c**, Heatmaps of the proportion of nuclei in each species-specific cluster that overlap in the  
119 integrated RNA-seq analysis. Blue boxes define homologous cell types that can be resolved across all  
120 three species. Arrows highlight clusters that overlap between two species and are not detected in the  
121 third species, due to differences in sampling depth of non-neuronal cells, relative abundances of cell  
122 types between species, or evolutionary divergence. **d**, Conserved marker genes for homologous cell  
123 types across species. **e**, Pairwise comparisons between species of log-transformed gene expression of  
124 the Astro\_1 type. Colored points correspond to significantly differentially expressed (DE) genes (FDR <  
125 0.01, log-fold change > 2). **r**, Spearman correlation. **f**, Fibrous astrocyte in situ validation. Violin plots of  
126 marker genes of human astrocyte clusters that correspond to fibrous, interlaminar, and protoplasmic  
127 types based on in situ labeling of types. Left ISH: Fibrous astrocytes located in the white matter (WM,  
128 top) and a subset of L1 (bottom) astrocytes express the Astro L1-6 *FGFR3 AQP1* marker gene *TNC*.  
129 Middle ISH: Image of putative varicose projection astrocyte located in cortical L5 adjacent to a blood  
130 vessel (bv) and extending long GFAP-labeled processes (white arrows) does not express the marker  
131 gene *TNC*. The white dashed box indicates the area shown at higher magnification in the top right  
132 panel. Likewise, the L3 protoplasmic astrocyte shown in the bottom right panel does not express *TNC*.  
133 **g**, Combined GFAP immunohistochemistry and RNAscope FISH for markers of L1 astrocytes in  
134 human, mouse, and marmoset. In human (top), pial and subpial interlaminar astrocytes are labeled with  
135 *AQP4* and *ID3* and extend long processes from L1 down to L3. In marmoset (middle), both pial and  
136 subpial L1 astrocytes express *AQP4* and *GRIK2* and extend GFAP-labeled processes through L1 that  
137 terminate before reaching L2. An image of a marmoset protoplasmic astrocyte located in L3 shows that  
138 this astrocyte type does not express the marker gene *GRIK2*. A subset of marmoset fibrous astrocytes  
139 located in the white matter (WM) express *GRIK2*, suggesting that fibrous and L1 astrocytes have a  
140 shared gene expression signature as shown in human<sup>2</sup>. L1 astrocytes in mouse (bottom) consist of pial

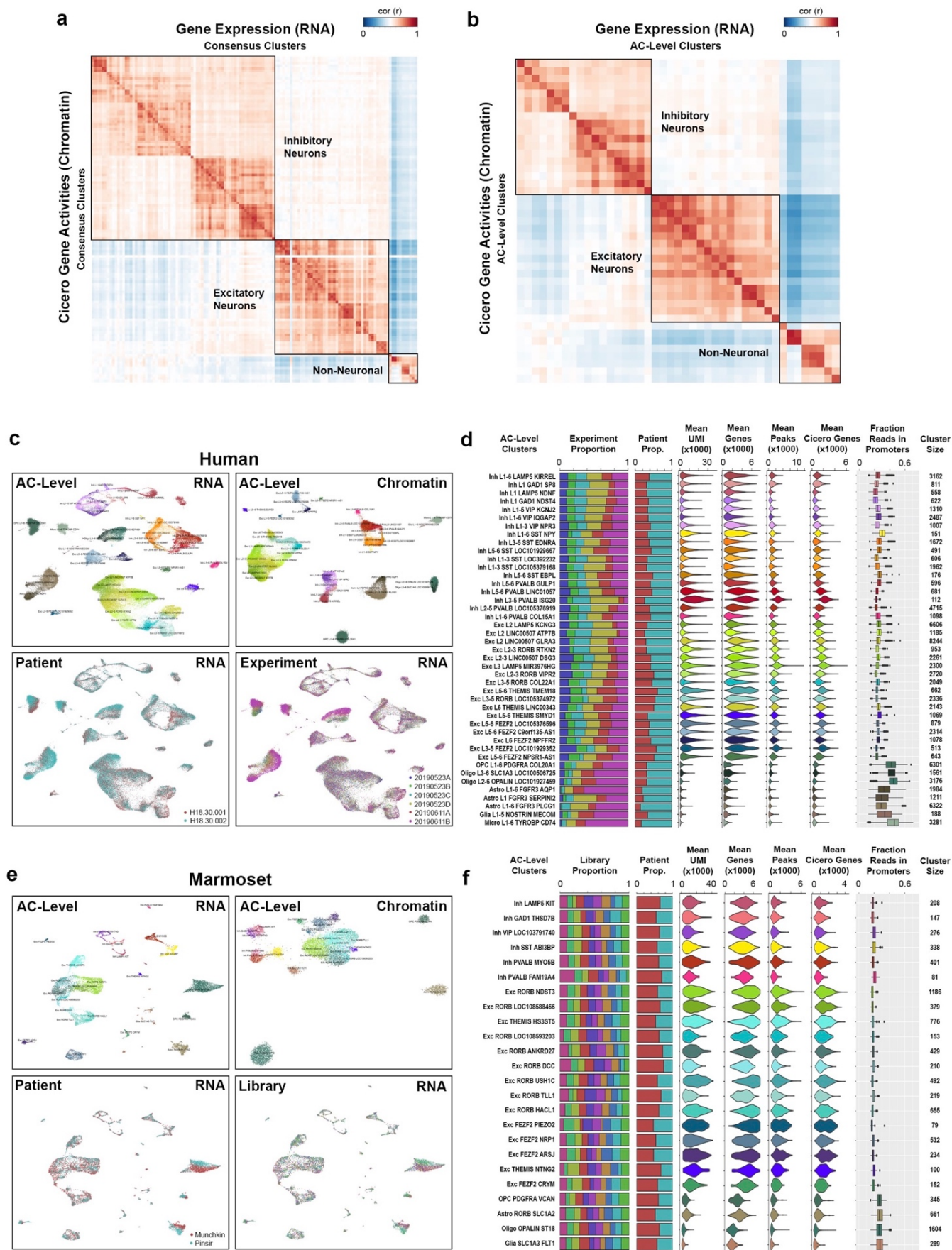
141 and subpial types that differ morphologically but are characterized by their expression of the genes  
142 *Aqp4* and *Id3*. Pial astrocytes in mouse extend short Gfap-labeled processes that terminate within L1  
143 whereas mouse subpial astrocytes appear to extend processes predominantly toward the pial surface.  
144 Protoplasmic astrocytes (example shown in L5) do not express *Id3*, whereas fibrous astrocytes in  
145 mouse share expression of *Id3* with L1 astrocyte types. Inset images outlined with white dashed boxes  
146 illustrate cells in each of the accompanying images at higher magnification to show RNAscope spots for  
147 each gene labeled. Scale bars, 20  $\mu\text{m}$ . **h**, Violin plots of marker genes of oligodendrocyte lineage  
148 clusters in human. Transcripts detected in the Oligo L2–6 *OPALIN MAP6D1* cluster include genes  
149 expressed almost exclusively in neuronal cells. Scale bars, 20  $\mu\text{m}$ . **i**, Left: Inverted DAPI image  
150 showing a column of cortex labeled with markers of the human Oligo L2-6 *OPALIN MAP6D1* type. Red  
151 dots show cells triple labeled with *SOX10*, *NPTX1*, and *ST18*. Top right: Examples of cells labeled with  
152 marker gene combinations specific for the human Oligo L2-6 *OPALIN MAP6D1* type. Bottom right:  
153 Example of a marmoset cell labeled with the marker genes *OLIG2* and *NRXN3*. Scale bars, 20  $\mu\text{m}$ .  
154





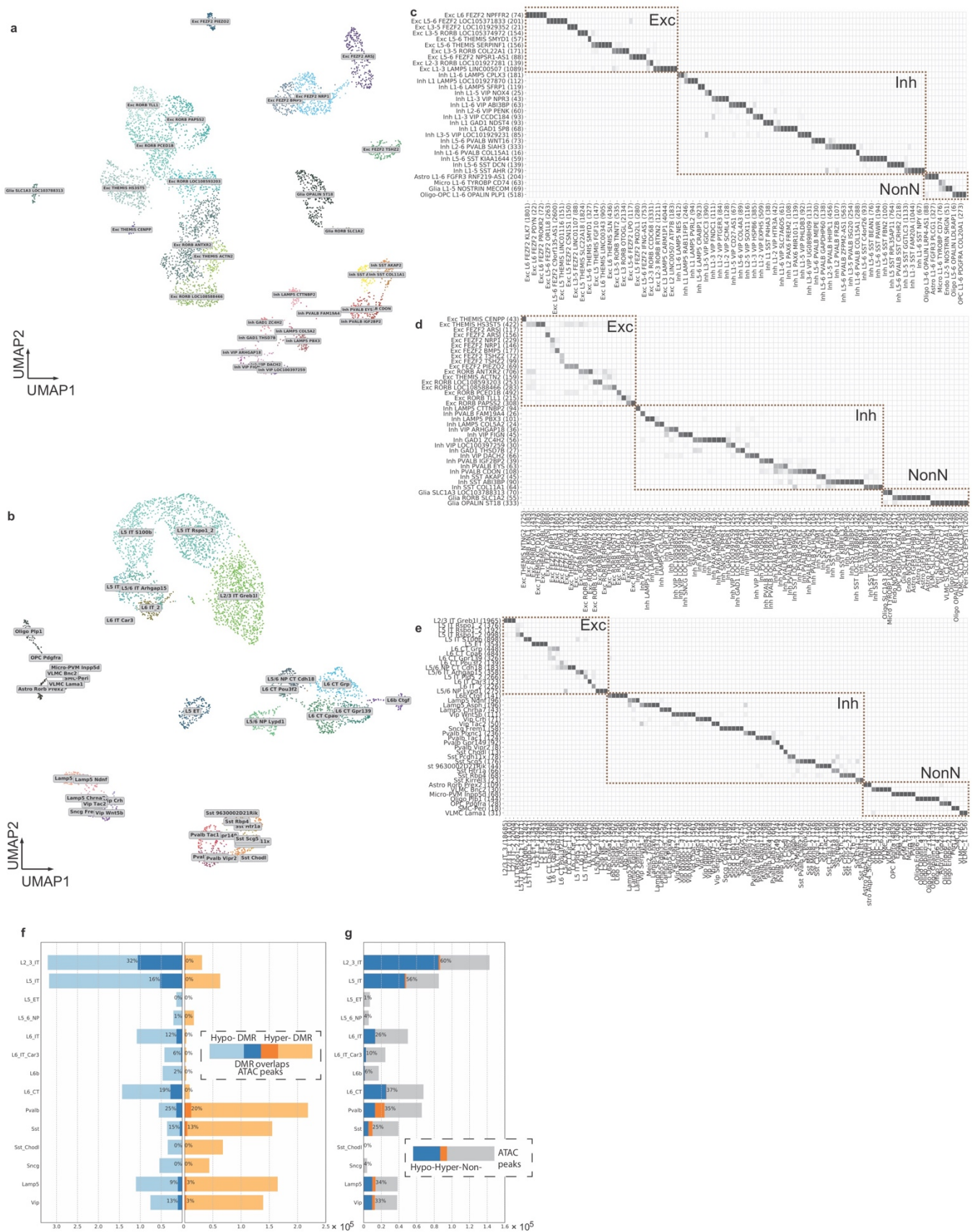
156 **Extended Data Figure 5. SNARE-seq2 transcriptomic profiling resolves M1 cell types. a-b**, FACS  
157 gating parameters used for sorting human and marmoset single nuclei (**a**) that were used for SNARE-  
158 seq2 as outlined in (**b**), to generate both RNA and accessible chromatin (AC) libraries having the same  
159 cell barcodes. **c**, Dot plot showing averaged marker gene expression values (log scale) and proportion  
160 expressed for clusters identified in a preliminary analysis of SNARE-seq2 RNA using Pagoda2. **d**,  
161 Correlation heatmap of averaged scaled gene expression values for Pagoda2 clusters against SSv4  
162 clusters from the same M1 region. **e**, Jaccard similarity plot for cell barcodes grouped according to  
163 Pagoda2 clustering compared against the predicted SSv4 consensus clustering. **f-k**, Overview of AC-  
164 level cluster assignment using RNA-defined clusters indicating the five main steps of the process. **f**,  
165 Consensus clusters visualized by UMAP on RNA expression data and that were used to independently  
166 call peaks from AC data. **g**, Histograms showing maximum prediction scores for consensus cluster  
167 (top) and subclass (bottom) labels from RNA data to corresponding accessibility data (cicero gene  
168 activities). **h**, Consensus cluster peaks, as well as those identified from subclass and class level  
169 barcode groupings, were combined and the corresponding peak by cell barcode matrix was used to  
170 predict gene activity scores using Cicero for integrative RNA/AC analyses. UMAP shows joint  
171 embedding of RNA and imputed AC expression values using Seurat/Signac. **i**, UMAP showing clusters  
172 identified from the joint embedding (**h**). **j**, Jaccard similarity plot comparing cell barcodes either grouped  
173 according to RNA consensus clustering or joint RNA/AC clustering (**i**). RNA consensus clusters were  
174 merged to best match the cluster resolution achieved from co-embedded clusters. Chromatin peak  
175 counts generated from peak calling independently on consensus, AC-level, subclass, and class  
176 barcode groupings were used to generate a final peak by cell barcode matrix. **k**, Final AC-level clusters  
177 visualized using UMAP.

178

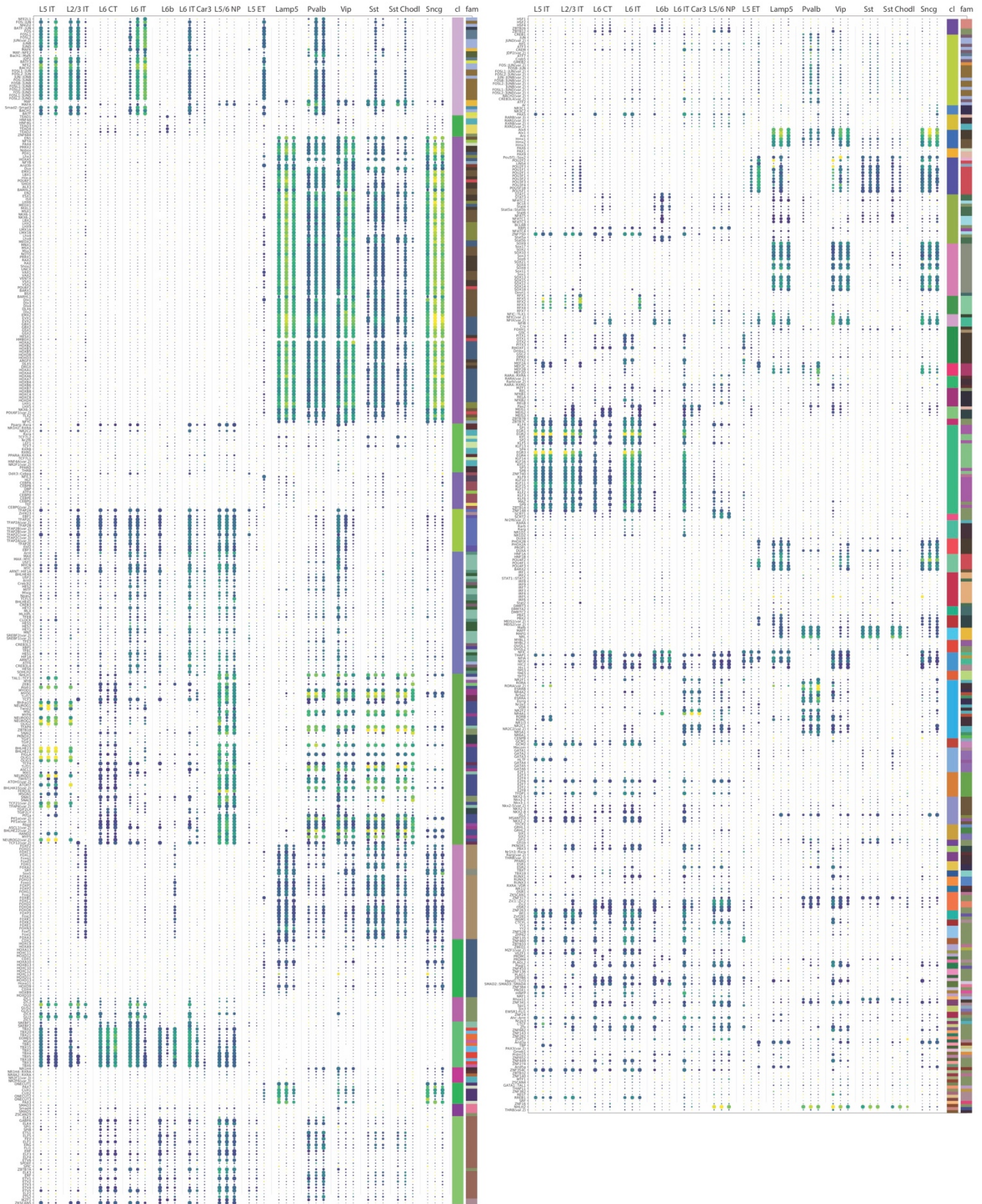


180 **Extended Data Figure 6. SNARE-Seq2 quality statistics. a-b**, Correlation heatmaps of average  
181 scaled gene expression values against average scaled Cicero gene activity values for consensus  
182 clusters (**a**) and AC-level clusters (**b**). **c**, UMAP plots showing human AC-level clusters for both RNA  
183 and chromatin data, as well as the corresponding patient and experiment identities for the RNA  
184 embeddings. **d**, Bar, violin and box plots for human AC-level clusters showing proportion contributed by  
185 each experiment or patient, mean UMI and genes detected from the RNA data, the mean peaks and  
186 cicero active genes detected from AC data, the fraction of reads found in promoters for AC data, and  
187 the number of nuclei making up each of the clusters. **e**, UMAP plots showing marmoset AC-level  
188 clusters for both RNA and chromatin data, as well as the corresponding patient and library identities for  
189 the RNA embeddings. **f**, Bar, violin and box plots for marmoset AC-level clusters showing proportion  
190 contributed by each library or patient, mean UMI and genes detected from the RNA data, the mean  
191 peaks and cicero active genes detected from AC data, the fraction of reads found in promoters for AC  
192 data, and the number of nuclei making up each of the clusters.

193

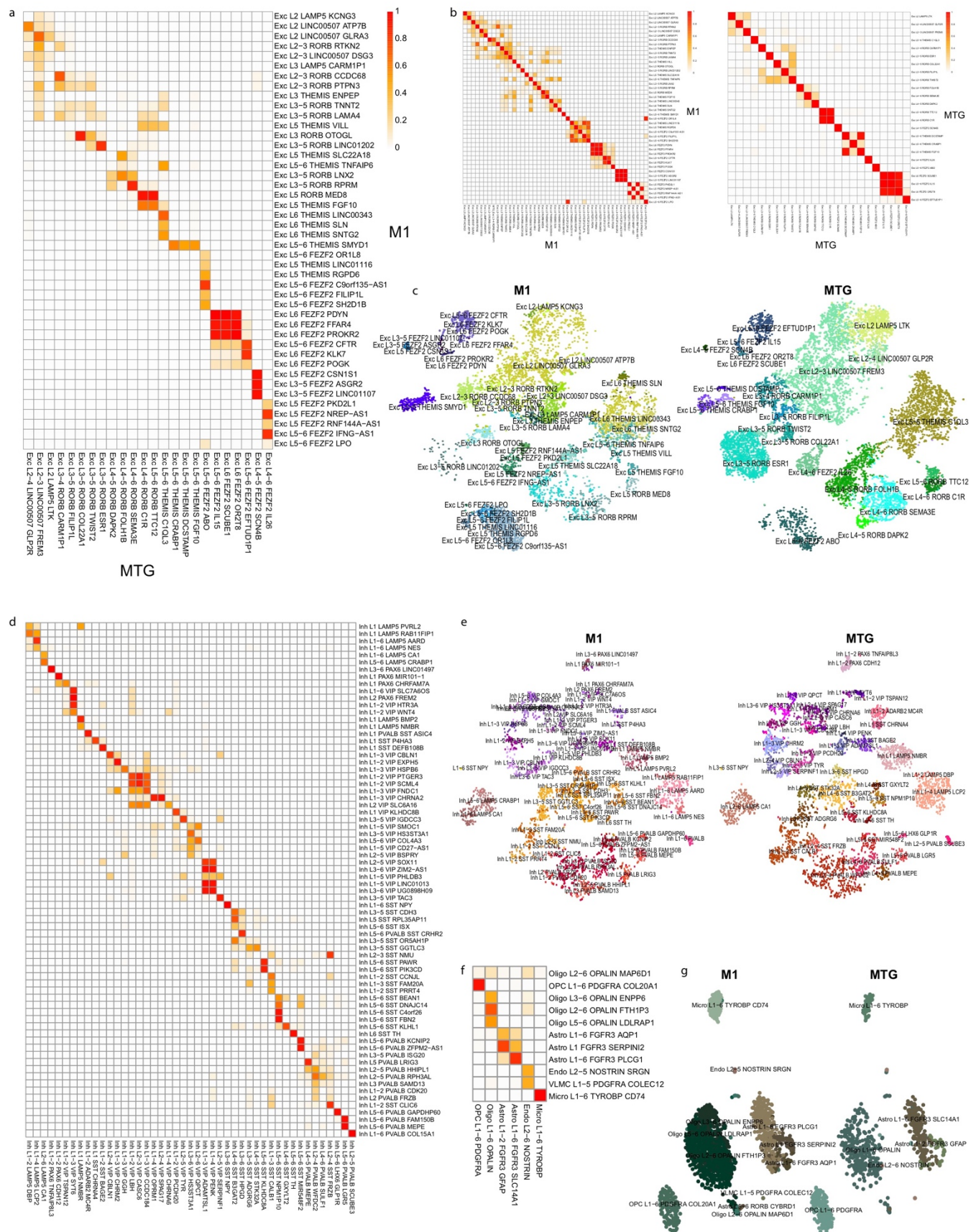


195 **Extended Data Figure 7. DNA-methylation cell type and integration with RNA-seq data. a-b,**  
196 UMAP visualization of marmoset M1 and mouse MOp DNA methylation (snmC-seq2) data and cell  
197 clusters. **c-e**, Mapping between DNAm-seq and RNA-seq clusters from human (**c**), marmoset (**d**), and  
198 mouse (**e**). Number of nuclei in each cluster are listed in parentheses. **f**, Numbers of hypo- and hyper-  
199 methylated DMRs and overlap with chromatin accessible peaks in each subclass of human. **g**,  
200 Numbers of chromatin accessible peaks and overlap with DMRs in each subclass of human.  
201  
202

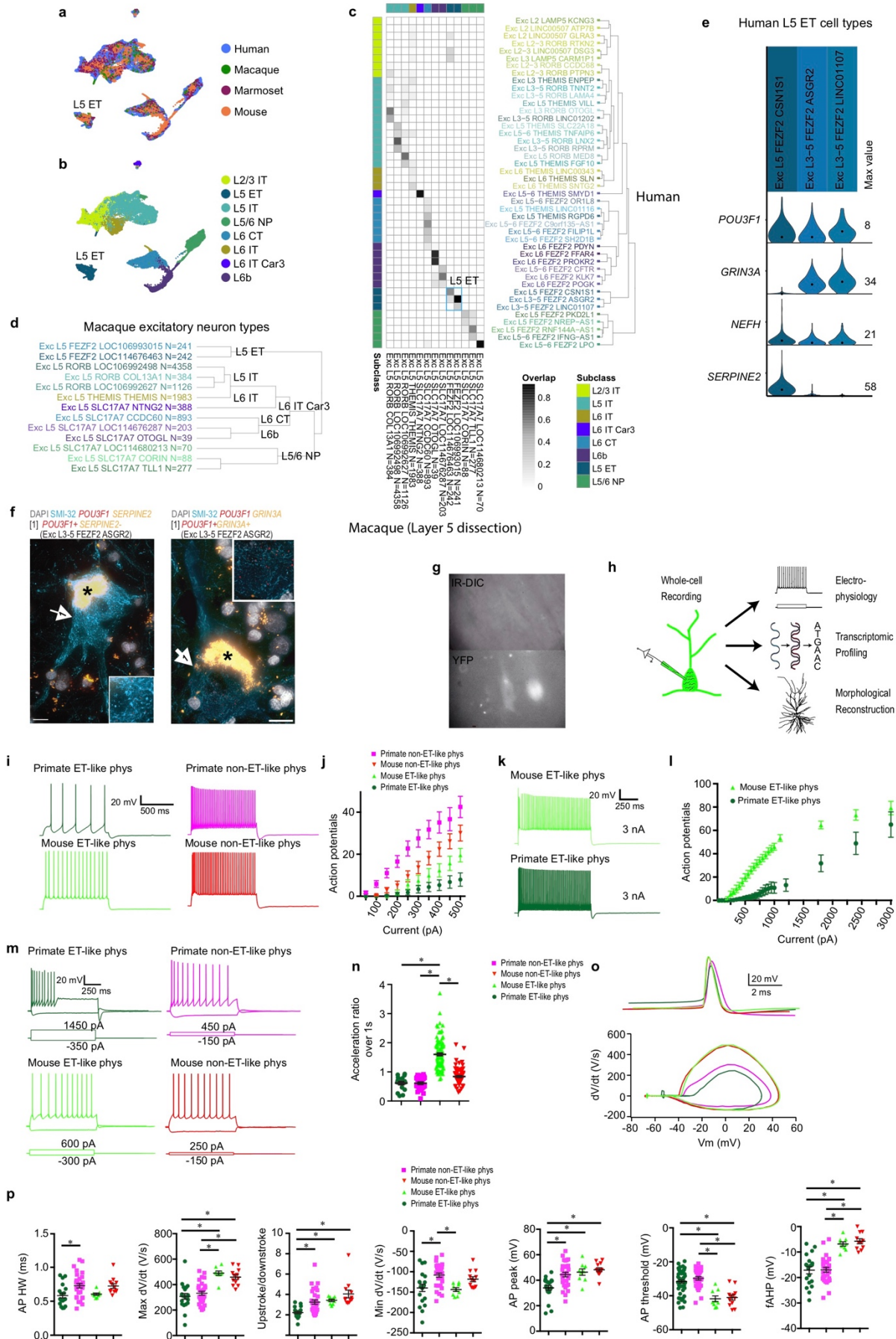


204 **Extended Data Figure 8. TFBS enrichment analysis on hypo-methylated DMRs at subclass level**  
205 **show conservativity of gene regulation across species.** Motif enrichment analysis of TFBS were  
206 conducted using JASPAR's non-redundant core vertebrata TF motifs for neuronal subclasses in each  
207 species. Each subclass tri-column shows the results of human, marmoset and mouse, respectively  
208 from left to right. The size of a dot denotes the p-value of the corresponding motif, while the color  
209 denotes the fold change. The rightmost two columns show TF clusters (cl) identified from motif profiles  
210 and TF family (fam) identified from TF structures.  
211





213 **Extended Data Figure 9. Cell type homologies between human cortical areas based on RNA-seq**  
214 **integration. a**, Heatmap of glutamatergic neuron cluster overlap between M1 and MTG. **b**, Heatmaps  
215 of glutamatergic neuron cluster overlap for M1 and MTG test datasets. Clusters were split in half and  
216 two datasets were integrated using the same analysis pipeline as the M1 and MTG integration. Most  
217 clusters mapped correctly (along the diagonal) with some loss in resolution between closely related  
218 clusters (red blocks). **c**, tSNE plots of integrated glutamatergic neurons labeled with M1 and MTG  
219 clusters. **d-g**, Cluster overlap heatmaps and tSNE plots of integrations of GABAergic neurons (**d**, **e**)  
220 and non-neuronal cells (**f**, **g**), as described for glutamatergic neurons.  
221



223 **Extended Data Figure 10. Cross-species alignment of glutamatergic neurons and differences in**  
224 **L5 neuron spike trains and single spike properties. a, b**, UMAP visualizations of cross-species  
225 integration of snRNA-seq data for glutamatergic neurons isolated from human, macaque (L5 dissection  
226 only), marmoset, and mouse. Colors indicate species (**a**) or cell subclass (**b**). **c**, Cluster overlap  
227 heatmap showing the proportion of nuclei from within-species clusters that are mixed within the same  
228 integrated clusters. Human clusters (rows) are ordered by the dendrogram reproduced from **Figure 1c**.  
229 Macaque clusters (columns) are ordered to align with human clusters. Color bars at top and left indicate  
230 subclasses of within-species clusters. Blue box denotes the L5 ET subclass. **d**, Dendrogram showing  
231 all macaque clusters from L5 dissection with subclasses denoted to the right. **e**, Violin plot showing  
232 expression of marker genes for human L5 ET neuron subtypes. **f**, Two examples of ISH labeled, SMI-  
233 32 IF stained Betz cells in L5 of human M1 that correspond to the L5 ET cluster Exc L3-5 *FEZF2*  
234 *ASGR2*. Insets show higher magnification of ISH-labeled transcripts in corresponding cells. Scale bars,  
235 20  $\mu\text{m}$ . Asterisks mark lipofuscin. **g**, Example IR-DIC (top) and fluorescent (bottom) images obtained  
236 from a macaque organotypic slice culture. Note the inability to visualize the fluorescently labeled  
237 neurons in IR-DIC because of dense myelination. **h**, patch-seq involves the collection of morphological,  
238 physiological and transcriptomic data from the same neuron. Following electrophysiological recording  
239 and cell filling with biocytin via whole cell patch clamp, the contents of the cell are aspirated and  
240 processed for RNA-sequencing. This permits a transcriptomic cell type to be pinned on the  
241 physiologically-probed neuron. **i**, Example voltage responses to a 1 s, 500 pA step current injection. **j**.  
242 Action potentials as a function of current injection amplitude. Primate ET neurons display shallowest  
243 action potential-current injection relationship, perhaps partially because of their exceptionally low input  
244 resistance. **k**, Voltage responses to a 1 s, 3 nA step current injection. **l**, Action potentials as a function  
245 of current injection for a subset of experiments in which current injection amplitude was increased  
246 incrementally to 3 nA. While both mouse and primate ET neurons could sustain high firing rates,  
247 primate neurons required 3 nA of current over 1s to reach similar average firing rates as mouse ET  
248 neurons. **m**, Example voltage responses to 1 s depolarizing step current injections. The amplitude of  
249 the current injection was adjusted to produce  $\sim 10$  spikes. Also shown are voltage responses to a

250 hyperpolarizing current injection. **n**, The firing rate of primate ET and IT neurons decreased during the 1  
 251 s step current injection, whereas, the firing rate of mouse ET neurons increased. Acceleration  
 252 ratio= $2^{\text{nd}}$ /last interspike interval. **o**, Example single action potentials (above) and phase plane plots  
 253 (below). **p**, Various action potential features are plotted as a function of cell type. Notably, action  
 254 potentials in primate ET neurons were reminiscent of fast spiking interneurons in that they were shorter  
 255 and more symmetrical compared with action potentials in other neuron types/species. Intriguingly, K<sup>+</sup>  
 256 channel subunits K<sub>v</sub>3.1 and K<sub>v</sub>3.2 that are implicated in fast spiking physiology<sup>89</sup> are encoded by highly  
 257 expressed genes (*KCNC1* and *KCNC2*) in primate ET neurons (Fig. 7c) \*  $p < 0.05$ , Bonferroni  
 258 corrected t-test.  
 259

Specimen ID	Age	Sex	Race	Cause of Death	PMI (hr)	Tissue RIN	Hemisphere Sampled	Data Type
H200.1023	43	F	Iranian descent	Mitral valve prolapse	18.5	7.4 ± 0.7	L	SSv4
H200.1025	50	M	Caucasian	Cardiovascular	24.5	7.6 ± 1.0	L	SSv4
H200.1030	54	M	Caucasian	Cardiovascular	25	7.7 ± 0.8	L	SSv4
H18.30.001	60	F	Unknown	Car accident	18	7.9 ± 2.5	R	SSv4, Cv3, SNARE-seq2, sn-methylome
H18.30.002	50	M	Unknown	Cardiovascular	10	8.2 ± 0.4	R	SSv4, Cv3, SNARE-seq2, snmC-seq2

260 **Extended Data Table 1.** Summary of human tissue donors. RIN, RNA integrity number. Data type:  
 261 SMART-Seqv4 (SSv4), 10x Genomics Single Cell 3' Kit v3 (Cv3), Single-Nucleus Chromatin  
 262 Accessibility and mRNA Expression sequencing (SNARE-seq2), Single-nucleus methylcytosine  
 263 sequencing (snmC-seq2).

264

Specimen ID	Age (years)	Sex	Data Type
bi005	2.3	M	Cv3
bi006	3.1	F	Cv3
bi003	1.9	M	FISH

265 **Extended Data Table 2.** Summary of marmoset specimens. Data type: 10x Genomics Chromium  
 266 Single Cell 3' Kit v3 (Cv3). ACD Bio multiplex fluorescent in situ hybridization (FISH).

267

## 268 Supplementary Table legends

269 **Supplementary Table 1.** Provisional cell ontology (pCL) terms for human, mouse, and marmoset  
270 primary motor cortex cell types. Column headers are described as follows: pCL\_id is a unique  
271 alphanumeric identifier assigned to each provisional cell type. CL\_id is the Cell Ontology (CL) identifier  
272 for those parent cell type classes already represented in CL. pCL\_name and Transcriptome data  
273 cluster are labels given according to each species naming convention that combines information about  
274 cortical layer enrichment and genes expressed in data cluster transcriptomes. TDC\_id is a unique  
275 identifier assigned to the transcriptome data cluster. The part\_of (uberon\_id) and part\_of  
276 (uberon\_name) columns contain unique identifiers and names for tissue anatomic regions from which  
277 the experiment specimen was derived, in this case primary motor cortex. The is\_a (CL or pCL\_id) and  
278 is\_a (CL or pCL\_name) columns contain parent cell type or provisional cell type identifiers and names,  
279 respectively. Cluster\_size indicates the number of single-nucleus or cell transcriptomes that were  
280 assigned membership to the transcriptome data cluster. Marker\_gene\_evidence indicates the number  
281 of marker genes that are necessary and sufficient to define the transcriptome cell type data cluster with  
282 maximal classification accuracy based on the NS-Forest v2.1 algorithm (see Supplementary Tables 4-  
283 6). F-measure\_evidence is the f-beta score of classification accuracy from the NS-Forest v2.1 algorithm  
284 using the marker genes listed. The selectively\_expresses column lists the minimum set of marker  
285 genes necessary and sufficient to define the transcriptome cell type data cluster. The definition brings  
286 together features to form a data driven ontological representation for each cell type cluster. The pCL  
287 annotations are available at [https://github.com/mkeshk2018/Provisional\\_Cell\\_Ontology](https://github.com/mkeshk2018/Provisional_Cell_Ontology) and  
288 <https://bioportal.bioontology.org/ontologies/PCL>.

289

290 **Supplementary Table 2.** Cluster annotations for human, marmoset, and mouse in separate  
291 worksheets. Cluster\_label column identifies the RNA-seq cluster within each species. Cluster\_size  
292 column denotes the number of nuclei that reside within each cluster (cluster\_label). Class column  
293 identifies which cell class each cluster belongs to. Subclass column identifies which cell subclass each  
294 cluster belongs to. Cross-species cluster column indicates the cross-species consensus cluster

295 taxonomy. DNAm\_cluster\_label column identifies the transcriptomic cluster (cluster\_label) that is  
296 aligned to DNAm-determined clusters. ATAC\_cluster label column identifies the transcriptomic cluster  
297 (cluster\_label) that is aligned to ATAC-determined clusters.

298

299 **Supplementary Table 3.** Application of Allen Institute nomenclature schema to mouse, marmoset, and  
300 human M1 taxonomies. The “taxonomy\_ids” tab lists ids and descriptions for the 11 taxonomies  
301 included and which tab those taxonomies are shown on. The “preferred\_aliases” tab shows a list of  
302 preferred aliases for linking between taxonomies, as well as descriptions for these. The next five tabs  
303 show nomenclatures for each of the taxonomies and have the following column headers: “tree\_order” is  
304 the order shown in the tree (if any); “cell\_set\_alias”, “cell\_set\_label”, and “cell\_set\_accession” are  
305 unique identifiers, as described in the Allen Institute nomenclature page ([https://portal.brain-](https://portal.brain-map.org/explore/classes/nomenclature)  
306 [map.org/explore/classes/nomenclature](https://portal.brain-map.org/explore/classes/nomenclature)), with “cell\_set\_alias” including the names used in this  
307 manuscript; “cell\_set\_preferred\_alias” indicates which clusters correspond to the “preferred\_alias”es  
308 from the previous tab, if any; “cell\_set\_alias\_integrated” shows linkages between single species  
309 transcriptomics taxonomies and the integrated taxonomy; “cell\_set\_labels\_CS191213#” columns  
310 indicate linkages between cell sets in the transcriptomics and other modalities within a single species;  
311 “cell\_set\_descriptor” shows the type of cell set (or level of ontology); and “taxonomy\_id” links to the  
312 “taxonomy\_id” tab. Finally, the “Cell class hierarchy” tab shows the ordered class, level2, and subclass  
313 hierarchy and associated colors used as cell sets in previous tabs.

314

315 **Supplementary Table 4.** NS-Forest v2.1 was used to determine cell type cluster marker genes for all  
316 annotated levels of the human primary motor cortex cell type taxonomy defined by RNA-seq (Cv3).  
317 “clusterName” corresponds to the annotation label, either a cell type cluster name or a parent cell type  
318 class in the taxonomy. “markerCount” gives the optimal number of marker genes in the set that best  
319 discriminates the label. The “f-measure” column gives the f-beta score for classification using the set of  
320 markers. The next four columns “True Negative”, “False Positive”, “False Negative”, “True Positive” give

321 the confusion matrix for the label given the set of markers. Finally, “Marker 1-5” lists the gene symbols  
322 corresponding to the optimal set of markers.

323

324 **Supplementary Table 5.** NS-Forest v2.1 was used to determine cell type cluster marker genes for all  
325 annotated levels of the mouse primary motor cortex cell type taxonomy defined by RNA-seq (Cv3).  
326 “clusterName” corresponds to the annotation label, either a cell type cluster name or a parent cell type  
327 class in the taxonomy. “markerCount” gives the optimal number of marker genes in the set that best  
328 discriminates the label. The “f-measure” column gives the f-beta score for classification using the set of  
329 markers. The next four columns “True Negative”, “False Positive”, “False Negative”, “True Positive” give  
330 the confusion matrix for the label given the set of markers. Finally, “Marker 1-5” lists the gene symbols  
331 corresponding to the optimal set of markers.

332

333 **Supplementary Table 6.** NS-Forest v2.1 was used to determine cell type cluster marker genes for all  
334 annotated levels of the marmoset primary motor cortex cell type taxonomy defined by RNA-seq (Cv3).  
335 “clusterName” corresponds to the annotation label, either a cell type cluster name or a parent cell type  
336 class in the taxonomy. “markerCount” gives the optimal number of marker genes in the set that best  
337 discriminates the label. The “f-measure” column gives the f-beta score for classification using the set of  
338 markers. The next four columns “True Negative”, “False Positive”, “False Negative”, “True Positive” give  
339 the confusion matrix for the label given the set of markers. Finally, “Marker 1-5” lists the gene symbols  
340 corresponding to the optimal set of markers.

341

342 **Supplementary Table 7.** DEGs determined by ROC test between each GABAergic neuron subclass  
343 and all other GABAergic nuclei within each species. Columns are labeled myAUC, which contains AUC  
344 scores > 0.7; avg\_diff, which contains difference in expression between target subclass and all other  
345 GABAergic neurons; power; pct.1, which indicates the percent of nuclei that express the gene in the  
346 target cluster; pct.2, which indicates the percent of non-target nuclei that express the gene; cluster,



347 which denotes the target cluster; gene, indicating the gene that was identified as DE; and species,  
348 which indicates the species the test was performed in.

349

350 **Supplementary Table 8.** List of DEGs (from Supplementary Table 7) that is sorted according to the  
351 order the genes appear within the heatmap.

352

353 **Supplementary Table 9.** Supervised MetaNeighbor results, within- and across-species. Each row  
354 corresponds to a unique entry for a given gene set and a given cell class, either Glutamatergic or  
355 GABAergic. The first five columns provide information about the gene sets, namely their provenance  
356 (SynGO or HGNC); numerical IDs; descriptive labels; manual classifications for plotting and  
357 interpretation; and finally the number of genes included in the analysis (after subsetting to genes with 1-  
358 1 orthologs across all three species). The sixth column indicates cell class. The remaining columns  
359 contain MetaNeighbor AUROCs for various analyses: within\_species\_meanROC (column 7) provides  
360 the mean of within-mouse (column 8), within-marmoset (column 9) and within-human (column 10)  
361 performance. For each species, tests were run with random 3-fold cross-validation, and the average  
362 across folds is reported. Columns 11 and 12 contain results from cross-species analyses, detailed in  
363 the methods. Results are sorted by their AUROC across primates (column 12).

364

365 **Supplementary Table 10.** DEGs determined by ROC test between each glutamatergic neuron  
366 subclass and all other glutamatergic nuclei within each species. Columns are labeled myAUC, which  
367 contains AUC scores > 0.7; avg\_diff, which contains difference in expression between target subclass  
368 and all other glutamatergic neurons; power; pct.1, which indicates the percent of nuclei that express the  
369 gene in the target cluster; pct.2, which indicates the percent of non-target nuclei that express the gene;  
370 cluster, which denotes the target cluster; gene, indicating the gene that was identified as DE; and  
371 species, which indicates the species the test was performed in.

372

373 **Supplementary Table 11.** List of DEGs (from Supplementary Table 10) that is sorted according to the  
374 order the genes appear within the heatmap.

375

376 **Supplementary Table 12.** Average expression of isoforms in human and mouse subclasses and  
377 estimates of isoform genic proportions (P) based on the ratio of isoform to gene expression. Isoforms  
378 were included if they had at least moderate expression (TPM > 10) and P > 0.2 in either human or  
379 mouse and at least moderate gene expression (TPM > 10) in both species.

380

381 **Supplementary Table 13.** SNARE-Seq2 metadata, cluster annotations and quality statistics. Tab 14a  
382 indicates SNARE-Seq2 experiment level metadata (experiment name, library, patient, species,  
383 purification, age, sex) and mapping statistics for RNA (mean UMI detected, mean genes detected) and  
384 AC (mean fraction of reads in promoters or FRiP, mean uniquely mapped fragments grouped by 5000  
385 base pair chromosomal bins, mean unique fragment counts per final peak locations, total number of  
386 final nuclei). Tab 14b indicates the SNARE-Seq2 local RNA clusters for human M1 generated using  
387 Pagoda2 (local cluster, annotated cluster name, broad cell type and abbreviation, k value used for  
388 Pagoda2 clustering, broad cell type markers, level 1 and level2 classes and associated markers,  
389 unique cluster markers). Tabs 14c-d indicates SNARE-Seq2 consensus or harmonized RNA and AC-  
390 Level cluster annotations for human and marmoset M1, respectively, including annotated cluster name,  
391 cluster order, associated subclass and class, and the number of datasets making up the clusters. Tabs  
392 14e-f lists all metadata outlined in tabs 14a-d for all SNARE-Seq2 cell barcodes from human and  
393 marmoset M1 samples, respectively.

394

395 **Supplementary Table 14.** SNARE-Seq2 differentially accessible regions for human and marmoset M1.  
396 Tabs 15a and 15b show SNARE-Seq2 differentially accessible regions (DARs, q value < 0.001, log-fold  
397 change > 1) identified by AC-Level clusters (15a) or subclass level (15b) for human M1, indicating for  
398 each chromosomal location the p value (hypergeometric test), q value (Benjamini-Hochberg adjusted p  
399 value), log-fold change and associated cluster or subclass. Tab 15b shows subclass DARs (q value <

400 0.001, log-fold change > 1) for marmoset subclasses as in tab 15b. Tab 15d shows a summarization of  
401 human and marmoset DARs detected by matched subclasses, indicating actual number of DARs  
402 detected (tabs 15b and 15c) and the values normalized to cluster size and total number of DARs  
403 detected per species.

404

405 **Supplementary Table 15.** Cis-co-accessible sites, TF motif enrichments and differential TFBS  
406 activities for human and marmoset M1. Tab 16a (human M1) and 16b (marmoset M1) show cis-  
407 coaccessible network (CCAN) sites for subclass distinct markers genes (Wilcoxon Rank Sum test,  
408 adjusted  $P < 0.05$ , average log-fold change > 0.5). pct.1 indicates the percent of nuclei that express the  
409 gene in the target cluster, pct.2 indicates the percent of non-target nuclei that express the gene. For  
410 each cluster and marker gene, corresponding motif enrichment values (hypergeometric test) for gene-  
411 associated CCAN sites are shown (“observed” indicates number of features containing the motif,  
412 “background” indicates the total number of features from a random selection of 40000 features that  
413 contain the motif), and the motif associated differential chromVAR activity values identified using  
414 logistic regression. The full list of chromVAR differentially active TFBS activities are also provided. Tab  
415 16c summarizes the number of CCAN-associated marker genes, associated TFBSs enriched and or  
416 active by subclass for both human and marmoset M1. Tabs 16d and 16e show cis-co-accessible sites,  
417 TFBS enrichments and differential activities by AC-level clusters for human and marmoset M1,  
418 respectively, similar to that provided in tabs 16a and 16b. Tab 16f shows chromVAR differentially active  
419 TFBS activities by consensus or harmonized cluster using logistic regression. Tabs 16g, 16h, and 16i  
420 show cis-co-accessible sites, TF motif enrichments and differential TFBS activities for human,  
421 marmoset and mouse M1 ChCs compared against BCs.

422

423 **Supplementary Table 16.** snmC-seq2 metadata. The table shows experiment level metadata,  
424 including species, sample name, gender, purification information, experiment nuclei numbers and pass-  
425 QC nuclei numbers.

426

427 **Supplementary Table 17.** Subclass TFBS enrichment results. TFBS enrichment analysis was done  
428 with AME<sup>77</sup> using JASPAR2020 motifs. Within a species, hypo-methylated DMRs in each subclass  
429 were tested against hypo-methylated DMRs of all the other subclasses (background). DMRs and 250bp  
430 around regions were used in the analysis. This table includes p-values and effect sizes ( $\log_2(\text{TP}/\text{FP})$ ) of  
431 the analysis results.

432

433 **Supplementary Table 18.** Subclass TFBS enrichment at TF cluster level. TFs in SI Tab 18 were  
434 grouped using clusters defined in Ref<sup>42</sup>. The table lists the most significant p-values and the largest  
435 effect size of each TF cluster group.

436

437 **Supplementary Table 19.** DEGs determined by ROC test between chandelier cells and basket cells  
438 within each species. Columns are labeled as species, with true/false values indicating if a gene was  
439 enriched in chandelier cells for that species.

440

441 **Supplementary Table 20.** DEGs determined by ROC test between L5 ET subclass and L5 IT subclass  
442 within each species. Columns are labeled as species, with values of 1 indicating a gene was enriched  
443 in the L5 ET subclass for that species. A value of 0 indicates that the gene was not enriched in the L5  
444 ET subclass for that species.

445

446 **Supplementary Table 21.** Genes with expression enrichment in L5 ET versus L5 IT that decreases  
447 with evolutionary distance from human (human > macaque > marmoset > mouse). Columns are labeled  
448 by species, and values indicate the log-fold change between L5 ET and L5 IT for that species. Genes  
449 were included if they had a minimum log-fold change equal to 0.5 in human.